HOKKAIDO UNIVERSITY

Title	Studies on Self-Assembled Platinum(II) and Palladium(II) Complexes : Control of Crystal Structures and Luminescence Properties
Author(s)	齋藤, 大将
Degree Grantor	北海道大学
Degree Name	博士(理学)
Dissertation Number	甲第15398号
Issue Date	2023-03-23
DOI	https://doi.org/10.14943/doctoral.k15398
Doc URL	https://hdl.handle.net/2115/91493
Type	doctoral thesis
File Information	SAITO_Daisuke.pdf

Studies on Self-Assembled Platinum(II) and Palladium(II) Complexes: Control of Crystal Structures and Luminescence Properties

(自己集積型白金(II)及びパラジウム(II)錯体に関する研究：

結晶構造および発光特性の制御)

Daisuke Saito

Graduate School of Chemical Sciences and Engineering

Hokkaido University

2023

Contents

Studies on Self-Assembled Platinum(II) and Palladium(II) Complexes: Control of Crystal Structures and Luminescence Properties

Chapter 1
General Introduction

1.1 Luminescent materials

Luminescent compounds have been actively developed to be applied to OLEDs (organic light-emitting devices) [1–5] and sensor materials [6]. In general, when considering applications in OLEDs, in contrast, to photoexcitation, the singlet and triplet states occur in a ratio of 1 : 3 because the excited state is directly generated by the coupling of holes injected from the anode and electrons injected from the cathode. In the case of fluorescent materials, only 25% of the excited singlet can be involved in luminescence, while the remaining 75% is inactivated without being able to emit light. On the other hand, for phosphorescent materials, the emission state, *i.e.*, the lowest excited triplet state, can also generate from the singlet state via intersystem crossing so that the theoretical internal quantum yield can be expected to be 100 %. From this viewpoint, phosphorescent materials have extensively developed in the last three decades.

Since the radiative process of phosphorescence is spin forbidden, the radiative rates of phosphorescence are generally smaller than the non-radiative rates for organic materials. It is rare to observe phosphorescence from purely organic materials that do not contain heavy atoms at room temperature. On the other hand, in the case of metal complexes, the intersystem crossing is not a forbidden process as a result of the mixing of singlet and triplet states due to the strong spin-orbit coupling of the heavy atom, the central metal. Since phosphorescent metal complexes containing 5d and 4d metal ions such as Ir^{3+}, Pt^{2+}, and Ru^{2+} have been extensively studied because of phosphorescence, the transition from the lowest excited triplet (T_1) to the ground state (S_0), is strongly observed even at room temperature through such an intersystem crossing [7]
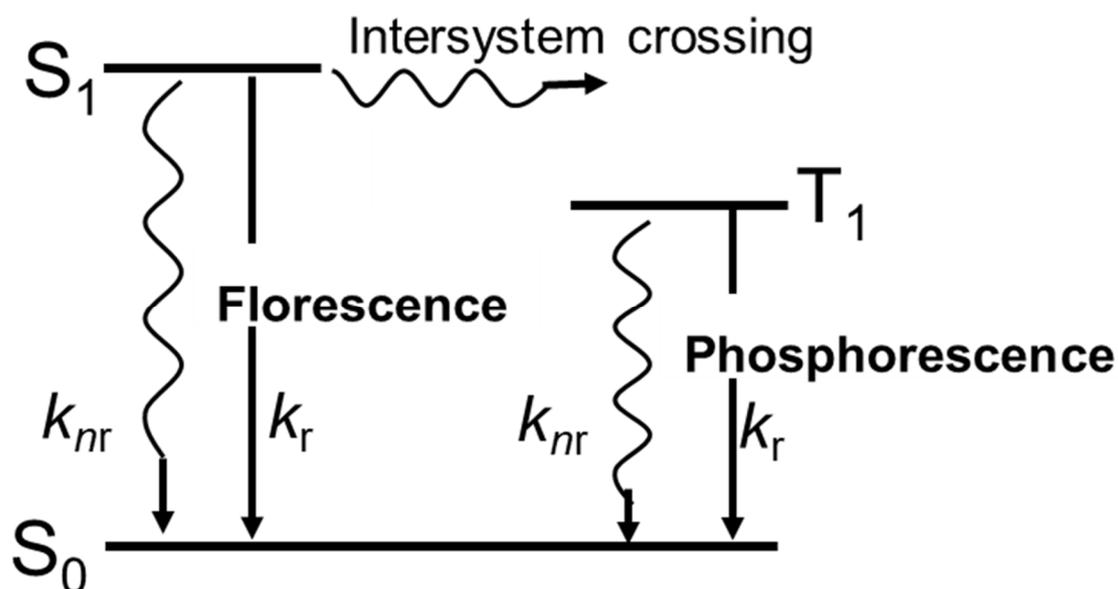

Figure 1. Jablonski diagram of fluorescence and phosphorescence

1.2 Phosphorescence metal complexes

This section describes the photophysical processes of phosphorescent metal complexes with unique features in detail. We consider a compound that, like many organic molecules, is in the singlet ground (S_0) state, in which all electron spins form a pair. The singlet excited state is reached by photoexcitation through a spin-allowed transition. If an excited singlet (S_n) state with a higher level than the lowest excited singlet (S_1) state is generated, an internal conversion occurs quickly, and the S_1 state rapidly relaxes. In general, the lowest excited triplet state (T_1), which is created by spin-flipping from the S_1 state, is lower level than the S_1 state, so an excited triplet (T_n) state is created from the S_1 state by intersystem crossing. Since intersystem crossing processes are accompanied by a spin-flip, the transition probability is generally low. In particular, the coupling between spin and orbital angular momenta is weak in organic molecules composed only of light atoms, and the conservation law of spin angular momentum holds approximately. Hence, the transition probabilities for intersystem crossing are very small. Since the non-radiative transition from the excited triplet state is very fast compared to the radiative rate of phosphorescence, it is rare to observe phosphorescence in organic compounds at room temperature. On the other hand, in compounds containing heavy atoms, the singlet and triplet states mix due to the strong spin-orbit coupling of the heavy atoms, and the intersystem crossing rate depends on the spin-orbit coupling. Therefore, the intersystem crossing speed of transition metal complexes is relatively fast. In fact, quantum chemical calculations have revealed that most of the excited states corresponding to the MLCT absorption band of *fac*-[Ir(ppy)$_3$] (ppy = 2-phenylpyridine), which exhibits strong phosphorescence properties, are a mixture of 30% singlet and 70% triplet states.[8] Thus, the singlet excited state produced by photoexcitation in transition metal complexes with strong spin-orbit coupling has a triplet character. The triplet state also has a particularly singlet character.

One method to investigate the character of excited triplets in detail is the analysis of zero-field splitting constant. In excited states involving heavy atom orbitals, the excited triplet state is split by spin-orbit coupling, so-called zero-field splitting(ZFS), resulting in multi-level emission from the sublevels.[9,10] In 1973, Crosby and co-workers found that [Ru(bpy)$_3$]$^{2+}$ dispersed in PMMA emission originated from three sublevels with energy intervals of 10 cm^{-1} and 60 cm^{-1} by analyzing the temperature dependence of the emission lifetime and emission quantum yields. [11] The first sublevel has a slow transition rate due to its pure triplet nature, while the third and second sublevels have large transition probabilities due to mixing with the singlet. The luminescence lifetime, especially at room temperature, is thought to be dominated by the transition rate of the third sublevel. Since then, luminescence lifetimes of various luminescent metal complexes have been analyzed. It was found that ^{3}MLCT luminescent complexes have a relatively large zero-field splitting constant (energy difference between the third and first sublevels: ΔE(ZFS)). In addition, complexes exhibiting a T_1 state of LC (ligand-centered) were also analyzed. It was found that the complexes with fast radiation rates are mixed with the higher ^{3}MLCTs to obtain high transition rates by using the spin-orbit coupling of the center metal. The analysis of ΔE(ZFS) was performed by assuming that the three sublevels of the triplet are in thermal equilibrium and that the distribution of each state follows a Boltzmann distribution, eq. 1[10] The

reported ΔE(ZFS) values (~200 cm^{-1}, Figure 2) are almost the same as thermal energy at room temperature (k_bT ≈ 209 cm^{-1}, 300 K), so the three sublevels are considered to be in thermal equilibrium at room temperature. Figure 2 summarizes typical complexes' ΔE(ZFS) and emission decay constant at room temperature. This figure shows that the MLCT transition has a larger ΔE(ZFS) and faster radiative rate than the LC transition, in which the metal orbital is less involved. Thus, ΔE(ZFS) analysis can provide information on the nature of the metal orbitals involved.

$$\tau = \frac{1}{k_{obs}} = \frac{1 + \exp\left(\frac{-E_1}{k_B T}\right) + \exp\left(\frac{-E_2}{k_B T}\right)}{k_0 + k_1 \exp\left(\frac{-E_1}{k_B T}\right) + k_2 \exp\left(\frac{-E_2}{k_B T}\right)} \quad (eq.\,1)$$
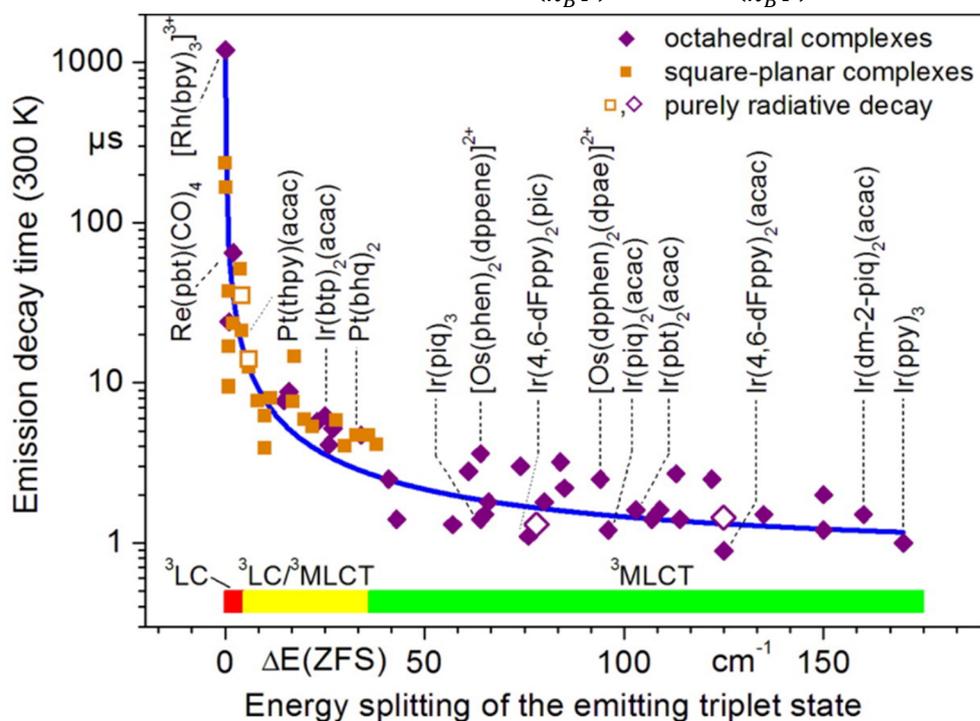
Figure 2. The ΔE(ZFS) and the emission decay constant at room temperature (300K) for typical luminescent metal complexes [10]

1.3 Assembly-induced emission of d⁸ metal complexes

1.3.1 Pt(II) complexes

It is well known that square planar Pt(II) complexes exhibit assembly-induced luminescence in crystals or highly concentrated solutions. To clarify the unique properties, Pt(II) complexes have been studied extensively from structural and electronical viewpoints.

Figure 3 shows that $5d_{z^2}$ orbitals overlap to form dσ and dσ* orbitals. The dσ and dσ* orbitals contain four electrons, so they are not the driving force of the assembly, but $6p_z$ orbitals also overlap to form pσ and pσ* orbitals. The mixing of dσ and pσ orbitals and dσ* and pσ* orbitals stabilize the orbital energy and lead to self-assembly.[12] The splitting width of the dσ and dσ* orbitals caused by the so-called " Pt···Pt Interaction" increases as the degree of overlap of the $5d_{z^2}$ orbitals increases. In other words, the energy of the dσ* orbital strongly depends on the Pt···Pt distance and stacking angle.

Figure 3. Schematic MO energy level diagram for Pt(II) complexes

Figure 4(a) shows that the absorption spectrum of $[Pt(CN)_4]^{2-}$ shows a concentration dependence, and a new absorption band appears at longer wavelengths under high concentration conditions. This absorption band can be assigned to that intra-metal (Pt dσ* to Pt 6pσ) transition, which originated from metal$\cdots$metal interaction.

Also, in solid states, $[Pt(CN)_4]^{2-}$ salts show broad emission originating from intra-metal excited states. In1970s, Day[13], Yersin[14–17], and other researchers[18,19] extensively studied about photophysical properties of excited state of $[Pt(CN)_4]^{2-}$ salts. As a result, it is well known that there is a strong correlation between emission as well as absorption energies and metal$\cdots$metal distances. (Figure 4(b)). The $[Pd(CN)_4]^{2-}$ salts, d^8 configuration same as$[Pt(CN)_4]^{2-}$, also shows a linear relationship between absorption energies and metal$\cdots$metal distances, but not observed luminescence.
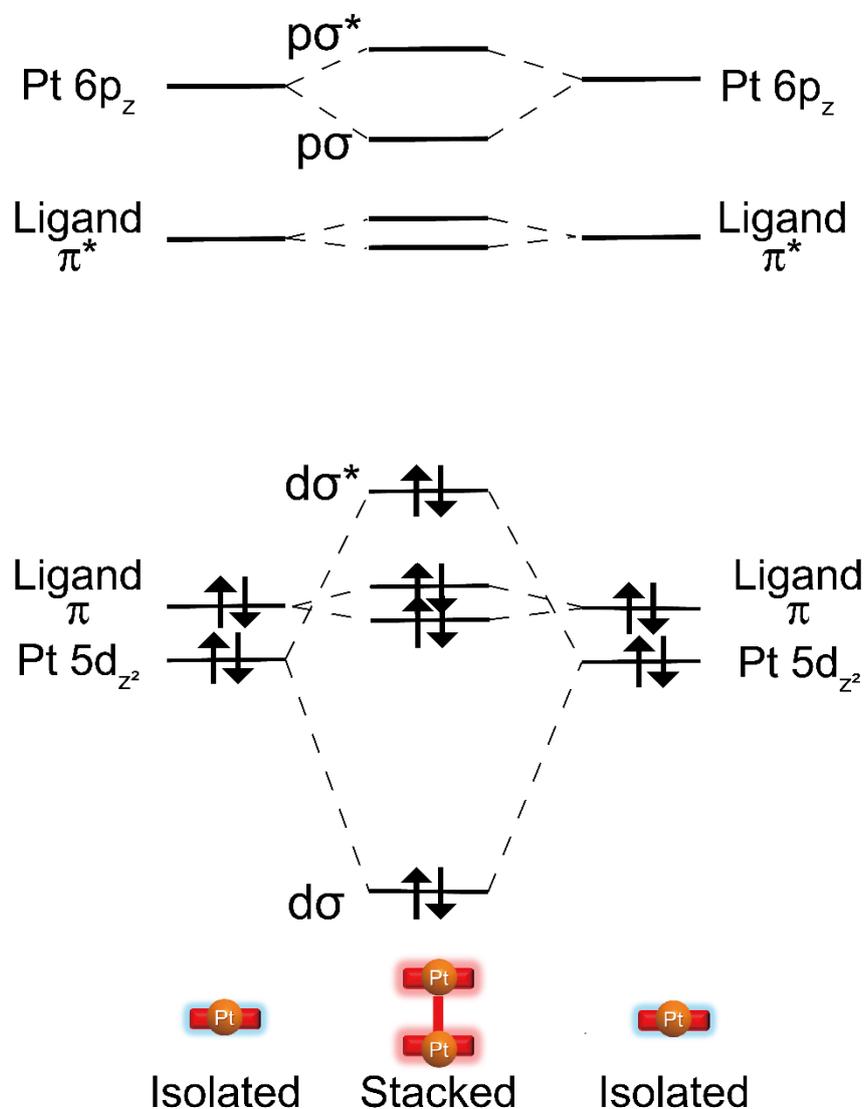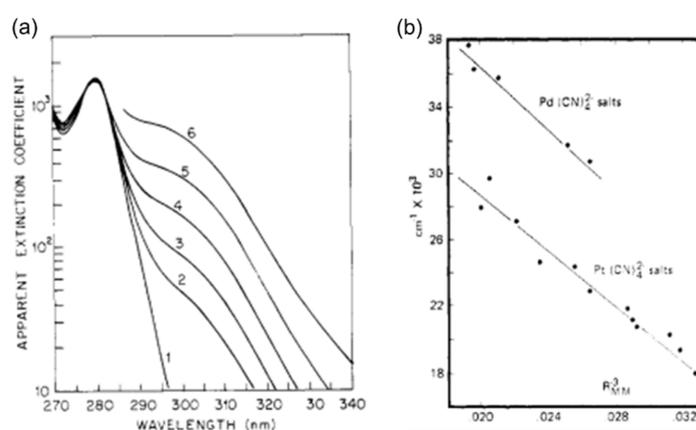

Figure 4. (a) Concentration dependence absorption spectra of $K_2[Pt(CN)_4]$ in aqueous solution. (1: 9.0×10^{-3} M, 2: 0.15 M, 2: 0.22 M, 3: 0.45 M, 4: 0.64 M [20] **(b)**Linear relationship of $[M(CN)_4]^{2-}$ (M=Pt, Pd)salts between R^{-3}(R: metal$\cdots$metal distance) and absorption (intra-metal dσ*pσ* transition) energy.[13]

Recently, Vlček, Gray, and co-workers reported dinuclear Pt(II) complex, Pt(pop-BF$_2$) (Figure X), unusually very slow ISC.[21,22] Pt(pop), the precursor of Pt(pop-BF$_2$), is also well-known as a typical Pt(II) complex that exhibits dual emission: intense green phosphorescence originated from ^{3}dσ*pσ* excited state, and weak fluorescence originated from ^{1}dσ*pσ* excited state.[23,24] The Pt(pop-BF$_2$) complex, in which the BF2 group bridges the hydroxy group of this typical POP complex, has a very slow intersystem crossing rate of more than 29 ns at 100 K. The total luminescence quantum yield was almost 100% even at room temperature, although interestingly, the ratio of fluorescence to phosphorescence showed a temperature dependence. The authors explain that the reason for this slow intersystem crossing is that the activation energy for structural relaxation, which is the shrinkage of the Pt$\cdots$Pt distance from S_1 to T_n, has been increased from rigidity due to cross-linking.

In this way, excited states involving metal$\cdots$metal interactions have the potential to tune not only the luminescence energy but also the overall photophysical processes, such as excitation dynamics, including inter-term crossing velocity, through their structure control.
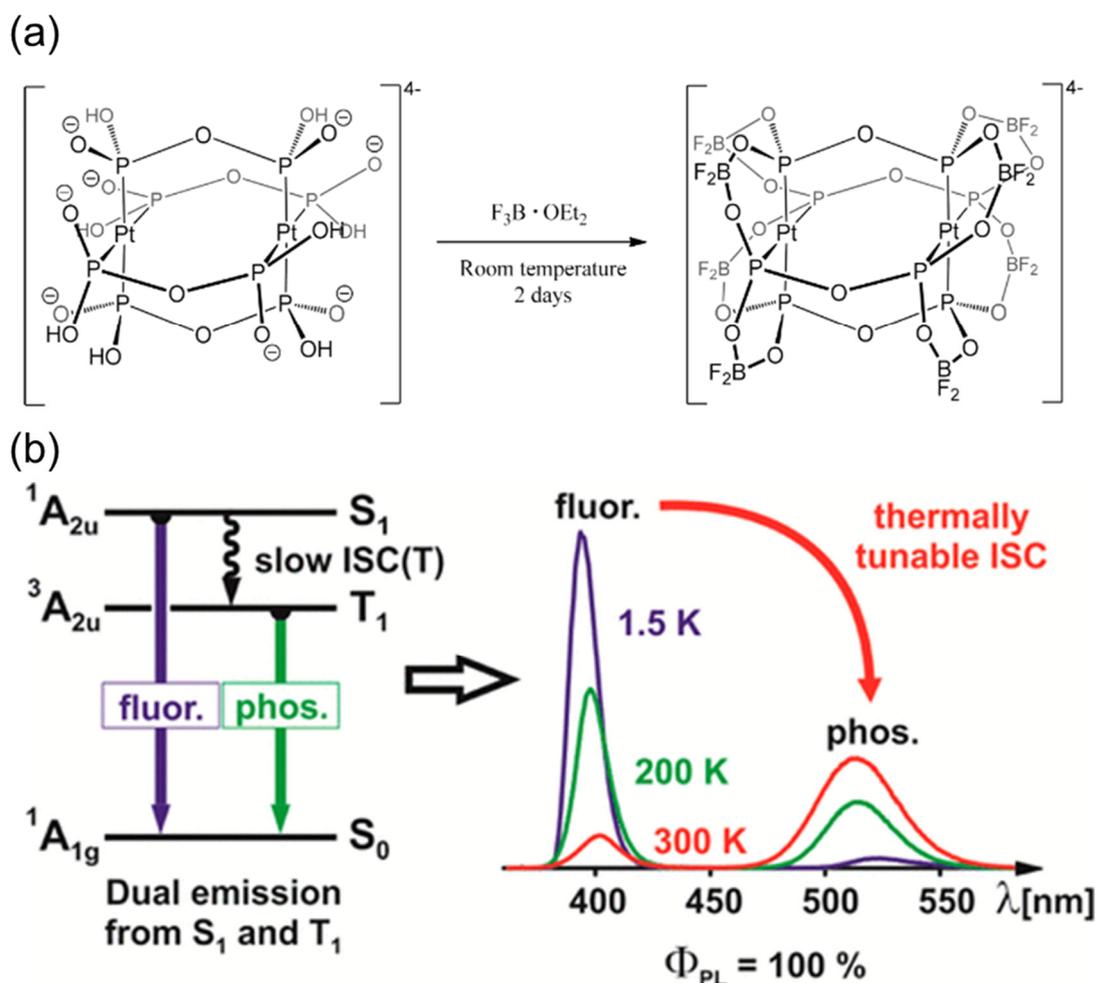
Figure 5. (a)Molecular structures of Pt(pop)(left) and Pt(pop-BF$_2$)(right), (b)schematic energy diagram of Pt(pop-BF$_2$) (left) and temperature dependence of emission spectra (right)[22]

Furthermore, introducing appropriate π-system ligands exhibits even more interesting properties and functionalities. The introduction of a ligand with a larger π-system, such as a bipyridine or its analog, such as a diimine ligand, results in characteristic absorption and emission properties derived from metal-to-metal-to-ligand charge transfer (MMLCT), a charge transfer transition from the dσ* orbital of metal to the π* orbital of ligand. Since the MMLCT absorption and emission properties sensitively reflect the Pt···Pt distance as well as dσ*pσ* transition.

The most representative example of a Pt(II)complex that exhibits ^{3}MMLCT emission with a bidentate chelate ligand is [Pt(bpy)Cl$_2$](bpy: 2,2'-bipyridine), its photophysical properties in the solid state reported by Miskiwski and Houlding in 1989.[25] [Pt(bpy)Cl$_2$] has two crystal polymorphs, red form with effective Pt···Pt interaction and yellow form without Pt···Pt interaction. The red form of [Pt(bpy)Cl$_2$] shows red emission and thermochromic behavior reported by Gay and co-workers in 1996[26], which originated from a slight change of Pt···Pt distance (Figure 6). The same thermochromic behavior was also reported for [Pt(bpy)CN$_2$].[27]
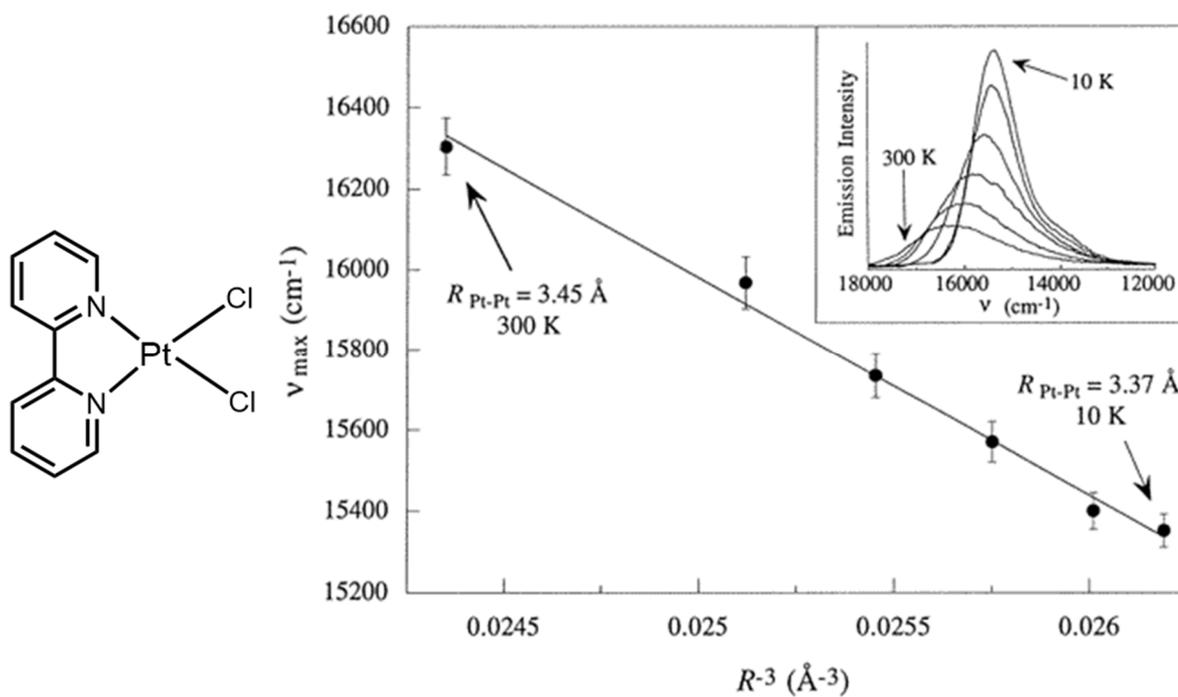
Figure 6. Molecular structure of [Pt(bpy)Cl$_2$](left), and linear relationship between R^{-3}(R: metal⋯metal distance) and ^{3}MMLCT emission energy(right).[26]

Another perspective on the properties of metal-metal interactions is supramolecular formation. The supramolecular chemistry of luminescent metal complexes based on metal···metal interaction is extensively studied[28–30], especially by Che[31], Yam[32,33], De Cola[34,35], and their co-workers.

De Cola and co-workers reported an outstanding example of supramolecular systems of luminescent Pt(II) complex in 2016.[34]   This complex is amphiphilic with a hydrophobic N^N^N-type tridentate ligand and a hydrophilic triethylene glycol chain. The supramolecular complex has two kinetically metastable phases and a thermodynamically stable phase. Each aggregate exhibits different luminescence properties, and the self-assembly formation was successfully imaged in real-time by fluorescence microscopy.
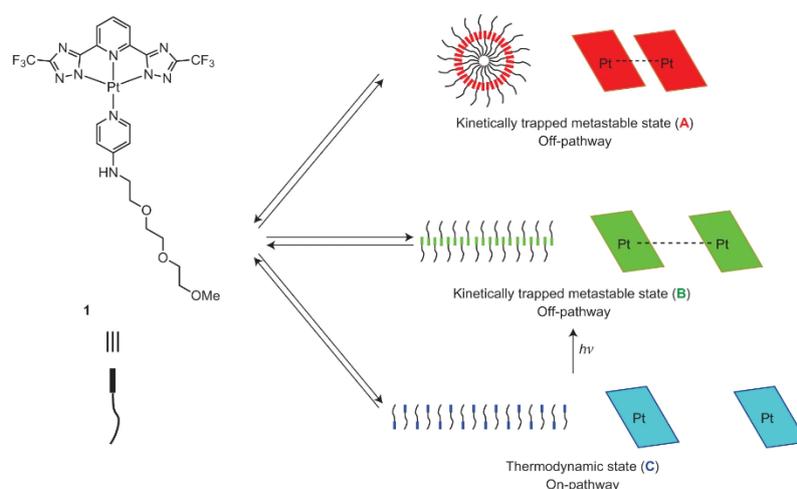
Figure 7. The schematic scheme of the supramolecular self-assemblies of Pt(II)complex.[34]

Back to the control of luminescence properties, an example of modulation of emission color in solution by controlling the inter Pt···Pt distance through molecular modification is the Pt(II) dinuclear complexes shown in Figure 8 ([Pt$_2$(4,6Fppy)$_2$(R-pz)$_2$] (4,6-Fppy = 2-(4,6-difluorophenyl)pyridinato 2-(4,6-difluorophenyl)pyridinato); R-pz = pyrazolate, 3-methyl-5-tert-butylpyrazolate or 3,5-di-tert-butylpyrazolate).[36] Thompson and co-workers reported that the intramolecular Pt···Pt distance interaction and luminescence color could be controlled by the bulkiness of the substituent introduced into the bridging ligand, pyrazolate. The Pt···Pt distance was 3.376 Å for pyrazolate (Figure 8), 3-methyl-5-tert-butylpyrazolate   for 3.046 Å. The 3.376 Å in the case of 3,5-bis(tert-butyl)pyrazolate pyrazolate shortens to 2.834 Å. In addition, the emission spectra obtained with the unsubstituted form show ^{3}LC spectra with vibrational structure. On the other hand, when 3-methyl-5-tert-butylpyrazolate is used, a broad emission spectrum with an emission maximum at 515 nm is attributed to ^{3}MMLCT. In the case of di(tert-butyl)pyrazolate, which has a further shorter Pt···Pt distance, the emission wavelength was extended to 570 nm.
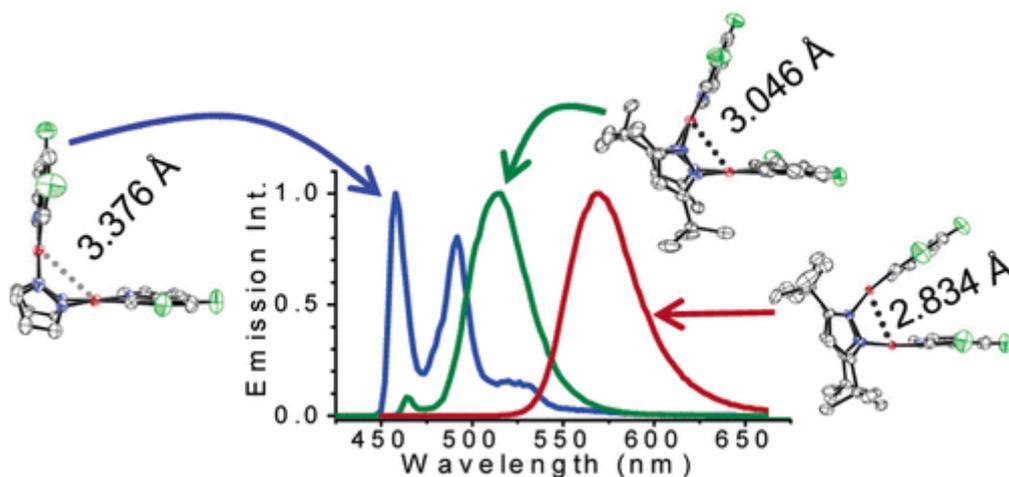
Figure 8. Molecular structures of [Pt$_2$(4,6Fppy)$_2$(R-pz)$_2$] determined by X-ray diffraction, and emission spectra in 2-MeTHF solution

As described above, the MMLCT luminescence properties of Pt(II) complexes have attracted much attention because the wavelength of the phosphorescence emission can be controlled by adjusting the Pt···Pt interactions in the crystal and solution. However, in most self-assembled systems of the square planar Pt(II) complexes, the ^{3}MMLCT emission is usually in the orange to the red color region because the MMLCT transition energy is lower than those of the metal-to-ligand charge transfer (MLCT) and ligand $\pi\pi^*$ transition energies. Using chelating ligands having carbanion or carbene, yellow to green emission originating from ^{3}MMLCT has been reported (Table 1, Figure 9). Nevertheless, a blue emission originating from ^{3}MMLCT has not been achieved yet.

Table 1. Pt(II) complexes that exhibit yellow to green ^{3}MMLCT emission.

Complex	Figure	color	λ_{max}^{em} / nm	Ref.
K[Pt(CN)$_2$(ptpy)]	(a)	yellow	558	[37]
[Pt$_2$(C^C*)$_2$(μ-N^N)$_2$]	(b)	yellow	561	[38]
[Pt(C^N^C)(Cl)]Cl	(c)	yellow	555	[39]
[Pt(N^C)(bipz)]	(d)	green	501	[40]
K[Pt(CN)$_2$(C^C*)]	(e)	green	502	[41]

ptpy = 2-(*p*-tolyl)pyridinate

H$_2$C^C* = 1-methyl-3-phenyl-1*H*-imidazolium

N^N = *N, N*-diphenylformamidinate

C^N^C = 2,6-bis(1-butylimidazol-2-ylidenyl)pyridine

N^C = 3-isopropyl-(pyrid-2-yl)-1*H*-imidazolylidene

bipz = 5,5'-di(trifluoromethyl)-3,3'-bipyrazolate

(a) λ_{max} = 558 nm

(b) λ_{max} = 561 nm

(c) λ_{max} = 555 nm

(d) λ_{max} = 501 nm

(e) λ_{max} = 502 nm
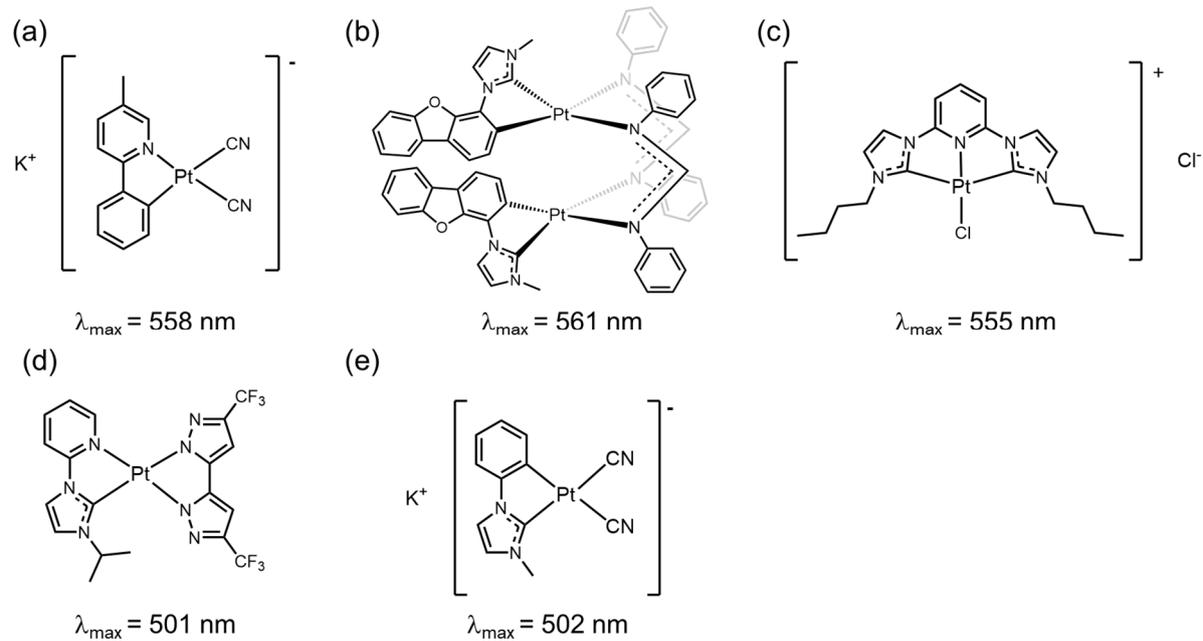
Figure 9. Molecular structures of Pt(II) complexes that exhibit yellow to green ^{3}MMLCT emission.

1.3.2 Other metal complexes with metal⋯metal interaction

The metal-metal interactions have been extensively investigated in other metal complex systems such as Au(I), Ag(I), Cu(I) complexes with the d^{10} configuration[7,42–44], and Rh(I) and Ir(I) complexes[12,45,46] with the same d^8 configuration as Pt(II) complexes.

On the other hand, palladium(II) complexes, homologous elements to platinum, have a smaller van der Waals radius(Pt: 1.75 Å, Pd: 1.63 Å).[47] For this reason, it is not expected to have a strong metal⋯metal interaction. However, several stacked structures by Pd⋯Pd/π⋯π have also been reported.[48–50] On the other hand, in considering excited states, it is known that the weak ligand field in a Pd(II) complex makes it easier to access the ^{3}dd excited state as a non-radiative process than in a Pt(II) complex. Consequently, few luminescence examples of palladium (II) complexes exist, and no MMLCT luminescence with clear evidence has been reported until recently.

In 2002, Neve and co-workers reported cyclometalated Pd(II) [Pd(L)Cl] (L=HL1: 6-phenyl-(2,2'-bipyridine)-4-carboxylic acid, HL2: 4-(6-phenyl-(2,2'-bipyridin)-4-yl)benzoic acid, L3: 4-(6-phenyl-(2,2'-bipyridin)-4-yl)phenol, (Figure 10a))complexes with C^N^N type tridentate ligands.[51] In the glass matrix at 77 K, [Pd(L1)Cl] and [Pd(L3)Cl] were observed emission with vibrational structure(Figure 10b), which can be assigned as triplet ligand-centered (^{3}LC). Only [Pd(L1)Cl] was successfully analyzed by X-ray structure analysis, and the Pd⋯Pd distances were 3.27 Å and 5.41 Å, suggesting the existence of a weak Pd⋯Pd interaction between the two neighboring molecules. (Figure 10c). Only [Pd(L1)Cl] showed a broad emission band (λ_{max}= 650 nm) at room temperature. (Figure 10d) The authors attributed this solid state emission to the presence of Pd⋯Pd interactions in the crystal. This emission assumed that the excimeric emission originated from the MMLCT state or combination of ππ*.
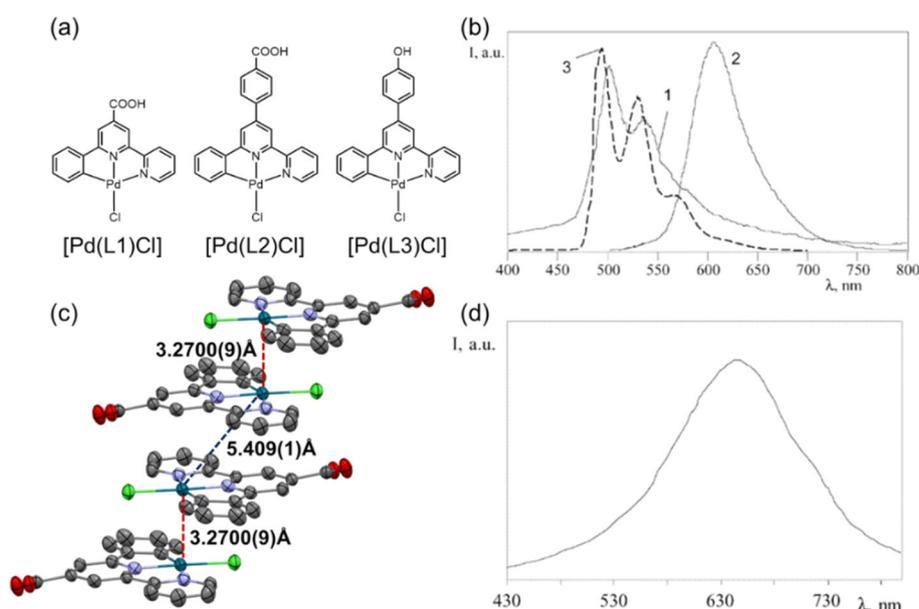
Figure 10. (a)Molecular structures of Pd(II) complexes, (b)Emission spectra at 77 K in a glass matrix (DMF/toluene = 1:1 v/v) 1 : [Pd(L1)Cl], 2 : [Pd(L2)Cl], 3 : [Pd(L2)Cl], (c)Packing structure of [Pd(L1)Cl], (d)Emission spectrum of [Pd(L1)Cl] at RT.[51]

In 2018, Che and co-workers reported ^{3}MMLCT emissive Pd(II) complexes with compelling evidence(Figure 11a). [31]   By changing the mixing ratio of acetonitrile-water of the Pd(II) solution, a new absorption band appeared, and luminescence were observed. The absorption and emission were assigned to ^{1}MMLCT absorption and ^{3}MMLCT emission, respectively, confirmed by X-ray crystallography and DFT/TDDFT calculations. Also, in 2018, Lu and co-workers reported ^{3}MMLCT emissive Pd(II) complexes exhibit vapochromic and mechanochromic behavior (Figure 11b).[52] Their groups also reported dinuclear Pd(II) complexes, which show highly emission not only in the solid state but also in the solution (PLQY up to 48% in the solution)(Figure 11c).[53] The intramolecular Pd···Pd distances were 3.2–3.3 Å in the crystal with red emission (λ_{max}=604 –640 nm). By computational studies, the emission originated from ^{3}MMLCT excited sate slightly mixed with ligand-to-ligand charge transfer (LLCT) character.

As described above, the number of examples of ^{3}MMLCT luminescent Pd(II) complexes is gradually increasing, but the molecular design is still in the under-explored stage.
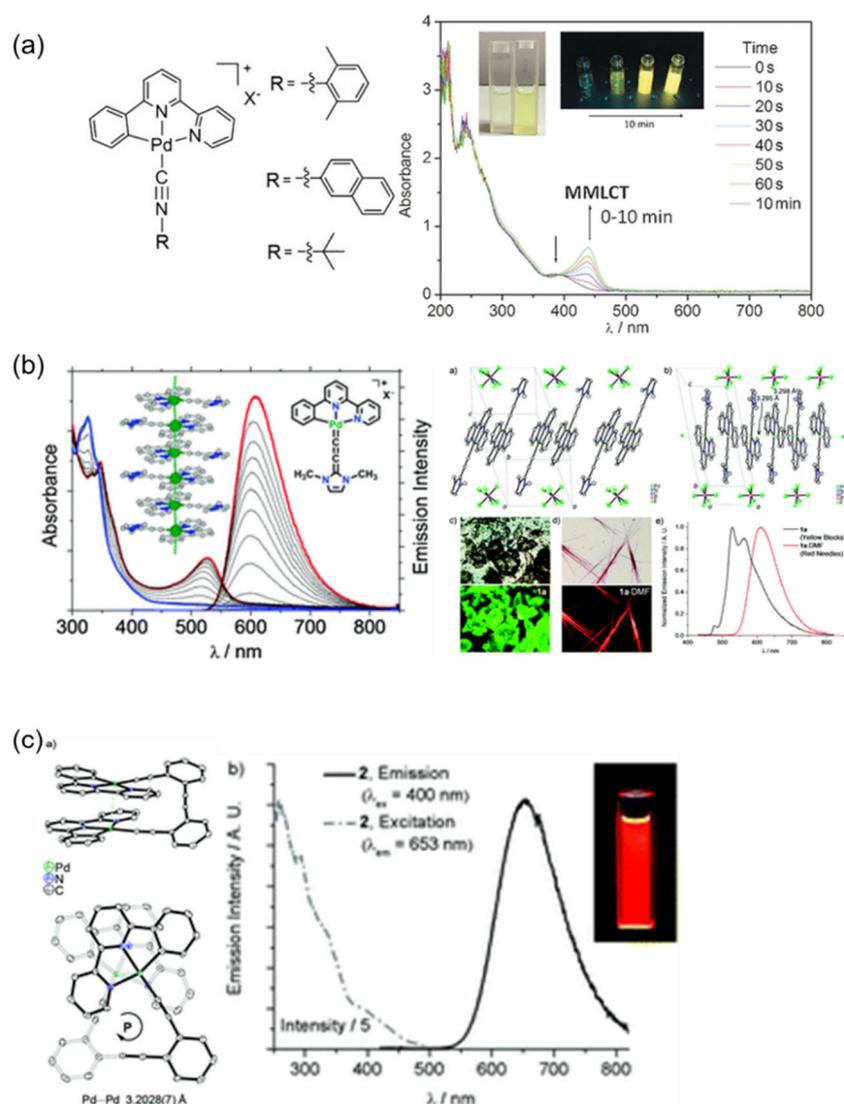
Figure 11. Examples of ^{3}MMLCT emissive Pd(II) complexes (a) ref.[31], (b)ref [52], (c)ref [53]

1.4 External stimulus responsive materials in the crystal states

The development of chromic materials that maintain crystallinity still remains a challenge. In recent years, many organic and metal complex crystals have been reported to change color and/or emission color in response to external stimuli (temperature, pressure, light, mechanical force, vapor, etc.). However, such chromic phenomena in the solid state are generally accompanied by a significant structural change, resulting in a decrease in crystallinity and a change to polycrystalline or amorphous. This makes it difficult to obtain structural information in the chromic materials with which structural changes are important. Although there are many reported examples of such chromic materials, very few show single crystal-to-single crystal (SCSC)-type structural transformation without losing their single crystallinity.

Many reviews and perspective articles[54–61] have been published on SCSC structural transitions from several perspectives. Small structural changes during the reaction are important in the SCSC structural transformation.[55,62] For example, Irie and co-workers reported photochromic reactions derived by the cyclization of some diarylethenes to proceed through the SCSC transformation.

On the other hand, maintaining crystallinity is considerably more complicated in a reaction system involving molecular insertion and release. There are examples associated with molecular adsorption and desorption in porous materials such as metal-organic frameworks (MOFs),[59–61] and hydrogen-bonded organic frameworks (HOFs) [63]where the framework structure is easily maintained.

However, a vapor-induced SCSC transformation, followed by the absorption and desorption of molecules, has been found only in limited systems.[64–68]   For example, Kato and co-workers reported the SCSC and associated vapochromism in a dinuclear Pt(II) complex, *syn*-[$Pt_2(bpy)_2(pyt)_2$](PF_6)$_2$ (bpy=2,2′-bipyridine, pyt=pyridine-2-thiolate) of due to desorption of acetonitrile molecules contained in crystals were revealed by temperature-variable single-crystal X-ray structure analysis (Figure 12a). [68,69] Ito and co-workers reported reverse vapor-induced SCSC transitions with luminesce color changes in Au(I) complexes with metal⋯metal interactions (Figure 12b).[66] Furthermore, in 2020, Ohba and co-workers reported a ligan exchange reaction via the SCSC process of luminescent Re(V) complex, (PPh_4)$_2$[ReN(CN)$_4$(ligands)](ligands= 4-cyanopyridine, MeOH), in which the luminescent color and luminescence origin change (Figure 12c).[67]

With this background, investigation of the dynamic process of SCSC conversion in vapochromic materials, in which relatively significant chemical compositional changes, such as vapor adsorption and desorption, occurs, is an important and challenging issue for the development of functions in high structural ordered systems.
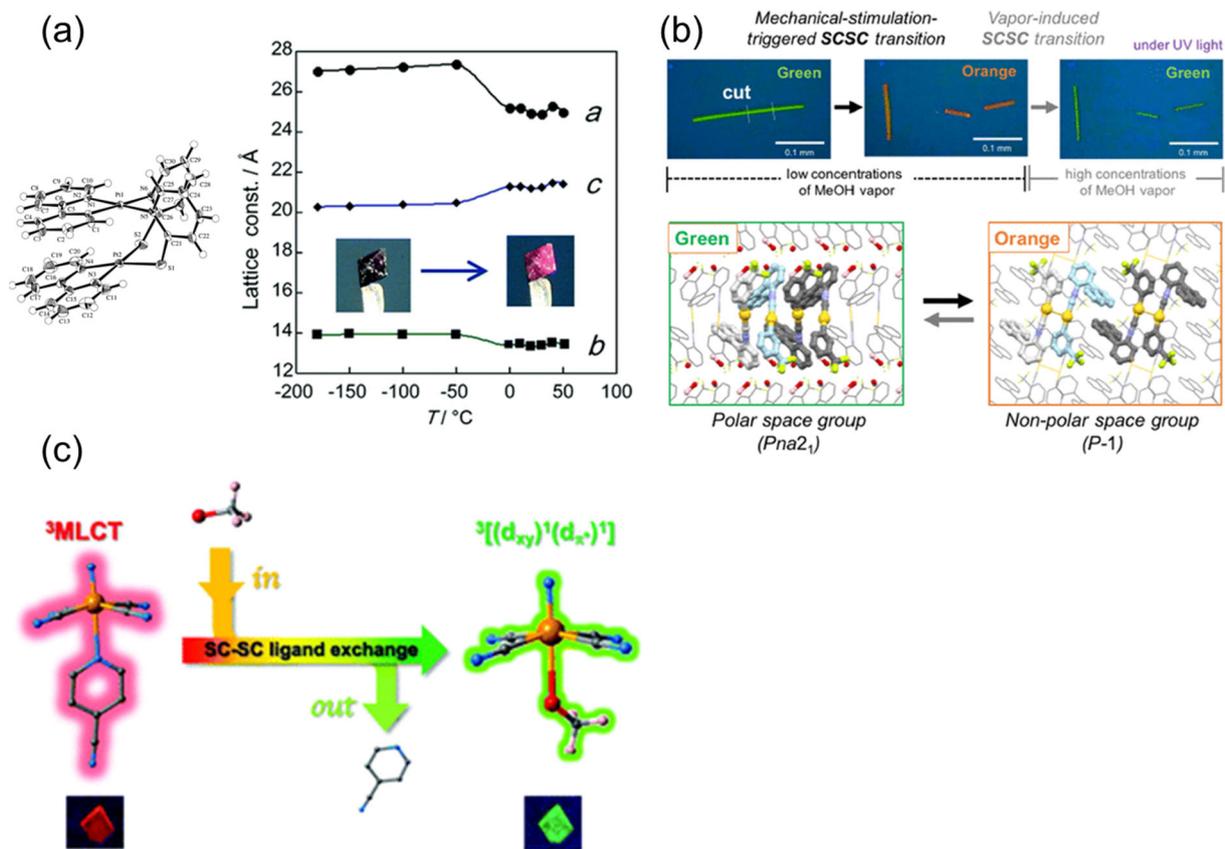
Figure 12. Several examples of vapor-induced SCSC

1.5 Purpose of this thesis

The MMLCT absorption and luminescence properties of Pt(II) complexes have been studied extensively because the photophysical properties change depending on a slight difference in the Pt···Pt distance. However, the MMLCT emission colors in the solid state have been reported to be mainly red (700 nm) to orange (580 nm), with very limited examples of yellow to green emission, so the control of emission colors in the solid state over the entire visible range remains a challenge. Very few examples of assembly-induced luminescence in Pd(II) complexes have the same d^8 electron configuration as that of Pt(II) complexes.

This thesis focused on self-assembled Pt(II) and Pd(II) complexes and developed a control method for their luminescence properties by controlling their crystal structures.

N-heterocyclic carbenes were used as ligands, and tuning of platinum-platinum interactions by controlling the crystal structure was investigated by changing the bulkiness of the introduced substituents. Four novel Pt(II) complexes, [Pt(CN)$_2$(R-impy)] (R-impy = 1-alkyl-3-(2-pyridyl)-1H-imidazol-2-ylidene, R = Me, Et, ^{i}Pr and ^{t}Bu) were synthesized and its crystal structure and luminescence properties were measured. In order to investigate the correlation between crystal structure and luminescence properties in more detail, temperature-variable single crystal X-ray structure analysis and luminescence spectra measurements were performed.

The Pt···Pt interaction, a type of intermolecular interaction, is an important factor in the formation of the assembled structure of Pt(II) complexes, competing with other intermolecular interactions. Therefore, I focused on complex [Pt(CN)$_2$(^{t}Bu-impy)] with weak Pt interactions and investigated its vapor responsiveness in expecting a flexible response to external stimuli based on the weak interactions.

To further investigate self-assembled d^8 metal complexes, I focused on tridentate ligands, which are more rigid than bidentate ligands and are expected to have more intense luminescence. The Pt(II) and Pd(II) complexes with CNC ligands having two NHC moieties, [M(bisimpy)CN]PF$_6$ (M = Pt, Pd; bisimpy= 2,6-bis(3-methyl-1H-imidazol-2-ylidene)pyridine) were synthesized, and its crystal structure and luminescence properties were measured. The crystals of [Pd(bisimpy)CN]PF$_6$ exhibit thermochromic behavior, and to investigate this behavior, the relationship between crystal structure and luminescence properties is discussed.
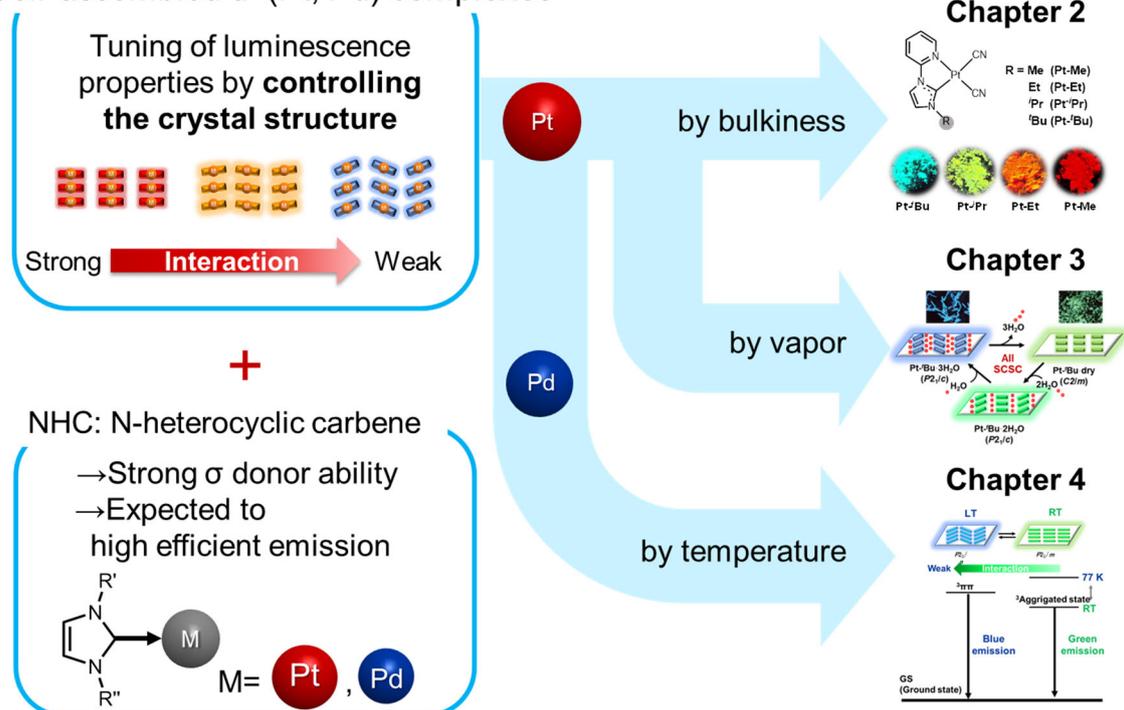
Figure 13. Outline the purpose of this theis

1.6 Outline of this thesis

This doctoral thesis consists of five chapters, briefly described in this section.

Chapter 1 describes the research background and purpose of this thesis with important references.

In chapter 2, the synthesis, crystal structure, and photophysical properties of P (II) complexes, [Pt(CN)$_2$(R-impy)] ((R-impy = 1-alkyl-3-(2-pyridyl)-1H-imidazol-2-ylidene, R = Me, Et, ^{i}Pr and ^{t}Bu) were described. As a result, intense blue emission originating from the triplet metal–metal-to-ligand charge transfer (^{3}MMLCT) state has been achieved by the fine control of the stacking structure of Pt(II) complexes bearing an N-heterocyclic carbene (NHC). By the slight change of the stacking structures based on the steric effect of a substituent on the NHC ligand, the luminescence color is fully tuned from red to blue without changing the emission origin (*i.e.*, ^{3}MMLCT).
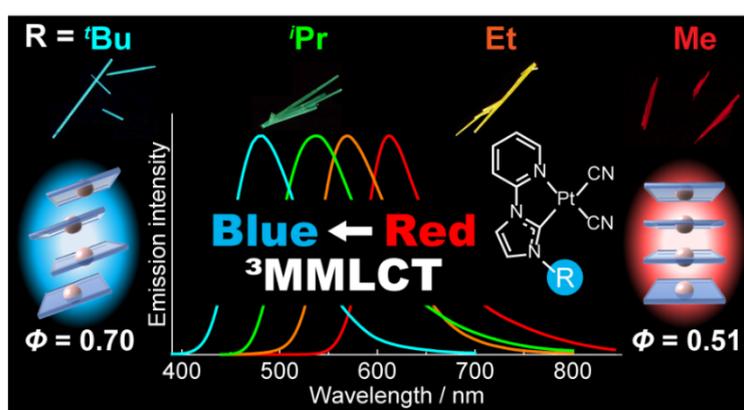
Figure 14. Schematic image of emission color tuning by control of Pt···Pt interaction

In chapter 3, the vapor-induced single-crystal-to-single-crystal (SCSC) transformations and vapochromic luminescence behavior of [Pt(CN)$_2$(^{t}Bu-impy)] were described. The vapor-induced reversible and stepwise single-crystal-to-single-crystal (SCSC) transformations were elucidated by variable-temperature and continuous in-situ tracking of single-crystal X-ray diffraction measurements. The blue MMLCT emission of 4 in response to the vapor atmosphere and emission color changed from blue to yellowish-green, although the single crystallinity and luminescence intensity are maintained.
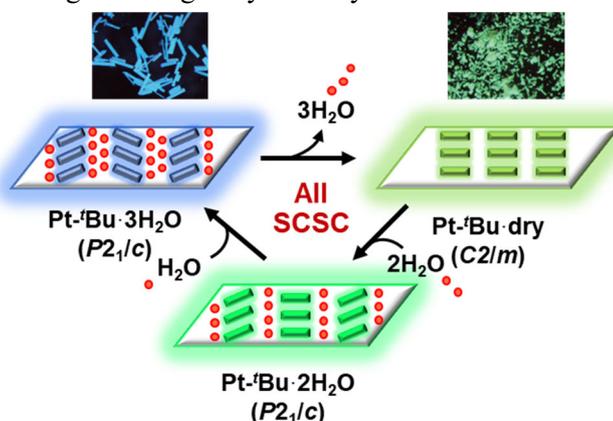
Figure 15. Schematic diagram of structural changes in vapor-induced reversible and stepwise SCSC transition of [Pt(CN)$_2$(^{t}Bu-impy)]

In chapter 4, the synthesis, crystal structure, and photophysical properties of Pt(II) and Pd(II)complexes, [M(bisimpy)CN]PF$_6$ (M = Pt, Pd; bisimpy= 2,6-bis(3-methyl-1*H*-imidazol-2-ylidene)pyridine) were described. The effect of the C^N^C tridentate ligand, including two NHCs, on photophysical properties, was investigated. Both Pt(II) and Pd(II) complexes self-assembled infinite 1D chains by intermolecular interaction. Interestingly, [Pd(bisimpy)CN]PF$_6$ shows thermochromic behavior corresponding to a slight change in stacking structure. This study shows that a new type of assembly-induced luminescence from NHC orbitals involves MMLCT excited states and provides a new approach to developing assembly-induced luminescence in d^8 metal complexes.
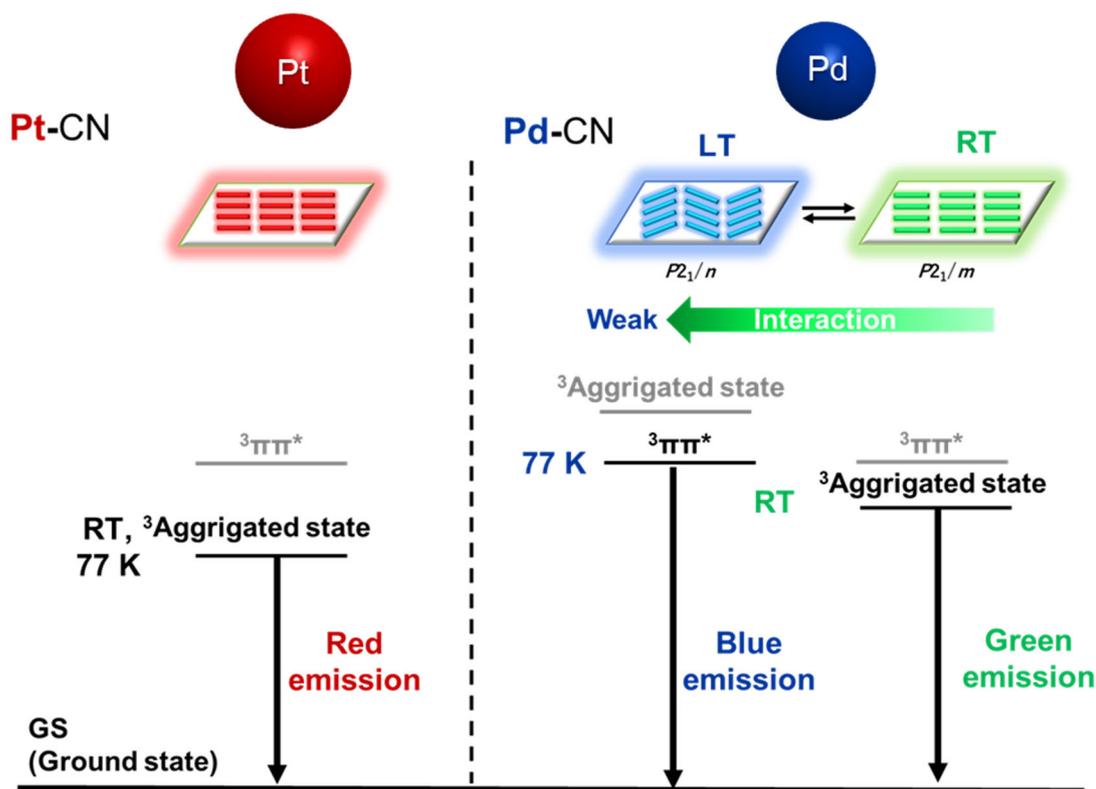
Figure 16. Schematic diagram of the difference in photophysical properties between Pt(II) and Pd(II)

In chapter 5, the general conclusion and future perspective of this doctoral thesis are described.

References

[1] M. A. Baldo, M. E. Thompson, S. R. Forrest, *Nature* **2000**, *403*, 750–753.

[2] M. A. Baldo, D. F. O'Brien, Y. You, A. Shoustikov, S. Sibley, M. E. Thompson, S. R. Forrest, *Nature* **1998**, *395*, 151–154.

[3] V. Adamovich, J. Brooks, A. Tamayo, A. M. Alexander, P. I. Djurovich, B. W. D'Andrade, C. Adachi, S. R. Forrest, M. E. Thompson, *New. J. Chem.* **2002**, *26*, 1171–1178.

[4] Z. Lin, R. Kabe, K. Wang, C. Adachi, *Nat. Commun.* **2020**, *11*, 191.

[5] S. Scholz, D. Kondakov, B. Lüssem, K. Leo, *Chem. Rev.* **2015**, *115*, 8449–8503.

[6] M. Kato, *Bull. Chem. Soc. Jpn.* **2007**, *80*, 287–294.

[7] V. W.-W. Yam, V. K.-M. Au, S. Y.-L. Leung, *Chem. Rev.* **2015**, *115*, 7589–7728.

[8] K. Nozaki, *J. Chin. Chem. Soc.* **2006**, *53*, 101–112.

[9] H. Yersin, J. Strasser, *Coord. Chem. Rev.* **2000**, *208*, 331–364.

[10] H. Yersin, A. F. Rausch, R. Czerwieniec, T. Hofbeck, T. Fischer, *Coord. Chem. Rev.* **2011**, *255*, 2622–2652.

[11] R. W. Harrigan, G. D. Hager, G. A. Crosby, *Chem. Phys. Lett.* **1973**, *21*, 487–490.

[12] H. B. Gray, S. Záliš, A. Vlček, *Coord. Chem. Rev.* **2017**, *345*, 297–317.

[13] P. Day, *J. Am. Chem. Soc.* **1975**, *97*, 1588–1589.

[14] H. Yersin, I. Hidvegi, G. Gliemann, M. Stock, *Phys. Rev. B.* **1979**, *19*, 177–180.

[15] H. Yersin, G. Gliemann, *Ann. Ny. Acad. Sci.* **1978**, *313*, 539–559.

[16] U. Rössler, H. Yersin, *Phys. Rev. B.* **1982**, *26*, 3187–3191.

[17] G. Gliemann, H. Yersin, *Struct. Bond.* **2005**, 87–153.

[18] A. Lechner, G. Gliemann, *J. Am. Chem. Soc.* **1989**, *111*, 7469–7475.

[19] T. W. Thomas, A. E. Underhill, *Chem. Soc. Rev.* **1972**, *1*, 99–120.

[20] J. W. Schindler, R. C. Fukuda, A. W. Adamson, *J. Am. Chem. Soc.* **1982**, *104*, 3596–3600.

[21] A. C. Durrell, G. E. Keller, Y.-C. Lam, J. Sýkora, A. Vlček, H. B. Gray, *J. Am. Chem. Soc.* **2012**, *134*, 14201–14207.

[22] T. Hofbeck, Y. C. Lam, M. Kalbáč, S. Záliš, A. Vlček, H. Yersin, *Inorg. Chem.* **2016**, *55*, 2441–2449.

[23] R. M. van der Veen, A. Cannizzo, F. van Mourik, A. Vlček, M. Chergui, *J. Am. Chem. Soc.* **2011**, *133*, 305–315.

[24] R. M. van der Veen, C. J. Milne, A. E. Nahhas, F. A. Lima, V. Pham, J. Best, J. A. Weinstein, C. N. Borca, R. Abela, C. Bressler, M. Chergui, *Angew. Chem. Int. Ed.* **2009**, *48*, 2711–2714.

[25] V. M. Miskowski, V. H. Houlding, *Inorg. Chem.* **1989**, *28*, 1529–1533.

[26] W. B. Connick, L. M. Henling, R. E. Marsh, H. B. Gray, *Inorg. Chem.* **1996**, *35*, 6261–6265.

[27] M. Kato, C. Kosuge, K. Morii, J. S. Ahn, H. Kitagawa, T. Mitani, M. Matsushita, T. Kato, S. Yano, M. Kimura, *Inorg. Chem.* **1999**, *38*, 1638–1641.

[28] S. G. Kang, K. Y. Kim, Y. Cho, D. Y. Jeong, J. H. Lee, T. Nishimura, S. S. Lee, S. K. Kwak, Y. You, J. H. Jung, *Angew. Chem. Int. Ed.* **2022**, *61*, e202207310.

[29] G. Ghosh, T. Ghosh, G. Fernández, *Chempluschem.* **2020**, *85*, 1022–1033.

[30] Y. Han, Z. Gao, C. Wang, R. Zhong, F. Wang, *Coord. Chem. Rev.* **2020**, *414*, 213300.

[31] Q. Wan, W. To, C. Yang, C. Che, *Angew. Chem. Int. Ed.* **2018**, *57*, 3089–3093.

[32] M.-Y. Leung, S. Y.-L. Leung, K.-C. Yim, A. K.-W. Chan, M. Ng, V. W.-W. Yam, *J. Am. Chem. Soc.* **2019**, *141*, 19466–19478.

[33] Y. Li, L. Chen, Y. Ai, E. Y.-H. Hong, A. K.-W. Chan, V. W.-W. Yam, *J. Am. Chem. Soc.* **2017**, *139*, 13858–13866.

[34] A. Aliprandi, M. Mauro, L. D. Cola, *Nat. Chem.* **2016**, *8*, 10–15.

[35] G. Moreno-Alcántar, A. Aliprandi, R. Rouquette, L. Pesce, K. Wurst, C. Perego, P. Brüggeller, G. M. Pavan, L. D. Cola, *Angew. Chem. Int. Ed.* **2021**, *60*, 5407–5413.

[36] B. Ma, J. Li, P. I. Djurovich, M. Yousufuddin, R. Bau, M. E. Thompson, *J. Am. Chem. Soc.* **2005**, *127*, 28–29.

[37] T. Ogawa, M. Yoshida, H. Ohara, A. Kobayashi, M. Kato, *Chem. Commun.* **2015**, *51*, 13377–13380.

[38] H. Leopold, M. Tenne, A. Tronnier, S. Metz, I. Münster, G. Wagenblast, T. Strassner, *Angew. Chem. Int. Ed.* **2016**, *55*, 15779–15782.

[39] C.-S. Lee, S. Sabiah, J.-C. Wang, W.-S. Hwang, I. J. B. Lin, *Organometallics.* **2010**, *29*, 286–289.

[40] C.-W. Hsu, K. T. Ly, W.-K. Lee, C.-C. Wu, L.-C. Wu, J.-J. Lee, T.-C. Lin, S.-H. Liu, P.-T. Chou, G.-H. Lee, Y. Chi, *Acs. Appl. Mater. Inter.* **2016**, *8*, 33888–33898.

[41] T. Ogawa, W. M. C. Sameera, M. Yoshida, A. Kobayashi, M. Kato, *Dalton. Trans.* **2018**, *47*, 5589–5594.

[42] C.-M. Che, S.-W. Lai, *Coord. Chem. Rev.* **2005**, *249*, 1296–1309.

[43] D. L. Phillips, C.-M. Che, K. H. Leung, Z. Mao, M.-C. Tse, *Coord. Chem. Rev.* **2005**, *249*, 1476–1490.

[44] L. M. C. Luong, M. A. Malwitz, V. Moshayedi, M. M. Olmstead, A. L. Balch, *J. Am. Chem. Soc.* **2020**, *142*, 5689–5701.

[45] K. R. Mann, J. G. Gordon, H. B. Gray, *J. Am. Chem. Soc.* **1975**, *97*, 3553–3555.

[46] K. Uemura, *Dalton. Trans.* **2016**, *46*, 5474–5492.

[47] A. Bondi, *J. Phys. Chem.* **1964**, *68*, 441–451.

[48] B. Oskui, M. Mintert, W. S. Sheldrick, *Inorg. Chim. Acta.* **1999**, *287*, 72–81.

[49] S.-W. Lai, T.-C. Cheung, M. C. W. Chan, K.-K. Cheung, S.-M. Peng, C.-M. Che, *Inorg. Chem.* **2000**, *39*, 255–262.

[50] M. J. Mayoral, C. Rest, V. Stepanenko, J. Schellheimer, R. Q. Albuquerque, G. Fernández, *J. Am. Chem. Soc.* **2013**, *135*, 2148–2151.

[51] F. Neve, A. Crispini, C. D. Pietro, S. Campagna, *Organometallics.* **2002**, *21*, 3511–3518.

[52] C. Zou, J. Lin, S. Suo, M. Xie, X. Chang, W. Lu, *Chem. Commun.* **2018**, *54*, 5319–5322.

[53] J. Lin, C. Zou, X. Zhang, Q. Gao, S. Suo, Q. Zhuo, X. Chang, M. Xie, W. Lu, *Dalton. Trans.* **2019**, *48*, 10417–10421.

[54] I. Halasz, *Cryst. Growth. Des.* **2010**, *10*, 2817–2823.

[55] A. Chaudhary, A. Mohammad, S. M. Mobin, *Cryst. Growth. Des.* **2017**, *17*, 2893–2910.

[56] M. E. van der Boom, *Angew. Chem. Int. Ed.* **2011**, *50*, 11846–11848.

[57] J.-G. Yu, M.-M. Gan, S. Bai, Y.-F. Han, *Crystengcomm* **2019**, *21*, 4673–4683.

[58] S. Kobatake, M. Irie, *Bull. Chem. Soc. Jpn.* **2004**, *77*, 195–210.

[59] J. J. Vittal, *Coord. Chem. Rev.* **2007**, *251*, 1781–1795.

[60] C.-P. Li, J. Chen, C.-S. Liu, M. Du, *Chem. Commun.* **2014**, *51*, 2768–2781.

[61] E. Fernandez-Bartolome, A. Martinez-Martinez, E. Resines-Urien, L. Piñeiro-Lopez, J. S. Costa, *Coord. Chem. Rev.* **2022**, *452*, 214281.

[62] S. Reinoso, B. Artetxe, J. M. Gutiérrez-Zorrilla, *Acta. Crystallogr. Sect. C* **2018**, *74*, 1222–1242.

[63] A. J. Sindt, M. D. Smith, S. Berens, S. Vasenkov, C. R. Bowers, L. S. Shimizu, *Chem. Commun.* **2019**, *55*, 5619–5622.

[64] A. Iturrospe, B. Artetxe, S. Reinoso, L. S. Felices, P. Vitoria, L. Lezama, J. M. Gutiérrez-Zorrilla, *Inorg. Chem.* **2013**, *52*, 3084–3093.

[65] S. Khatua, S. Goswami, S. Biswas, K. Tomar, H. S. Jena, S. Konar, *Chem. Mater.* **2015**, *27*, 5349–5360.

[66] M. Jin, T. Sumitani, H. Sato, T. Seki, H. Ito, *J. Am. Chem. Soc.* **2018**, *140*, 2875–2879.

[67] K. Sasaki, H. Yamate, H. Yoshino, H. Miura, Y. Shimoda, K. Miyata, K. Onda, R. Ohtani, M. Ohba, *Chem. Commun.* 2020, *56*, 12961–12964.

[68] T. Ohba, A. Kobayashi, H.-C. Chang, M. Kato, *Dalton Trans.* **2013**, *42*, 5514–5523.

[69] M. Kato, A. Omura, A. Toshikawa, S. Kishi, Y. Sugimoto, *Angew. Chem. Int. Ed.* **2002**, *41*, 3183–3185.

Chapter 2

Wide-range Color Tuning of Highly Luminescent One-dimensional Platinum(II) Complexes with *N*-heterocyclic Carbenes

2.1 Introduction

Self-assembly based on weak intermolecular interactions is essential for constructing supramolecular systems and can be the key to functionalization in various systems such as organic crystals, metal-complex systems, polymers, and biosystems.[1–3] Pt(II) complexes have occupied a unique position for a long time because of their square-planar coordination geometry, which leads to assembly-induced luminescence as well as coloration owing to the Pt···Pt electronic interactions.[4,5] Thus, Pt(II) complexes have recently attracted significant attention for application in biological imaging[6] and biomimetic systems.[7] Typically, square-planar Pt(II) complexes with a d^8 electronic configuration form bonding $d\sigma$ and antibonding $d\sigma^*$ orbitals by the overlapping of the occupied dz^2 orbitals in their stacked forms with short Pt···Pt contacts. When appropriate aromatic ligands are introduced into such systems, they often exhibit characteristic light absorption/emission based on a charge transfer transition between the $d\sigma^*$ orbital and the π^* orbital of the ligand, the so-called metal-metal-to-ligand charge transfer (MMLCT) transition (Figure 1).[8] The assembly-induced luminescent systems are fascinating because an intense emission can occur even if the monomeric unit is non-emissive. In addition, these systems are free from the problem of the so-called aggregation caused quenching,[9] while aggregation induced emission has also been developed by sophisticated molecular design.[10]

The MMLCT absorption/emission energies distinctly reflect the intermolecular Pt···Pt interactions determined by the Pt···Pt distances and the orientation of the stacks; that is, the Pt···Pt interaction can change sensitively when the stack is inclined from the parallel arrangement (A→B in Figure 1), and the effect increases for the shifted stack formed by the effect of the ligands (C in Figure 1). Assembly-induced luminescence has been investigated based on the design of ligands for the assembled systems to develop sensor materials for heat, pressure, volatile organic compounds, and other stimuli.[4,5] However, since self-assembled structures are controlled by various factors kinetically and thermodynamically,[11] the construction of desired structures with precisely controlled Pt···Pt distances is difficult not only in solution, but also in the crystal state.[12] Self-assembly systems with metal-metal interactions have been developed for other metal complexes, such as Rh(I) and Pd(II) complexes with the same d^8 configuration as that of Pt(II) complexes,[13] and Au(I) and Ag(I) complexes with a d^{10} configuration.[14–17] However, the wide and fine control of metal···metal distances has not been systematically investigated.
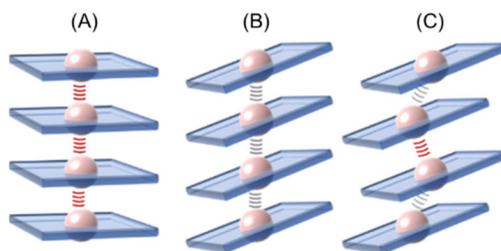
Figure 1. Schematic stacking features for infinite chains of Pt(II) complexes that affect the Pt···Pt interactions (drawn as stacked tetramers): (A) parallel stack, (B) oblique stack with equivalent Pt···Pt distances, (C) oblique stack with inequivalent Pt···Pt distances.

In most self-assembled systems of the square-planar Pt(II) complexes, the ^{3}MMLCT emission usually occurs in the color regions of orange to red because the MMLCT transition energy is lower than those of the metal-to-ligand charge transfer (MLCT) and ligand $\pi\pi^*$ transition energies. To realize MMLCT with a higher energy, it is essential to construct Pt(II) complex systems with moderate Pt$\cdots$Pt interactions and appropriate π-acceptor ligands. In addition, strong ligand fields are favorable for highly efficient luminescence because the rise of the dd state would suppress non-radiative deactivation,[18] while rigid structures would suppress vibrational deactivation.[19] Using chelating ligands having carbanion or carbene, yellow to green emission originating from ^{3}MMLCT has been reported.[20–24] However, a blue emission originating from ^{3}MMLCT has not been achieved yet. For this purpose, the introduction of a ligand with moderate π-conjugation and π-accepting properties is important in addition to the construction of weak Pt$\cdots$Pt stacks.

Table 1. Pt(II) complexes that exhibit yellow to green ^{3}MMLCT emission.

Complex	color	λ_{max}^{em} / nm	Ref.
K[Pt(CN)$_2$(ptpy)]	yellow	558	20
[Pt$_2$(C^C*)$_2$(μ-N^N)$_2$]	yellow	561	21
[Pt(C^N^C)(Cl)]Cl	yellow	555	22
[Pt(N^C)(bipz)]	green	501	23
K[Pt(CN)$_2$(C^C*)]	green	502	24

ptpy = 2-(*p*-tolyl)pyridinate

H$_2$C^C* = 1-methyl-3-phenyl-1*H*-imidazolium

N^N = *N,N*-diphenylformamidinate

C^N^C = 2,6-bis(1-butylimidazol-2-ylidenyl)pyridine

N^C = 3-alkyl-1-(pyrid-2-yl)-1H-imidazolylidene derivatives

bipz = 5,5'-di(trifluoromethyl)-3,3'-bipyrazolate

Blue phosphorescent materials have been developed based on the ligand centered $^3\pi\pi^*$ emission or mixed $^3\pi\pi^*/^3$MLCT emission using cyclometalated Ir(III) and Pt(II) complexes for application in organic light-emitting diodes (OLEDs).[25–27] However, the relatively long exciton lifetimes based on the $^3\pi\pi^*$ emission (> several microseconds) were a problem for efficient blue OLEDs.[28] In addition, the $^3\pi\pi^*$ emission of metal complexes often suffers from quenching due to aggregation, as in the case of the organic emitters.[28]

In this context, blue emitters with ^{3}MMLCT-based emission are intriguing and desirable because they can provide intensely luminescent materials with favorable emission lifetimes (< 1 µs). In addition, materials with assembly-induced luminescence enable the facile fine-tuning of luminescence color while

maintaining a high emission quantum yield. To realize blue ^{3}MMLCT emission, it is essential to make ^{3}MMLCT the lowest triplet excited state instead of the $^3\pi\pi^*$ state, which is a common emission state in the blue region for many luminescent complex systems including aromatic ligands. Considering this, ligands that can provide not only a stable and strong ligand field, but also an appropriate π^* orbital should be chosen. In addition, to control the color of the ^{3}MMLCT emission in the entire visible region from red to blue, tuning the intermolecular Pt···Pt distances finely in the sub-angstrom range in the crystal state is necessary. The introduction of substituent groups on Pt(II) complexes would be an effective way to control the Pt···Pt interactions systematically. In this case, the substituent groups should be placed near the coordination sphere because additional groups often change the crystal packing structures, which may break the Pt···Pt chain structure. In fact, the dynamic behaviors of the assembled Pt(II) complexes derived by the introduction of excessively long alkyl chains would change the emission states between the ^{3}MMLCT and the ligand centered $^3\pi\pi^*$, both in solutions and crystal states. [7, 29–31]

In this work, a series of assembled Pt(II) complex systems using N-heterocyclic carbene (NHC) ligands with different substituent groups, [Pt(CN)$_2$(R-impy)] (R-impyH+ = 1-alkyl-3-(2-pyridyl)-1H-imidazolium, R = Me (**Pt-Me**), Et (**Pt-Et**), ^{i}Pr (**Pt-^{i}Pr**), and ^{t}Bu (**Pt-^{t}Bu**)) (Scheme 1) were constructed. All the complexes exhibited highly efficient photoluminescence (Φ = 0.51–0.81) in the solid state at room temperature. Furthermore, we successfully controlled the emission color over the entire visible region from red to blue by fine tuning the Pt···Pt distances controlled by the substituent groups on the NHC ligands. In particular, it is notable that a blue ^{3}MMLCT emission was realized for **Pt-tBu** for the first time. The wide-range color tuning of luminescence without changing the emission origin (*i.e.*, ^{3}MMLCT emission) is elucidated in detail by structural and spectroscopic analyses.
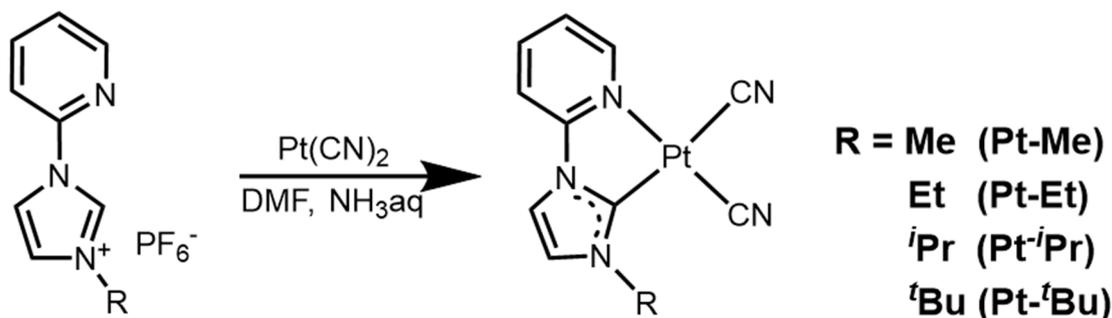
Scheme 1. Synthetic scheme of [Pt(CN)$_2$(R-impy)] [R = Me (**Pt-Me**), Et (**Pt-Et**), ^{i}Pr (**Pt-^{i}Pr**), and ^{t}Bu (**Pt-^{t}Bu**)].

2.2 Experimental detail

2.2.1 Materials.

Potassium tetra(chlorido)platinate(II) (K$_2$[PtCl$_4$]) was purchased from Tanaka Holdings. All other reagents were purchased from Wako Pure Chemical Industries, and all solvents were purchased from Kanto Chemical. Those for synthesis were used without further purification. Platinum(II) dicyanide, Pt(CN)$_2$[32] 1-alkyl-3-(2-pyridyl)-1*H*-imidazolium hexafluorophosphate (R-impyH)PF$_6$ (alkyl = R = methyl (Me), [33] ethyl (Et),[34] isopropyl (^{i}Pr), [35] *tert*-butyl (^{t}Bu) [36]) were synthesized according to literature methods.

Synthesis of [Pt(CN)$_2$(R-impy)] [R = Me (Pt-Me), Et (Pt-Et), ^{i}Pr (Pt-^{i}Pr), ^{t}Bu (Pt-^{t}Bu)]. Pt(CN)$_2$ (207 mg, 0.84 mmol) suspended in an aqueous ammonia (28%, 7 mL) was added dropwise to a refluxing DMF solution of (R-impyH)PF$_6$ (2.10 mmol in 7 mL), and the mixture was refluxed overnight. Then, the reaction mixture was cooled to 0°C, and the precipitated solid was collected by filtration and washed with ice-cooled DMF, Et$_2$O, and acetone.

Pt-Me was obtained as red crystalline powder by recrystallization from DMF/Et$_2$O. Yield, 102 mg (0.25 mmol, 30%). ^{1}H NMR (400 MHz, DMSO-*d$_6$*, TMS, δ) 9.11 (dd, *J* = 5.7, 1.1 Hz, 1H), 8.48 (td, *J* = 8.0, 1.7 Hz, 1H), 8.41 (d, *J* = 2.3 Hz, 1H), 8.24 (d, *J* = 8.2 Hz, 1H), 7.74-7.62 (m, 2H), 4.07 (s, 3H). Anal. calcd for C$_{11}$H$_9$N$_5$Pt·0.2H$_2$O: C, 32.23; H, 2.13; N, 17.09%. Found: C, 32.25; H, 2.04; N, 16.79%. MS (ESI) *m/z*: [M+Na]$^+$ calcd for C$_{11}$H$_9$N$_5$Pt+Na$^+$, 429.04; found, 429.04. mp 345–348 °C (dec).

Pt-Et was obtained as orange powder by recrystallization from hot-DMF/H$_2$O. Yield, 199 mg (0.47 mmol, 50%). ^{1}H NMR (400 MHz, DMSO-*d$_6$*, TMS) δ = 9.11 (dd, *J* = 5.7, 1.1 Hz, 1H), 8.47 (td, *J* = 8.0, 1.8 Hz, 1H), 8.42 (d, *J* = 2.3 Hz, 1H), 8.23 (d, *J* = 8.2 Hz, 1H), 7.78 (d, *J* = 1.8 Hz, 1H), 7.73-7.64 (m, 1H), 4.53 (q, *J* = 7.2 Hz, 2H), 1.43 (t, *J* = 7.1 Hz, 3H). Anal. calcd for C$_{12}$H$_{11}$N$_5$Pt: C, 34.29; H, 2.64; N, 16.66%. Found: C, 34.07; H, 2.42; N, 16.29%. MS (ESI) *m/z*: [M+Na]$^+$ calcd for C$_{12}$H$_{11}$N$_5$Pt+Na$^+$, 443.06; found, 443.06. mp 335–338 °C (dec).

Pt-^{i}Pr was obtained as yellow powder by recrystallization from hot-DMF/H$_2$O. Yield, 182 mg (0.42 mmol, 50%). ^{1}H NMR (400 MHz, DMSO-*d$_6$*, TMS) δ = 9.12 (dd, *J* = 5.5, 1.4 Hz, 1H), 8.56-8.39 (m, 2H), 8.23 (d, *J* = 8.2 Hz, 1H), 7.94 (d, *J* = 2.3 Hz, 1H), 7.69 (t, *J* = 6.2 Hz, 1H), 5.53 (septet, *J* = 6.6 Hz, 1H), 1.49 (d, *J* = 6.9 Hz, 6H). Anal. calcd for C$_{13}$H$_{13}$N$_5$Pt·0.5H$_2$O: C, 35.22; H, 3.16; N, 15.80%. Found: C, 35.07; H, 2.80; N, 15.55%. MS (ESI) *m/z*: [M+Na]$^+$ calcd for C$_{13}$H$_{13}$N$_5$Pt+Na$^+$, 457.07; found: 457.07. mp 338–340 °C (dec).

Pt-^{t}Bu was obtained as pale-yellow powder by recrystallization from hot-DMF/H$_2$O. Yield, 186 mg (0.42 mmol, 50%). ^{1}H NMR (400 MHz, DMSO-*d$_6$*, TMS) δ = 9.21 (dd, *J* = 5.7, 1.1 Hz, 1H), 8.56-8.39 (m, 2H), 8.29 (d, *J* = 8.7 Hz, 1H), 7.85 (d, *J* = 2.3 Hz, 1H), 7.78-7.62 (m, 1H), 1.83 (s, 9H). Anal. calcd

for $C_{14}H_{15}N_5Pt$: C, 37.43; H, 3.25; N, 15.36%. Found: C, 37.46; H, 3.26; N, 15.37%. MS (ESI) m/z: $[M+Na]^+$ calcd for $C_{14}H_{15}N_5Pt+Na^+$, 471.09; found, 471.09. mp 345–350 °C (dec).

2.2.2 Luminescence measurements.

Luminescence spectra were recorded using a JASCO FP-8600 spectrofluorometer at room temperature and 77 K. Slit widths of excitation and emission light were 5 nm. Variable temperature luminescence spectra were measured with a Hamamatsu Photonics multichannel photodetector (PMA-11) and nitrogen laser (Usho KEN-X) for 337 nm excitation. A liquid nitrogen cryostat (Optistat-DN optical Dewer and ITC-503 temperature controller, Oxford instruments) was used for temperature control. Absolute luminescent quantum yields were recorded on a Hamamatsu Photonics C9920-02 absolute photoluminescence quantum yield measurement system equipped with an integrating sphere apparatus and a 150 W CW xenon light source. A Hamamatsu Photonics A10095-3 non-luminescent quartz sample holder was used for absolute photoluminescence quantum yield measurements. The accuracy of the instrument was confirmed by the measurement of the quantum yield of anthracene in ethanol solution ($\Phi = 0.27$). [37] Emission lifetime measurements and time-resolved emission spectra were recorded using a Hamamatsu Photonics C4780 system equipped with streak camera (Hamamatsu Photonics C4334) as a photodetector and a nitrogen laser for the 337 nm excitation. For variable temperature measurements lower than 77 K, a streak camera (Hamamatsu Photonics, C10910-05) system combined with a spectrometer (Hamamatsu Photonics, C11119-04) was used equipped with a closed-cycle refrigerator cryostat (Nagase Techno-Engineering, PS25-SS and Cryogenic Control Systems, Model 22C cryogenic temperature controller). Widely wavelength-tunable pulsed laser (Spectra-Physics InSight X3) with a repetition rate of 80 MHz and a pulse width of < 120 fs was used as the excitation source. Before laser irradiation of the samples, the excitation wavelength and the repetition rate were tuned to 400 nm and 20 kHz using a pulse selector with harmonic generation (Spectra-Physics, UHG), respectively. The excitation powers were 10 and 5 μW for complexes, **Pt-Me** and **Pt-^{t}Bu**, respectively. The emission decays were analyzed using one or two exponentials; $I = A_1\exp(-t/\tau_1) + A_2\exp(-t/\tau_2)$, where A_i denotes the pre-exponential factors for lifetimes τ_i. The average emission lifetimes (τ_{av}) were calculated using following equation (1):

$$\tau_{av} = \frac{\sum A_i \tau_i^2}{\sum A_i \tau_i} \qquad (1)$$

Temperature-dependent emission lifetime data were fitted with Origin2020 software using Boltzmann-type equations.

2.2.3 Single-Crystal X-ray diffraction measurements.

All single-crystal X-ray diffraction measurements were performed using a Rigaku XtaLAB Synergy-S diffractometer equipped with HyPix6000HE hybrid photon counting detector and multilayer mirror-monochromated Cu K$_\alpha$ radiation ($\lambda = 1.54184$ Å) and a micro-focus sealed X-ray tube generator. Each

single crystal was mounted on a MicroMount using paraffin oil. These single crystals were cooled by using N_2-flow type temperature controller. Diffraction data were collected and processed using the CrysAlisPro software. [38] The structures were solved with the intrinsic phasing method by using the SHELXT-2014. [39a] Structural refinements were conducted by the full-matrix least-squares method using the SHELXL-2017. [39b] None-hydrogen atoms were refined anisotropically, and all hydrogen atoms were refined using the riding model. All calculations were performed using Olex2 software.[40]

2.2.4 Other measurements.

^{1}H NMR spectroscopy was performed using a JEOL ECZ-400S NMR spectrometer. Elemental analyses and ESI mass spectrometry were carried out at the analysis center in Hokkaido University. Melting points were measured with a Yanaco MP-500D micro melting point apparatus. UV-vis absorption spectra were measured using a Shimadzu UV-2500PC spectrophotometer. Diffuse reflectance spectra were converted to absorption spectra using the Kubelka-Munk function $F(R^\infty)$. Spectroscopic grade of solvents and a quartz cuvette were used for UV-vis absorption spectra.

2.2.5 Computational methods.

Density functional theory (DFT) and time-dependent density functional theory (TD-DFT) were conducted using the Gaussian 16 program [41] The M06 functional [42] was used for ground-state structure optimizations, vertical excitation energy calculations and optimizations of the lowest singlet and triplet states for the monomer complexes. The SDD basis set and associated effective core potentials were used for Pt [43] and the 6-311+G(d,p) basis sets were used for other atoms. [44] Unless otherwise stated, structure optimizations were performed without any constraints. Vibrational frequency calculations were performed to confirm the nature of the optimized ground-state (DFT) and excited-state (TD-DFT) minima (*i.e.*, no imaginary frequencies).

2.3 Results and discussion

2.3.1 Crystal structure

The crystal structures, three of which included some solvent molecules, **Pt-Me**, **Pt-Et**·CH_3OH, **Pt-^{i}Pr**·$3H_2O$, and **Pt-^{t}Bu**·$3H_2O$, were analyzed by single crystal X-ray diffraction analysis performed at different temperatures (100–250 K) (Tables 2–6). In the temperature regions, all the complexes maintained their crystal structures without phase transition or desolvation. Therefore, the simple abbreviations **Pt-Me**, **Pt-Et**, **Pt-^{i}Pr**, and **Pt-^{t}Bu** are used for the crystal samples hereafter. The molecular and stacking structures at 200 K are shown in Figure 2, and the selected atomic distances and angles are listed in Table 7. The Pt(II) ion in each complex adopts a typical square-planar coordination geometry constructed with two carbon atoms of cyanide anions, one pyridine nitrogen atom, and one carbene carbon atom. All the neutral Pt(II) complexes were stacked one-dimensionally along the *b* axis (Figure 2). However, the stacking modes are slightly different: **Pt-Me** has a completely parallel stack (Figure 1, A) because the crystallographic non-hydrogen atoms are located on the crystallographic mirror planes of the space group $P2_1/m$, while the other three complexes have slightly inclined stacks with the dihedral angles between the (0,1,0) plane (*i.e.*, perpendicular to the b axis) being 6.3°, 6.4°, and 5.5° for **Pt-Et**, **Pt-iPr**, and **Pt-tBu**, respectively. As a result, two different Pt···Pt distances were observed in the stacks (Figure 1, type C) for these three complexes, and the difference depends on the shift from the stacking axis of the Pt atoms. The average Pt···Pt distances increased in the order of **Pt-Me** (3.28 Å), **Pt-Et** (3.35 Å), **Pt-iPr** (3.40 Å), and **Pt-tBu** (3.57 Å) (Table 7). These Pt···Pt distances are shorter or comparable to twice the van der Waals radius of platinum (3.5 Å),[45] which indicates that the electronic interactions are effective in these one-dimensional stacking chains. It is worth noting that the Pt···Pt···Pt angles also decreased from 180° in the order of **Pt-Me** (170.38(5)°), **Pt-Et** (161.43(1)°), **Pt-iPr** (157.15(1)°), and **Pt-tBu** (147.68(1)°), as shown in Table 7, which could be related to the strength of the Pt···Pt interactions. The packing structures of the four crystals are shown in Figures 3–6. It can be seen that the solvent molecules would affect the stacking structures of the Pt(II) complexes through hydrogen bonding. However, we discuss the stacking structures and Pt···Pt interactions obtained from the overall crystal packing here because neither phase transition nor desolvation was observed during the measurements.
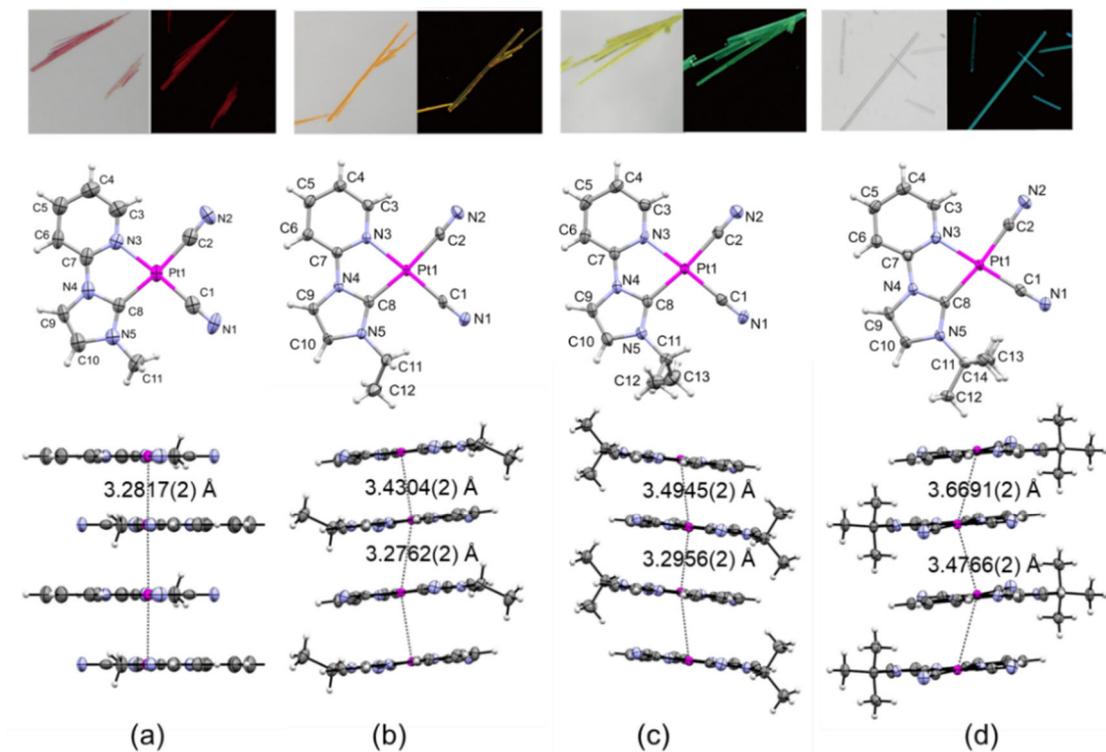
Figure 2. Photographs of crystals (top) and ORTEP drawings of molecular (middle) stacking structures along the *b* axis (bottom) of the Pt(II) complexes at 200 K: (a) **Pt-Me**, (b) **Pt-Et**, (c) **Pt-^{i}Pr**, and (d) **Pt-^{t}Bu**. The thermal ellipsoids are displayed at the 50% probability level for non-hydrogen atoms. Solvent molecules are omitted for clarity.

Pt-Me
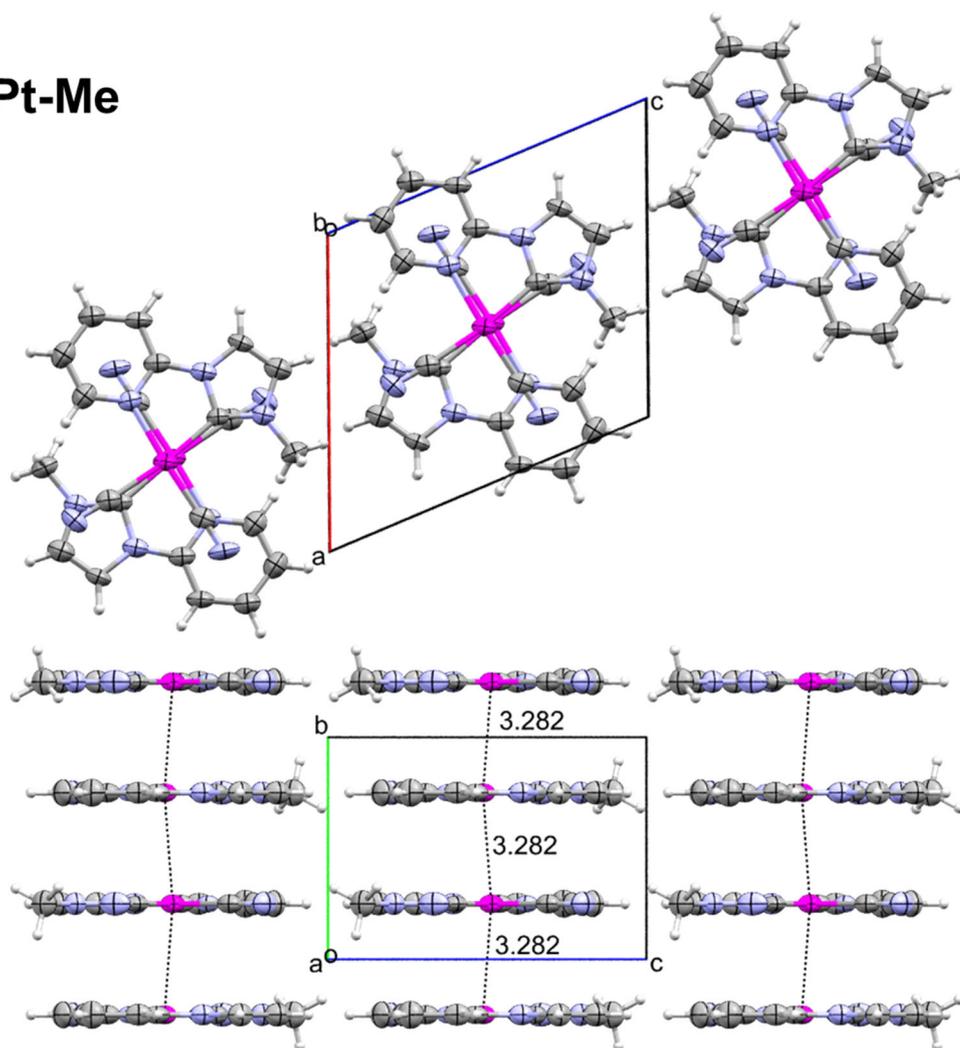
Figure 3. Packing structures of **Pt-Me** at 200 K.

Pt-Et
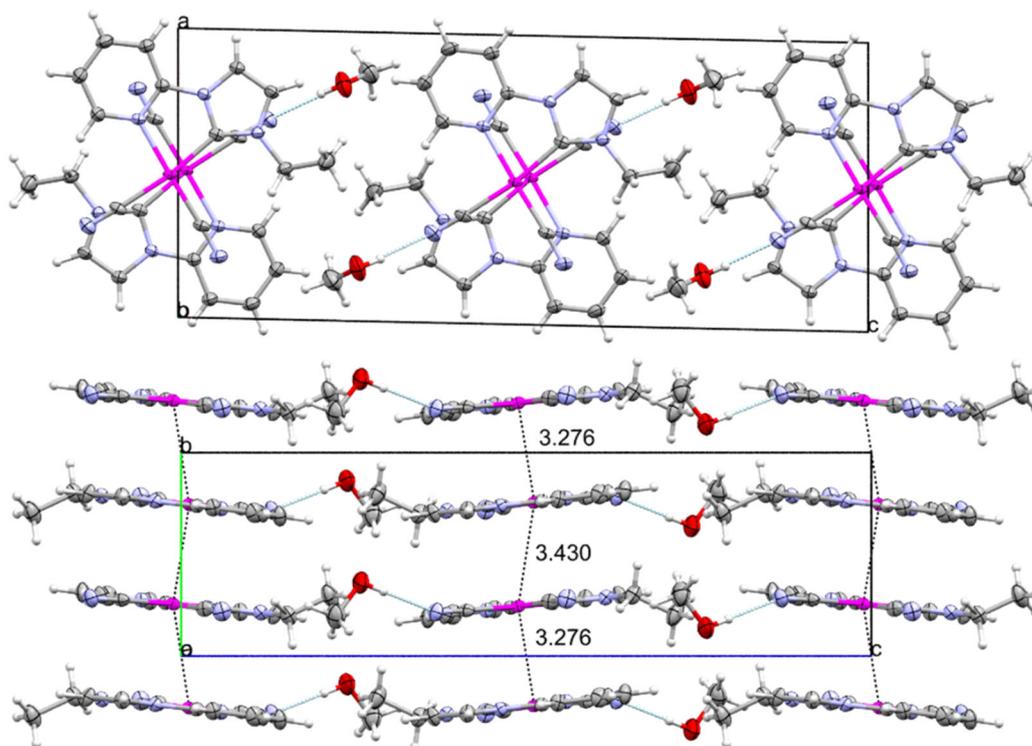
Figure 4. Packing structures of **Pt-Et**·CH$_3$OH at 200 K.
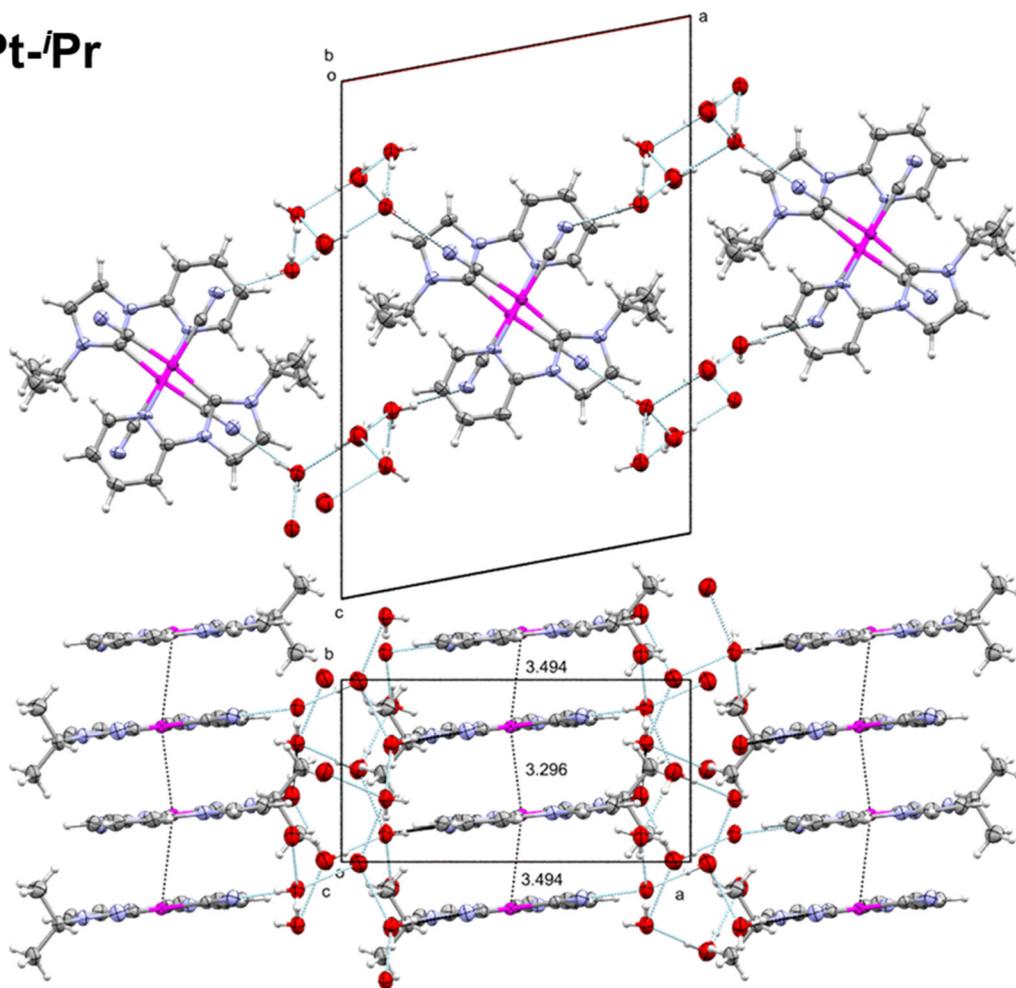
Figure 5. Packing structures of **Pt-^{i}Pr**·3H$_2$O at 200 K.

Pt-tBu
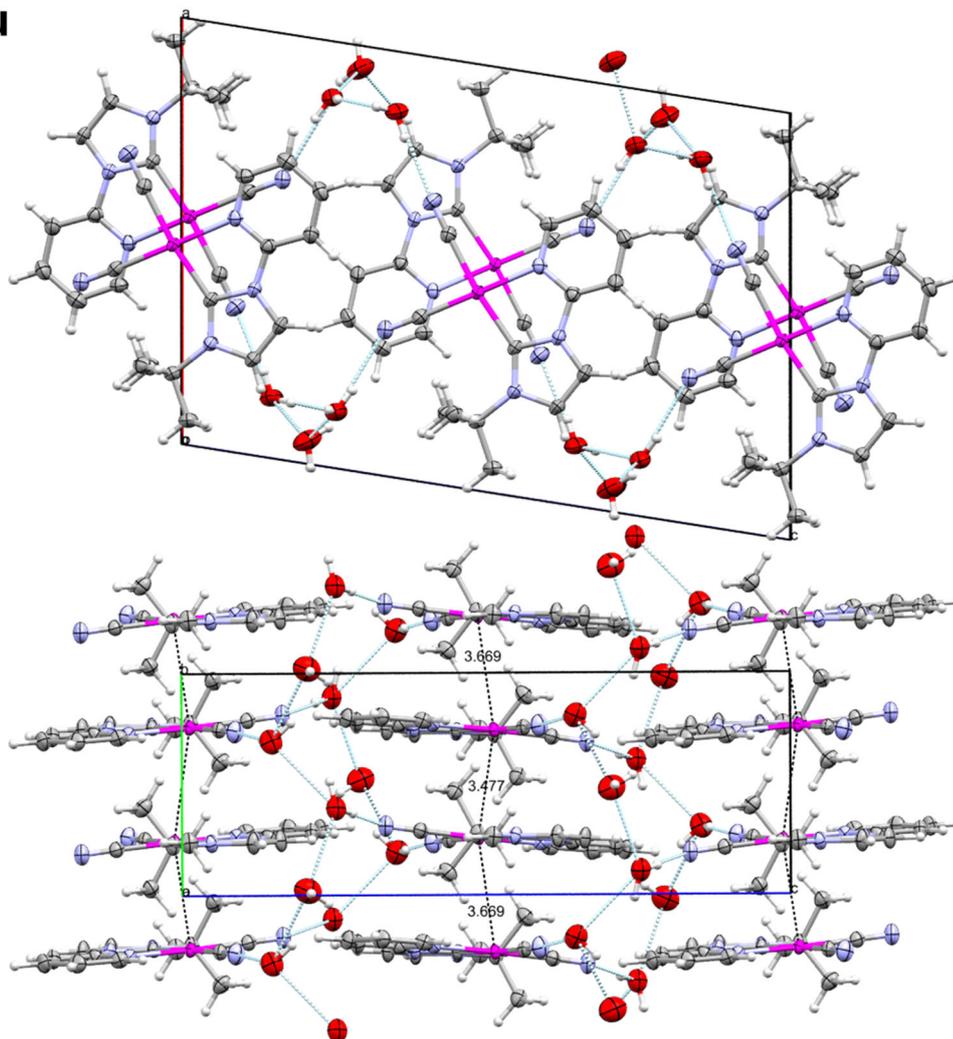
Figure 6. Packing structures of **Pt-tBu**·3H₂O at 200 K.

Table 2. Crystal data for complexes at 200 K.

	Pt-Me	**Pt-Et**	**Pt-^{i}Pr**	**Pt-^{t}Bu**
Formula	$C_{11}H_9N_5Pt$	$C_{13}H_{15}N_5OPt$	$C_{13}H_{19}N_5O_3Pt$	$C_{16}H_{25}N_5O_3Pt$
Formula weight	406.32	452.39	488.42	502.45
Crystal system	monoclinic	monoclinic	monoclinic	monoclinic
Space group	$P2_1/m$	$P2_1/c$	$P2_1/c$	$P2_1/c$
a / Å	9.3398(4)	9.40710(10)	12.9439(2)	13.1903(2)
b / Å	6.5403(3)	6.61870(10)	6.65570(10)	6.86340(10)
c / Å	10.0913(4)	22.3212(2)	18.9102(3)	18.9764(2)
α / °	90	90	90	90
β / °	112.700(4)	91.2330(10)	100.6950(10)	98.9960(10)
γ / °	90	90	90	90
V / Å^3	568.68(4)	1389.46(3)	1600.83(4)	1696.81(4)
T / K	200	200	200	200
Z	2	4	4	4
D_{calc} / g cm^{-3}	2.373	2.163	2.027	1.967
$F(000)$	376	856	936	968
Reflections collected	4324	13661	10352	16732
Unique reflections	1236	2878	3255	3449
GOF on F^2	1.107	1.269	1.121	1.092
R_{int}	0.0304	0.0257	0.0295	0.0311
$R_1{}^a$	0.0436	0.0299	0.0308	0.0237
w$R_2{}^b$ (all data)	0.0984	0.0901	0.0960	0.0635

$^a R_1 = \Sigma||F_o| - |F_c||/\Sigma|F_o|$. ^{b} $wR_2 = [\Sigma w(F_o^2 - F_c^2)/ \Sigma w(F_o)^2]^{1/2}$, $w = [\Sigma_c^2(F_o^2) + (xP)^2 + yP]^{-1}$, $P = (F_o^2 - 2F_c^2)/3$.

Table 3. Crystal data for **Pt-Me** at various temperatures during 100–250 K.

T / K	100	130	160	190	220	250
Formula	$C_{11}H_9N_5Pt$	$C_{11}H_9N_5Pt$	$C_{11}H_9N_5Pt$	$C_{11}H_9N_5Pt$	$C_{11}H_9N_5Pt$	$C_{11}H_9N_5Pt$
Formula weight	406.32	406.32	406.32	406.32	406.32	406.32
Crystal system	monoclinic	monoclinic	monoclinic	monoclinic	monoclinic	monoclinic
Space group	$P2_1/m$	$P2_1/m$	$P2_1/m$	$P2_1/m$	$P2_1/m$	$P2_1/m$
a / Å	9.3296(5)	9.3328(4)	9.3391(5)	9.3452(4)	9.3458(5)	9.3483(7)
b / Å	6.4863(3)	6.4985(3)	6.5167(3)	6.5327(3)	6.5493(3)	6.5644(4)
c / Å	10.0810(5)	10.0863(4)	10.0850(5)	10.0927(4)	10.0914(5)	10.0907(7)
α / °	90	90	90	90	90	90
β / °	112.766(5)	112.714(4)	112.710(5)	112.709(5)	112.678(6)	112.649(8)
γ / °	90	90	90	90	90	90
V / Å^3	562.52(2)	564.28(4)	566.19(5)	568.39(5)	569.92(5)	571.47(7)
Z	2	2	2	2	2	2
D_{calc} /g cm^{-3}	2.399	2.391	2.383	2.374	2.368	2.361
$F(000)$	376.0	376.0	376.0	376.0	376.0	376.0
Reflections collected	8675	5700	3253	3426	5619	4905
Unique reflections	1266	1226	1231	1236	1238	1251
GOF on F^2	1.106	1.113	1.077	1.094	1.134	1.068
R_{int}	0.0680	0.0550	0.0325	0.0288	0.0321	0.0327
R_1 [a]	0.0498	0.0516	0.0488	0.0496	0.0447	0.0507
wR_2 [b] (all data)	0.1257	0.1253	0.1299	0.1296	0.1025	0.1244

[a] $R_1 = \Sigma ||F_o|-|F_c|| /\Sigma|F_o|$. [b] $wR_2 = [\Sigma w(F_o^2 - F_c^2)/ \Sigma w(F_o)^2]^{1/2}$, $w = [\sigma_c^2(F_o^2) + (xP)^2 + yP]^{-1}$, $P = (F_o^2 - 2F_c^2)/3$.

Table 4. Crystal data for **Pt-Et** at various temperatures during 100–250 K.

T / K	100	130	160	190	220	250
Formula	$C_{13}H_{15}N_5OPt$	$C_{13}H_{15}N_5OPt$	$C_{13}H_{15}N_5OPt$	$C_{13}H_{15}N_5OPt$	$C_{13}H_{15}N_5OPt$	$C_{13}H_{15}N_5OPt$
Formula weight	452.39	452.39	452.39	452.39	452.39	452.39
Crystal system	monoclinic	monoclinic	monoclinic	monoclinic	monoclinic	monoclinic
Space group	$P2_1/c$	$P2_1/c$	$P2_1/c$	$P2_1/c$	$P2_1/c$	$P2_1/c$
a / Å	9.3871(1)	9.3932(1)	9.3991(1)	9.4058(1)	9.4104(1)	9.4168(1)
b / Å	6.5510(1)	6.5690(1)	6.5885(1)	6.6113(1)	6.6357(1)	6.6622(1)
c / Å	22.2560(2)	22.2715(2)	22.2909(2)	22.3157(2)	22.3339(2)	22.3575(2)
α / °	90	90	90	90	90	90
β / °	90.992(1)	91.052(1)	91.128(1)	91.208(1)	91.301(1)	91.399(1)
γ / °	90	90	90	90	90	90
V / Å^3	1368.43(3)	1374.01(3)	1380.12(3)	1387.38(3)	13564	13526
Z	4	4	4	4	4	4
D_{calc} /g cm^{-3}	2.196	2.187	2.177	2.166	2.155	2.143
$F(000)$	856.0	856.0	856.0	856.0	856.0	856.0
Reflections collected	13142	13350	13381	13730	13564	13526
Unique reflections	2442	2814	2826	2873	2863	2875
GOF on F^2	1.188	1.252	1.248	1.244	1.178	1.208
R_{int}	0.0365	0.0281	0.0276	0.0273	0.0263	0.0287
R_1[a]	0.0251	0.0264	0.0284	000288	0.0283	0.0281
wR_2[b] (all data)	0.0688	0.0785	0.0841	0.0868	0.0885	0.0817

[a] $R_1 = \Sigma||F_o|-|F_c|| /\Sigma|F_o|$. [b] $wR_2 = [\Sigma w(F_o^2 - F_c^2)/ \Sigma w(F_o)^2]^{1/2}$, $w = [\sigma_c^2(F_o^2) + (xP)^2 + yP]^{-1}$, $P = (F_o^2 - 2F_c^2)/3$.

Table 5. Crystal data for **Pt-^{i}Pr** at various temperatures during 100–250 K.

T / K	100	130	160	190	220	250
Formula	$C_{13}H_{19}N_5O_3Pt$	$C_{13}H_{19}N_5O_3Pt$	$C_{13}H_{19}N_5O_3Pt$	$C_{13}H_{19}N_5O_3Pt$	$C_{13}H_{19}N_5O_3Pt$	$C_{13}H_{19}N_5O_3Pt$
Formula weight	488.42	488.42	488.42	488.42	488.42	488.42
Crystal system	monoclinic	monoclinic	monoclinic	monoclinic	monoclinic	monoclinic
Space group	$P2_1/c$	$P2_1/c$	$P2_1/c$	$P2_1/c$	$P2_1/c$	$P2_1/c$
a / Å	12.8866(3)	12.8991(3)	12.9153(2)	12.9356(2)	12.9573(1)	12.9811(2)
b / Å	6.6082(2)	6.6210(1)	6.6368(1)	6.6507(1)	6.6682(1)	6.6860(1)
c / Å	18.8713(4)	18.8872(3)	18.8989(3)	18.9072(2)	18.9168(2)	18.9266(3)
α / °	90	90	90	90	90	90
β / °	100.642(2)	100.647(2)	100.679(2)	100.6900(10)	100.6890(10)	100.678(2)
γ / °	90	90	90	90	90	90
V / Å^3	1579.39(7)	1585.29(5)	1591.89(4)	1598.37(4)	1606.09(3)	1614.23(4)
Z	4	4	4	4	4	4
D_{calc} / g cm^{-3}	2.054	2.046	2.038	2.030	2.020	2.010
$F(000)$	936.0	936.0	936.0	936.0	936.0	936.0
Reflections collected	10146	9758	10837	10816	10278	10192
Unique reflections	3201	3216	3229	3290	3298	3256
GOF on F^2	1.108	1.156	1.100	1.112	1.075	1.100
R_{int}	0.0286	0.0272	0.0304	0.0255	0.0310	0.0363
R_1[a]	0.0381	0.0308	0.0305	0.0262	0.0287	0.0382
wR_2[b] (all data)	0.1159	0.0981	0.0931	0.0772	0.0894	0.1146

[a] $R_1 = \Sigma||F_o|-|F_c||\,/\Sigma|F_o|$. [b] $wR_2 = [\Sigma w(F_o^2 - F_c^2)/\,\Sigma w(F_o)^2]^{1/2}$, $w = [\sigma_c^2(F_o^2) + (xP)^2 + yP]^{-1}$, $P = (F_o^2 - 2F_c^2)/3$.

Table 6. Crystal data for **Pt-^{t}Bu** at various temperatures during 100–250 K.

T / K	100	130	160	190	220	250
Formula	$C_{16}H_{25}N_5O_3Pt$	$C_{16}H_{25}N_5O_3Pt$	$C_{16}H_{25}N_5O_3Pt$	$C_{16}H_{25}N_5O_3Pt$	$C_{16}H_{25}N_5O_3Pt$	$C_{16}H_{25}N_5O_3Pt$
Formula weight	502.45	502.45	502.45	502.45	502.45	502.45
Crystal system	monoclinic	monoclinic	monoclinic	monoclinic	monoclinic	monoclinic
Space group	$P2_1/c$	$P2_1/c$	$P2_1/c$	$P2_1/c$	$P2_1/c$	$P2_1/c$
a / Å	13.1174(2)	13.1269(2)	13.1391(2)	13.1816(2)	13.2029(2)	13.2252(2)
b / Å	6.8158(1)	6.8318(1)	6.8481(1)	6.8578(1)	6.8759(1)	6.8943(1)
c / Å	18.9496(2)	18.9590(3)	18.9716(3)	18.9696(2)	18.9862(2)	18.9992(3)
α / °	90	90	90	90	90	90
β / °	98.967(1)	98.930(1)	98.893(1)	98.991(1)	98.982(1)	98.984(1)
γ / °	90	90	90	90	90	90
V / Å^3	1673.49(4)	1679.64(4)	1686.50(4)	1693.72(4)	1702.47(4)	1711.07(5)
Z	4	4	4	4	4	4
D_{calc} / g cm^{-3}	1.994	1.987	1.979	1.970	1.960	1.950
$F(000)$	968.0	968.0	968.0	968.0	968.0	968.0
Reflections collected	16747	16917	16527	16972	16715	16958
Unique reflections	3435	3469	3454	3514	3458	3514
GOF on F^2	1.123	1.104	1.093	1.110	1.073	1.113
R_{int}	0.0314	0.0338	0.0359	0.0250	0.0307	0.0318
R_1[a]	0.0238	0.0255	0.0250	0.0230	0.0249	0.0255
wR_2[b] (all data)	0.0616	0.0693	0.0685	0.0650	0.0680	0.0718

[a] $R_1 = \Sigma||F_o|-|F_c|| /\Sigma|F_o|$. [b] $wR_2 = [\Sigma w(F_o^2 - F_c^2)/ \Sigma w(F_o)^2]^{1/2}$, $w = [\sigma_c^2(F_o^2) + (xP)^2 + yP]^{-1}$, $P = (F_o^2 - 2F_c^2)/3$.

Table 7. Selected interatomic distances (Å) and angles (°) for **Pt-Me**, **Pt-Et**, **Pt-*i*Pr**, and **Pt-*t*Bu**, at 200 K.

	Pt-Me	**Pt-Et**	**Pt-*i*Pr**	**Pt-*t*Bu**
Pt1−C1	1.96(1)	1.955(6)	1.961(6)	1.945(4)
Pt1−C2	2.01(1)	2.009(6)	2.005(5)	2.011(4)
Pt1−N3	2.08(1)	2.089(5)	2.081(5)	2.078(3)
Pt1−C8	2.01(1)	2.001(6)	2.015(5)	2.057(4)
N1−C1	1.16(2)	1.146(8)	1.139(8)	1.152(5)
N2−C2	1.15(2)	1.137(8)	1.144(7)	1.130(6)
Pt1⋯Pt1'	3.2817(2)	3.2762(2)	3.2956(2)	3.4766(2)
Pt1⋯Pt1"	–	3.4304(2)	3.4945(2)	3.6691(2)
C1−Pt1−C2	89.0(6)	88.8(2)	88.0(2)	86.4(2)
C1−Pt1−C8	97.6(5)	98.9(2)	98.6(2)	101.1(2)
C1−Pt1−N3	176.8(5)	177.7(2)	177.4(2)	178.5(1)
C2−Pt1−C8	173.4(5)	172.2(2)	173.3(2)	172.6(1)
C2−Pt1−N3	94.2(5)	93.3(2)	94.5(2)	93.3(2)
C8−Pt1−N3	79.2(4)	79.0(2)	78.9(2)	79.4(1)
Pt1'⋯Pt1⋯Pt1"	170.38(5)	161.43(1)	157.15(1)	147.68(1)

2.3.2 Photophysical properties

Table 1 summarizes the photophysical data of the **Pt-Me**, **Pt-Et**, **Pt-^{i}Pr**, and **Pt-^{t}Bu** complexes in the solid state at 298 K and 77 K. As mentioned in the previous section, these complexes exhibited intense luminescence with different colors ranging from red, orange, and yellowish green to blue, respectively, in the solid state. All the complexes showed very high emission quantum yields (Φ) of 0.51–0.81 with sub-microsecond emission lifetimes (τ) (0.29–0.88 μs) at 298 K. The emission spectra displayed structureless broad emission bands with the maxima of 612 (**Pt-Me**), 592 (**Pt-Et**), 537 (**Pt-^{i}Pr**), and 484 nm (**Pt-^{t}Bu**) (Figure 7b). The emission color coordinates are shown in the CIE 1931 chromaticity diagram in Figure 8. Consistent with the emission spectra, the excitation spectra appeared at different wavelengths, shifting to shorter wavelengths from **Pt-Me** to **Pt-^{t}Bu** (Figure 7a). The non-structured spectral profiles as well as other photophysical features including the values of radiative rate constants (k_r) (10^5–10^6 s^{-1}, Table 8) suggest that the remarkable emissions in the solid state originated from the ^{3}MMLCT state and were controlled by the packing structures.

Table 8. Photophysical data of [Pt(CN)$_2$(R-impy)] in the solid state [R = Me (**Pt-Me**), Et (**Pt-Et**), ^{i}Pr (**Pt-^{i}Pr**), and ^{t}Bu (**Pt-^{t}Bu**)].

Complex	T / K	λ_{max}[a] / nm	Φ[b]	τ[c] / μs (A[d])	τ_{av}[e] / μs	k_r[f] / s^{-1}	k_{nr}[g] / s^{-1}
Pt-Me	298	612	0.51	0.24 (0.93), 0.58 (0.07)	0.29	1.8×10^6	1.7×10^6
	77	691	0.58	0.52 (0.53), 1.50 (0.47)	1.2	4.8×10^5	3.5×10^5
Pt-Et	298	592	0.81	0.22 (0.45), 0.50 (0.55)	0.43	1.9×10^6	4.4×10^5
	77	656	0.77	0.90 (0.40), 1.44 (0.60)	1.3	5.9×10^5	1.8×10^5
Pt-^{i}Pr	298	537	0.72	0.26 (0.93), 0.67 (0.07)	0.33	2.2×10^6	8.5×10^5
	77	555	0.88	0.31 (0.33), 1.01 (0.67)	0.92	9.6×10^5	1.3×10^5
Pt-^{t}Bu	298	484	0.70	0.55 (0.72), 1.25 (0.28)	0.88	8.0×10^5	3.4×10^5
	77	472	0.75	1.26 (0.96), 2.86 (0.04)	1.4	5.4×10^5	1.8×10^5

[a] Emission maximum. [b] Photoluminescence quantum yields. [c] Emission lifetime. [d] Pre-exponential factors. [e] Average emission lifetimes were determined from the equation $\tau_{av} = \Sigma\, A_i\tau_i^2 / \Sigma\, A_i\tau_i$ (i = 1, 2). The emission decay curves are shown in Figure 9. [f] Radiative rate constants (k_r) were estimated from the equation $k_r = \Phi/\tau_{av}$. [g] Non-radiative rate constants (k_{nr}) were estimated from the equation $k_{nr} = k_r(1 - \Phi)/\Phi$.

In contrast to the emission in the solid state, all the complexes exhibited almost the same absorption and emission spectra in diluted solutions (Figures 7c and 7d), which indicate that the electronic effects of the substituent groups of the NHC ligands on the monomer complexes are negligible. As shown in Figure 3c, these four complexes exhibited moderately intense absorption bands ($\varepsilon \sim 5 \times 10^3$ M^{-1} cm^{-1}) in the region of 280–360 nm, which are absent in the absorption spectra of the free ligands; thus, the bands are considered to originate from ^{1}MLCT transition. Time-dependent density functional theory (TD-DFT) calculations support the assignment although metal-perturbed $^1\pi\pi^*$ (or ^{1}LC) transitions are

also included to some extent (Figures 10–13, Tables 10–22). Meanwhile, the emission spectra with vibronic structures, which were observed only for a rigid glass at 77 K, could be attributed to the emission from the ligand-centered $^3\pi\pi^*$ (or ^{3}LC) excited state (Figure 7d, Table 9). This indicates that the lowest excited triplet state is not the ^{3}MLCT state, but the $^3\pi\pi^*$ state for the monomer complexes and they have essentially the same emission states, as confirmed by theoretical calculations (Figures 15 and 16).
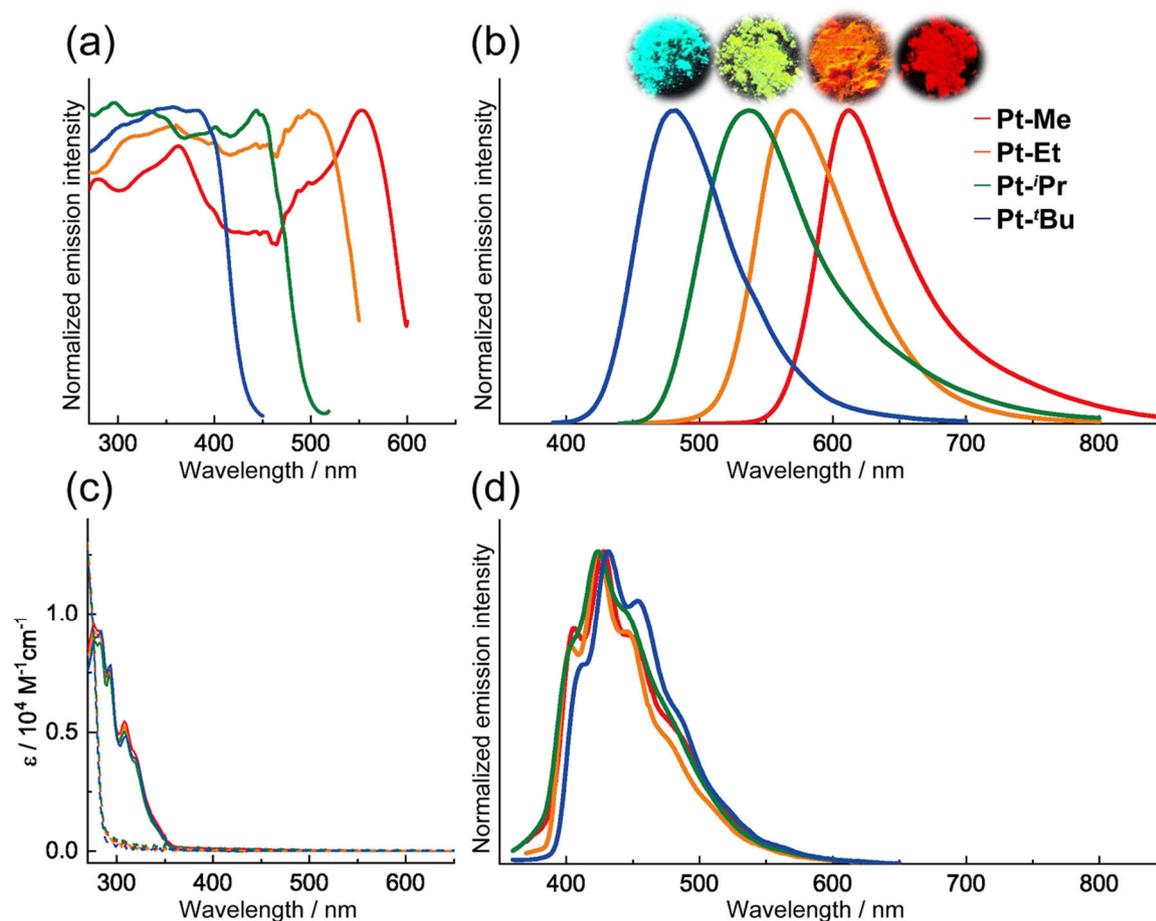
Figure 7. (a) Excitation and (b) emission spectra of **Pt-Me** (red), **Pt-Et** (orange), **Pt-^{i}Pr** (green), and **Pt-^{t}Bu** (blue) in the solid state at room temperature with photos of crystalline powders under UV light. The excitation wavelengths were 350 nm for all complexes, while the excitation spectra were measured at each emission maximum. (c) UV-vis absorption spectra of the four complexes in DMF (1×10^{-4} M) at 298 K. Dotted lines indicate the absorption spectra of corresponding protonated ligands, R-impyH$^+$ (R = Me, Et, ^{i}Pr, and ^{t}Bu). (d) Emission spectra of the four complexes in EtOH-MeOH (1:1 v/v, 1.0×10^{-7} M) at 77 K (λ_{ex} = 280 nm). The color assignment is the same as that in (b).
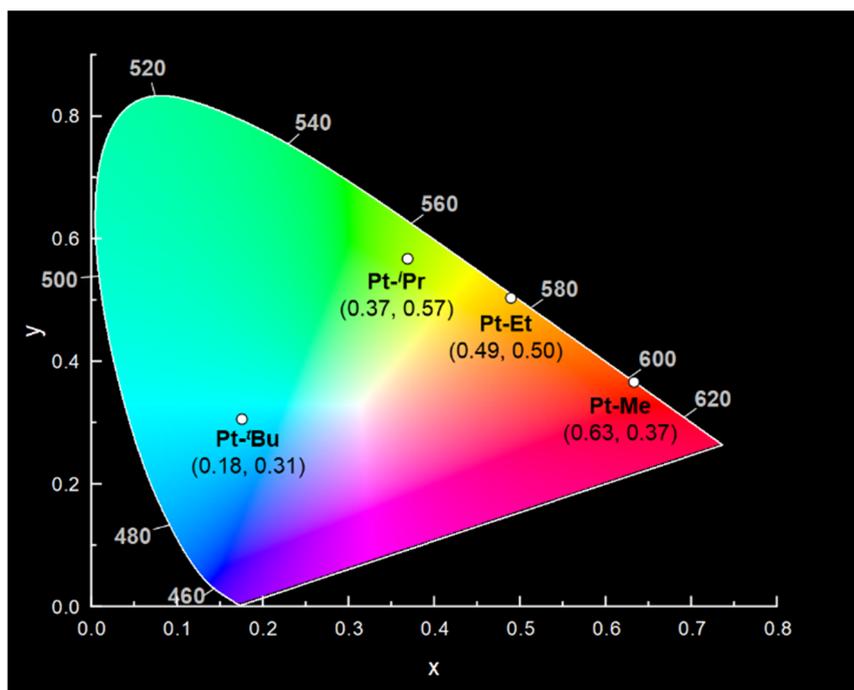
Figure 8. CIE1931 diagrams of **Pt-Me, Pt-Et, Pt-^{i}Pr** and **Pt-^{t}Bu** in the solid states at 298 K.
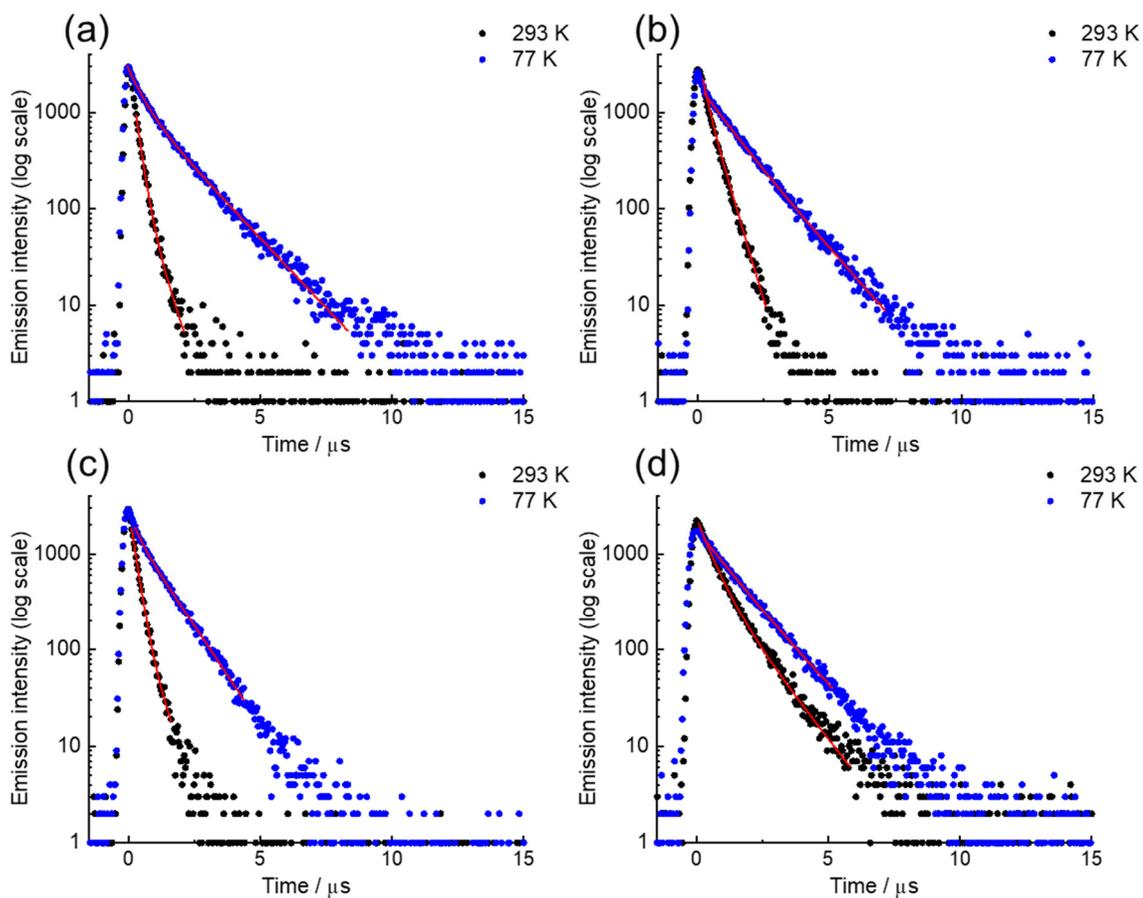
Figure 9. Emission decay curves and fitting curve (red line) of (a) **Pt-Me**, (b) **Pt-Et**, (c) **Pt-^{i}Pr**, and (d) **Pt-^{t}Bu** at 293 K (black) and 77 K (blue) (λ_{ex} = 337 nm).
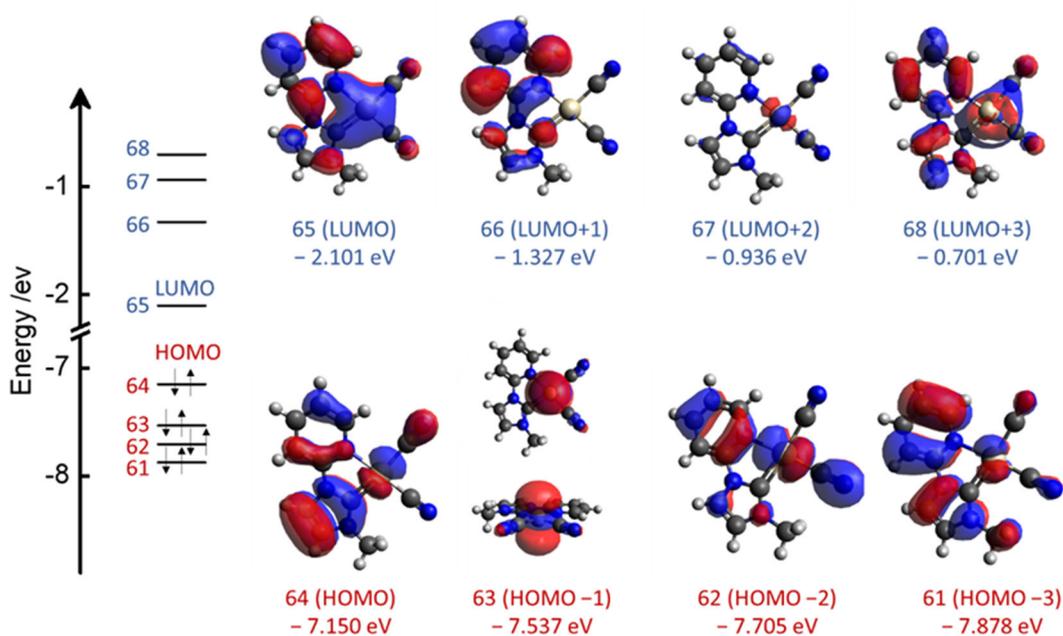
Figure 10. Kohn–Sham orbitals in the frontier region for the singlet ground state of **Pt-Me** (isovalue = 0.02) with their energies (eV). The highest occupied molecular orbital (HOMO) are delocalized on both Pt and the ligands. On the other hand, the lowest unoccupied molecular orbitals (LUMOs) are delocalized on Pt and the NHC ligand. Therefore, the lowest allowed transitions can be assigned to a mixed [1]MLCT and [1]LC state.
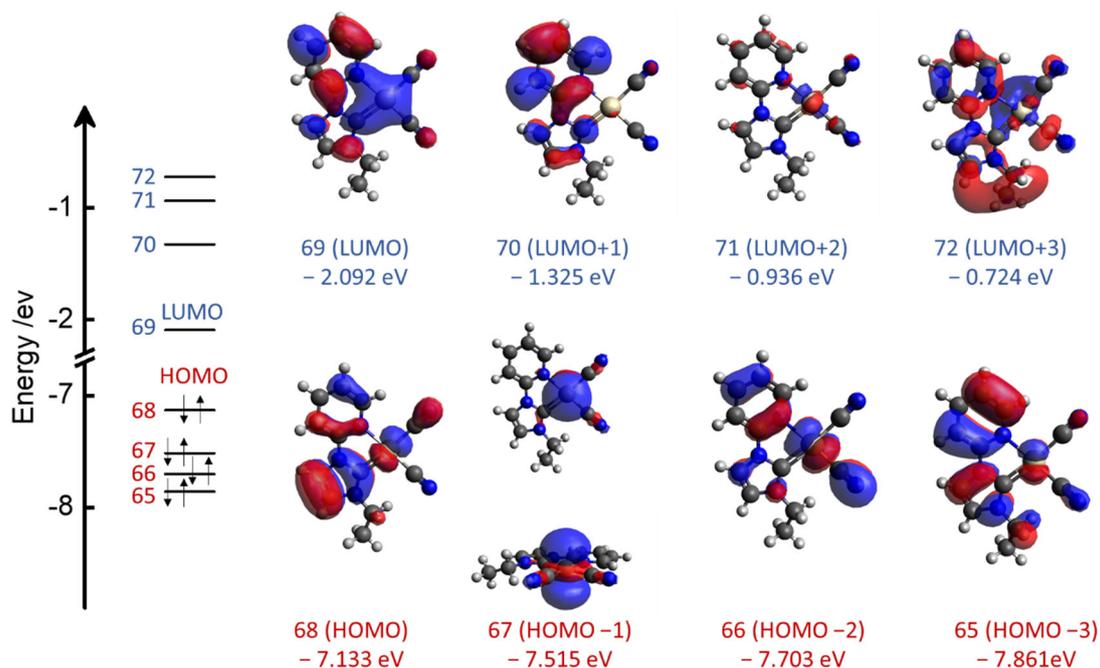
Figure 11. Kohn–Sham orbitals in the frontier region for the singlet ground state of **Pt-Et** (isovalue = 0.02) with their energies (eV). The HOMO and LUMO characters are similar to those of **Pt-Me**.
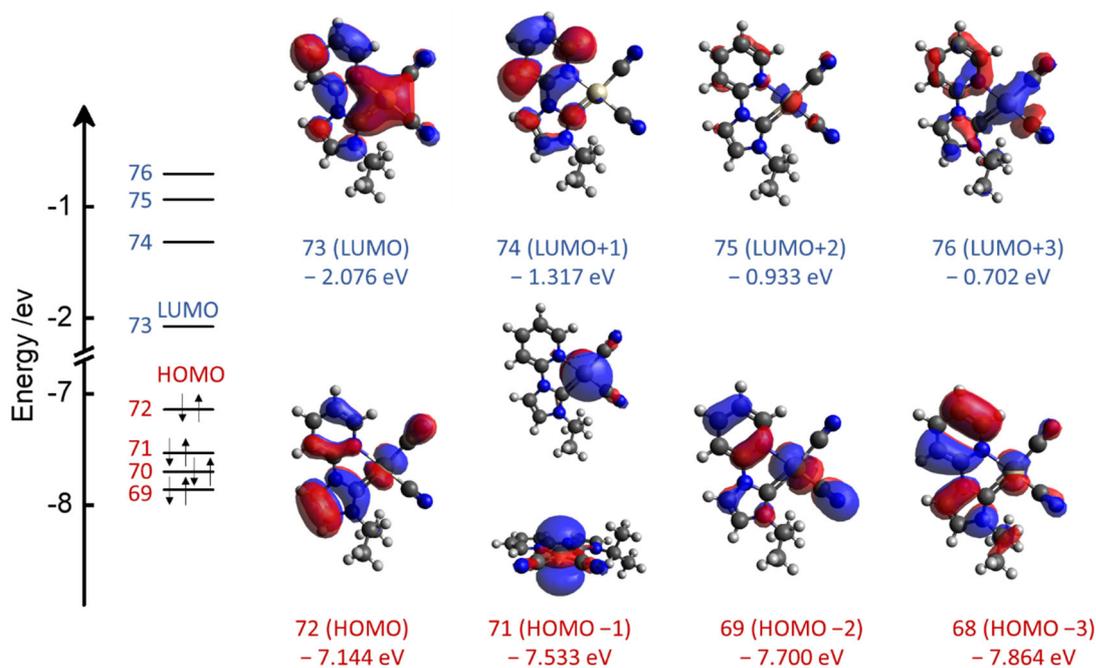
Figure 12. Kohn–Sham orbitals in the frontier region for the singlet ground state of **Pt-^{i}Pr** (isovalue = 0.02) with their energies (eV). The HOMO and LUMO characters are similar to those of **Pt-Me**.
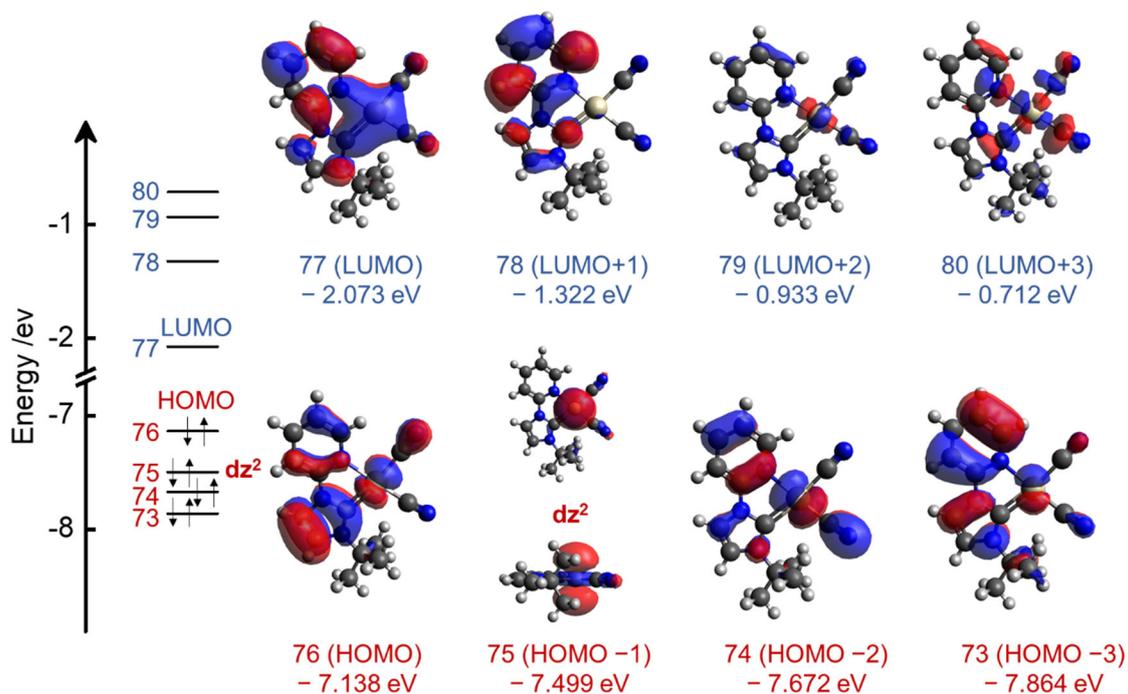
Figure 13. Kohn–Sham orbitals in the frontier region for the singlet ground state of **Pt-^{t}Bu** (isovalue = 0.02) with their energies (eV). The HOMO and LUMO characters are similar to those of **Pt-Me**.
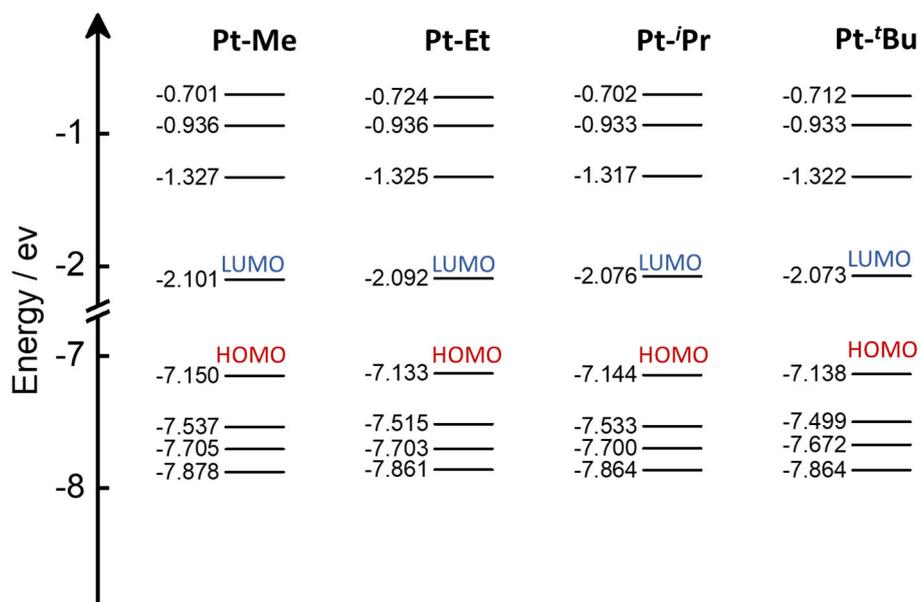
Figure 14. Energy level diagrams for **Pt-Me**, **Pt-Et**, **Pt-*i*Pr**, and **Pt-*t*Bu** of the singlet ground states. The energy levels of all four complexes in the frontier region are almost the same.
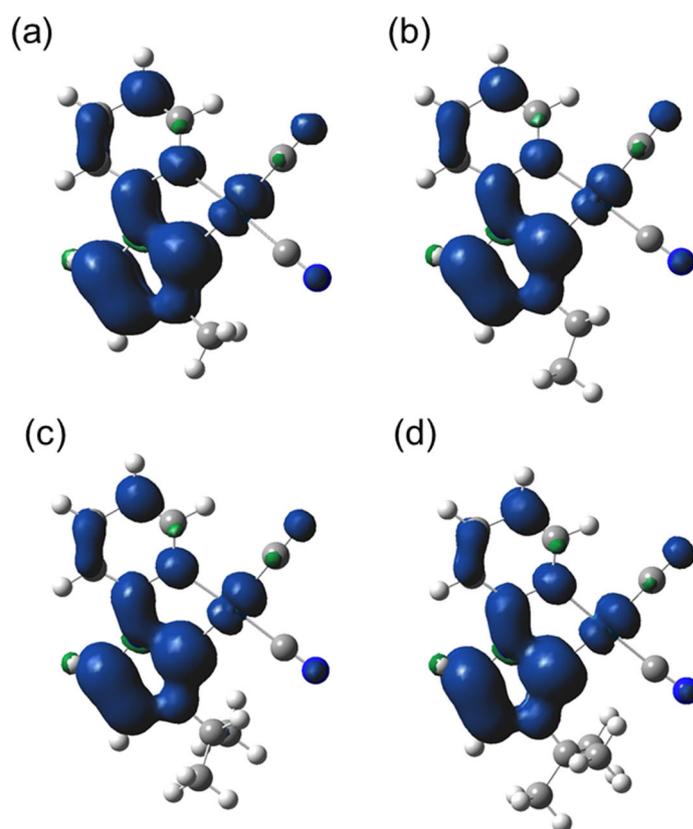
Figure 15. Spin density plots for **Pt-Me** (a), **Pt-Et** (b), **Pt-^{i}Pr** (c), and **Pt-^{t}Bu** (d) for triplet states (calculated the spin density distributions of the T_1 structures using UM06 single-point energy calculations). For all the complexes, the spin density was mainly delocalized in the NHC ligand (the calculated spin density on Pt is 0.18 for **Pt-Me**, 0.17 for **Pt-Et**, 0.17 for **Pt-^{i}Pr** and 0.14 for **Pt-^{t}Bu**), implying the ^{3}LC state mixed to some extent with the ^{3}MLCT state.
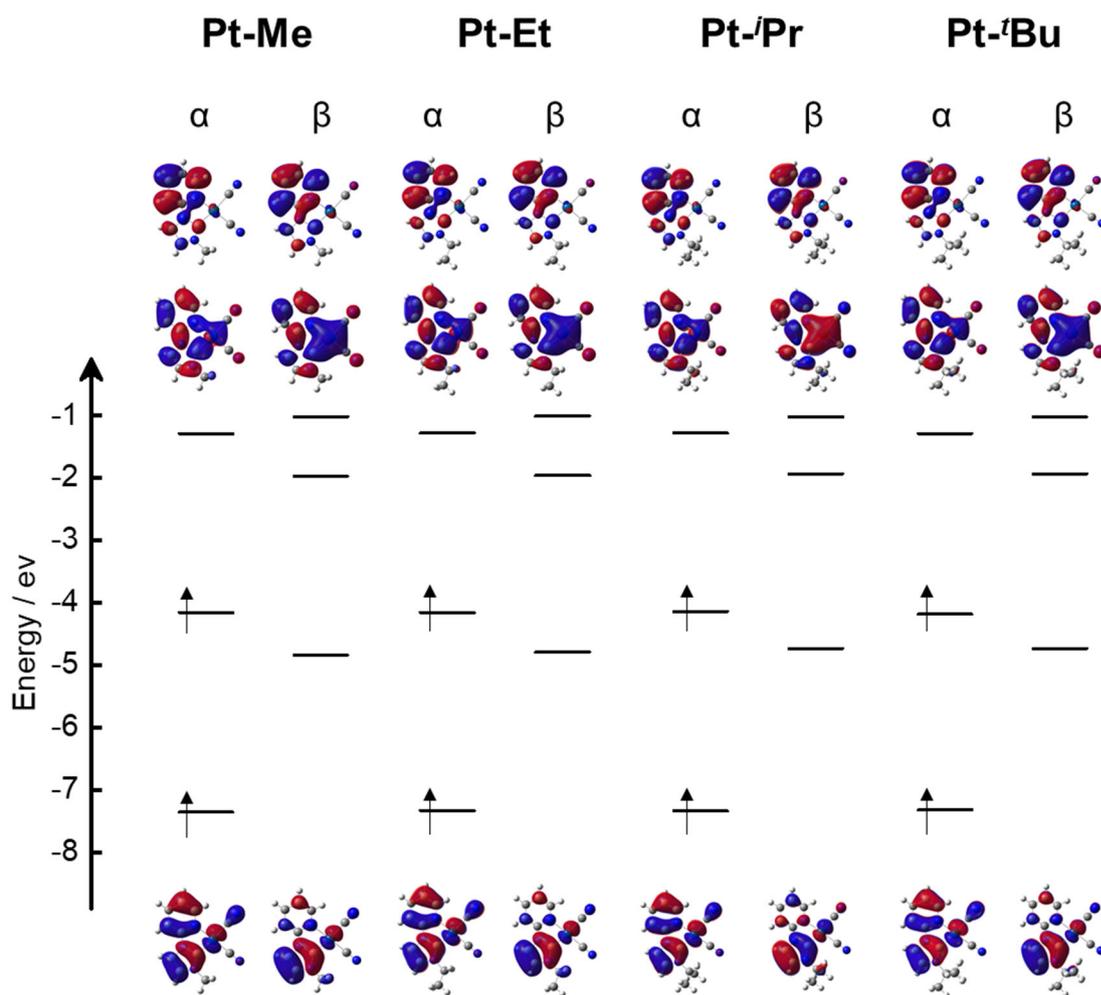
Figure 16. Kohn–Sham orbitals in the frontier region of the T_1 structure, obtained by UM06 single-point calculations starting from the TD-DFT-optimized triplet state structures. There is no significant difference in the energy levels of singly occupied molecular orbitals (SOMOs) for all complexes. The electronic effects of the substituent groups of the NHC ligands on the monomer states in both of ground state and excited states were negligible. It was strongly suggested that the remarkable emission from red to blue in the solid state originated from the ^{3}MMLCT state and could be achieved by finely controlling of the intermolecular Pt···Pt distances.

Considering the large differences in the luminescence properties in the solid and solution states, we conclude that all the solid-state luminescence originated from ^{3}MMLCT. Moreover, DFT calculations of the stacked tetramers based on the crystal structures supported the emergence of lower energy HOMO-LUMO gaps that enabled the MMLCT transitions for all the complexes (Figure 17). Even in Pt-tBu with longer Pt···Pt distances, the formation of the assembled structure is essential for the intense blue emission. Thus, this series of the NHC complexes is outstanding as a complete one that exhibits red to blue emission originating from ^{3}MMLCT. Such wide-range tuning of emission color is simply derived by the change of the Pt···Pt interactions controlled by the bulkiness of the substituent groups on the NHC ligands.
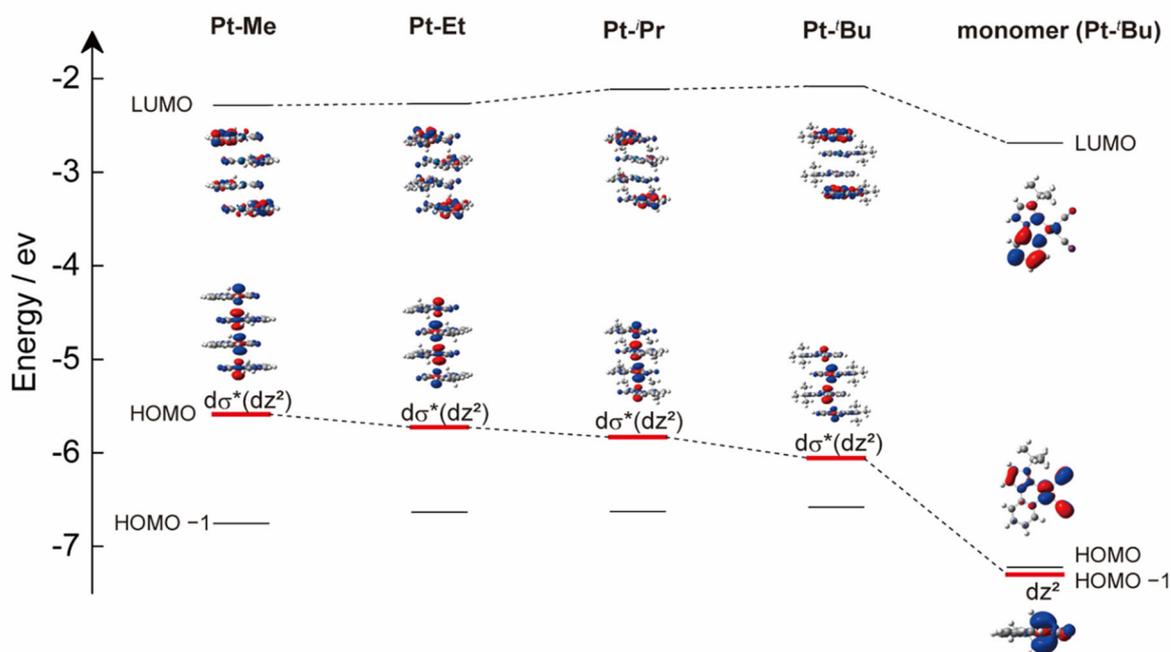
Figure 17. Kohn–Sham orbitals in the frontier region of the singlet ground state, obtained by M06 single-point calculations using crystal structure (isovalue = 0.03)

It is worth mentioning that the ^{3}MMLCT emission was also observed at higher concentrations of glassy solutions (MeOH/EtOH 1:1 v/v) for **Pt-Me**, **Pt-Et**, and **Pt-^{i}Pr**, whereas it was not evident for **Pt-^{t}Bu** (Figures 18–21). This suggests that the steric effect of the bulky tert-butyl group prevented the Pt(II) complex units from assembling with Pt···Pt interactions in the solution. Meanwhile, for the Pt-Me, Pt-Et and Pt-^{i}Pr complexes, a similar broad emission band appeared at approximately 490 nm with an increase in concentration (10^{-5}–10^{-6} M) in addition to the monomer-based $^3\pi\pi^*$ emission (λ_{max} = ~430 nm) observed at a low concentration (1.0×10^{-7} M). The time-resolved emission spectra showed that the band at 490 nm decayed rapidly (τ = 3.8 μs), which can be easily separated from the long-lived $^3\pi\pi^*$ emission (τ = 14 μs) (Figure 23).
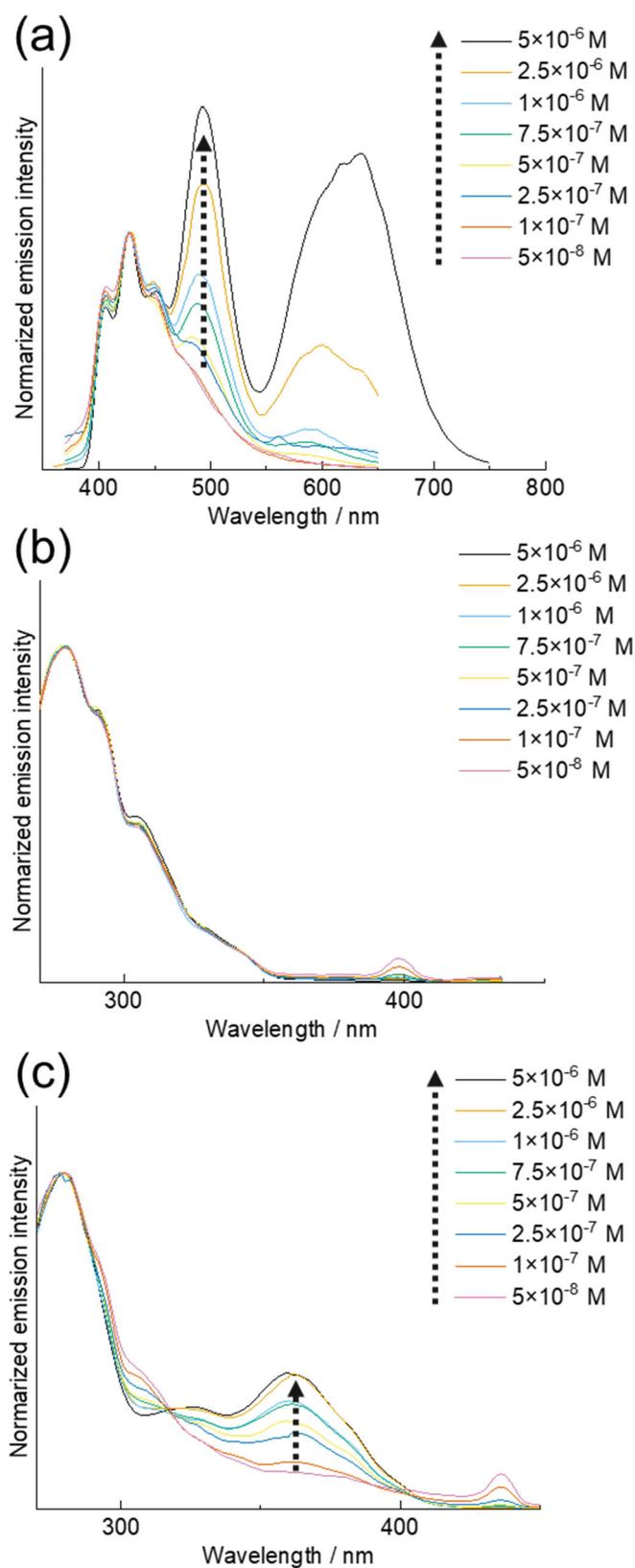
Figure 18. (a) Concentration dependence of emission spectra of **Pt-Me** in EtOH-MeOH (1:1 v/v) at 77 K (λ_{ex} = 280 nm), and corresponding excitation spectra monitored at (b) 450 nm and (c) 500 nm.
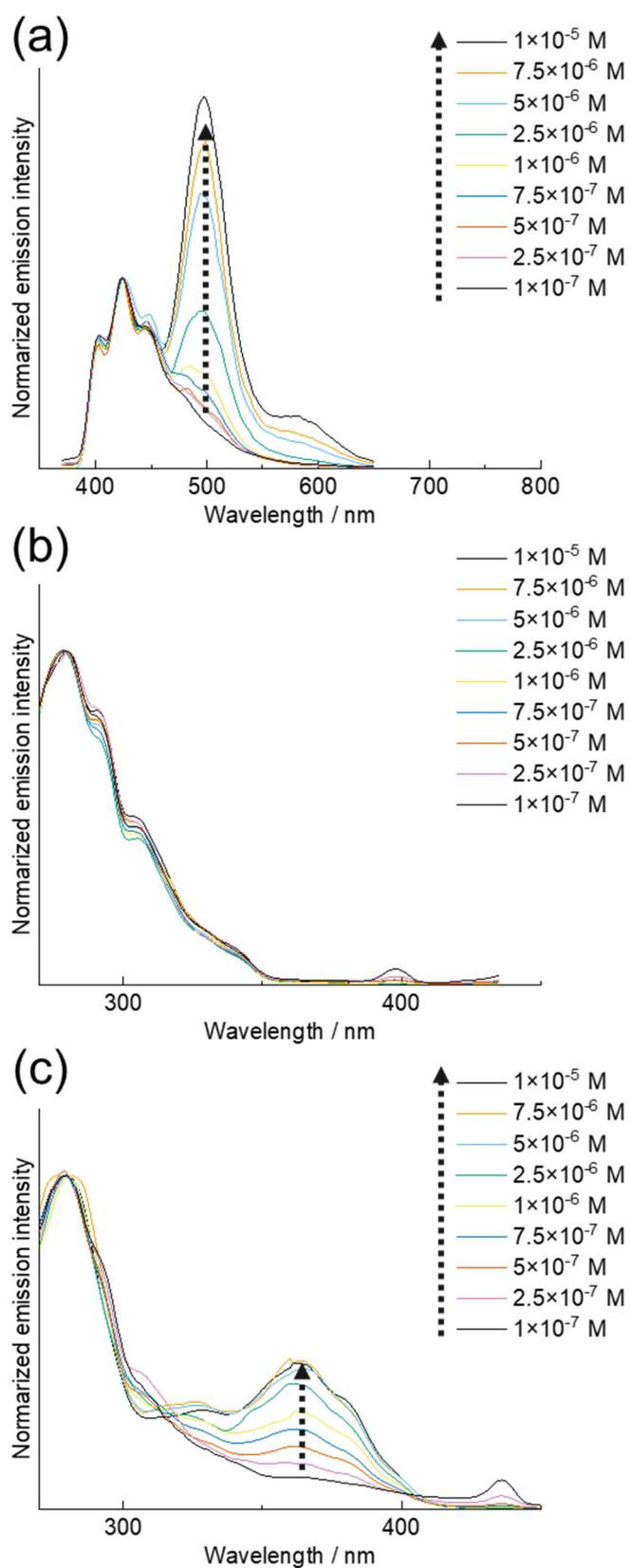
Figure 19. (a) Concentration dependence of emission spectra of **Pt-Et** in EtOH-MeOH (1:1 v/v) at 77 K (λ_{ex} = 280 nm), and corresponding excitation spectra monitored at (b) 450 nm and (c) 500 nm.
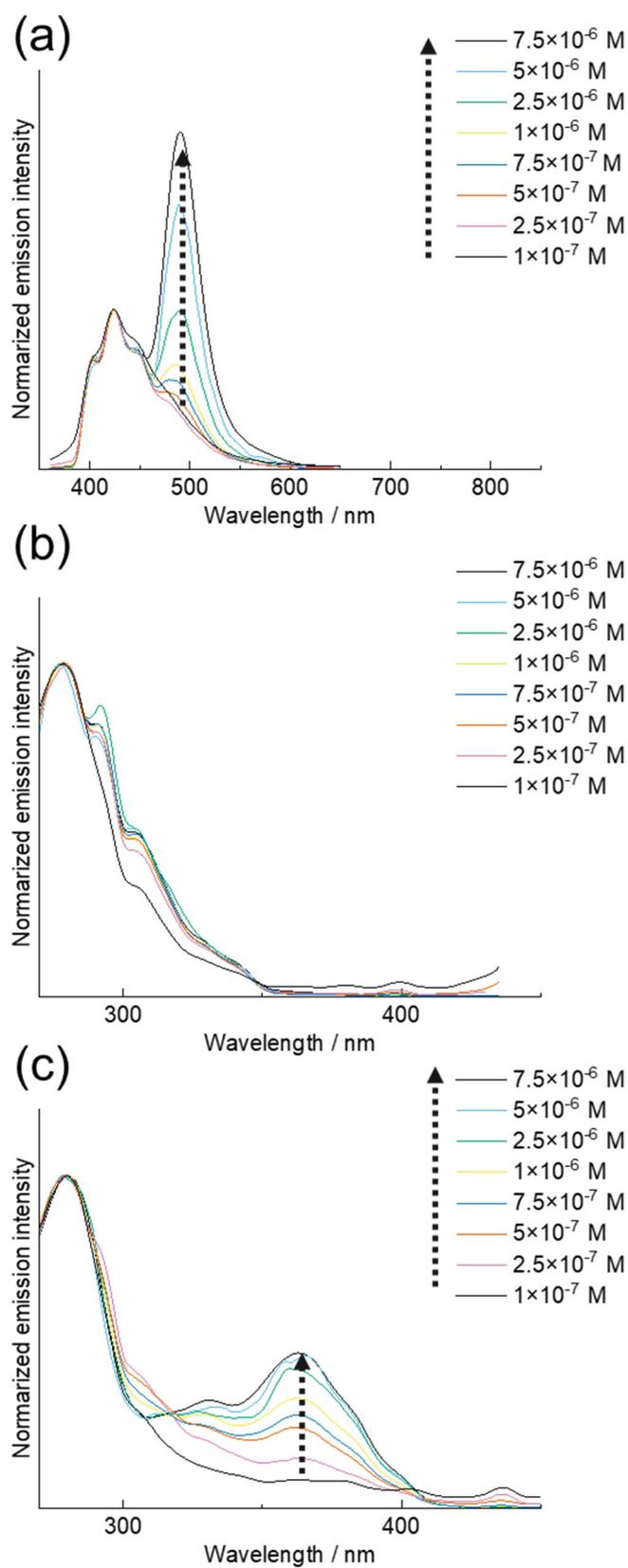
Figure 20. (a) Concentration dependence of emission spectra of **Pt-^{i}Pr** in EtOH-MeOH (1:1 v/v) at 77 K (λ_{ex} = 280 nm), and corresponding excitation spectra monitored at (b) 450 nm and (c) 500 nm.
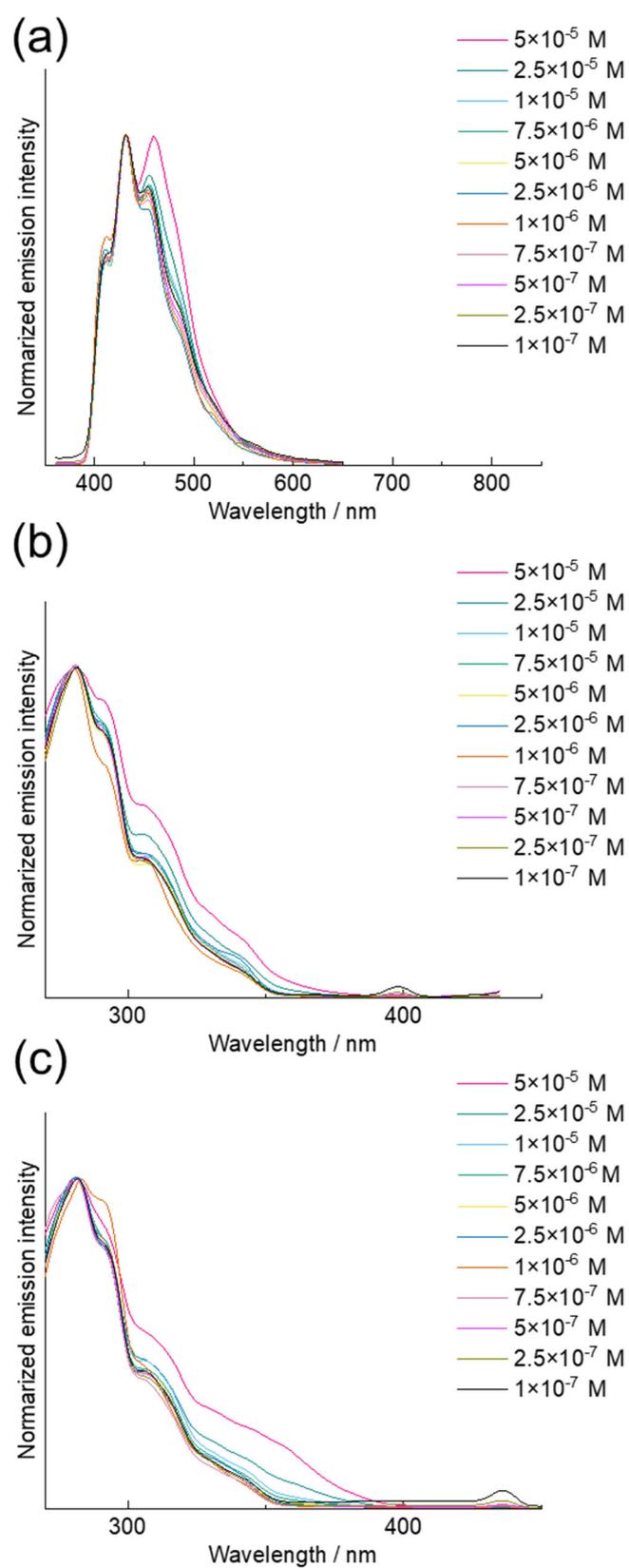
Figure 21. (a) Concentration dependence of emission spectra of **Pt-ᵗBu** in EtOH-MeOH (1:1 v/v) at 77 K (λ_{ex} = 280 nm), and corresponding excitation spectra monitored at (b) 450 nm and (c) 500 nm
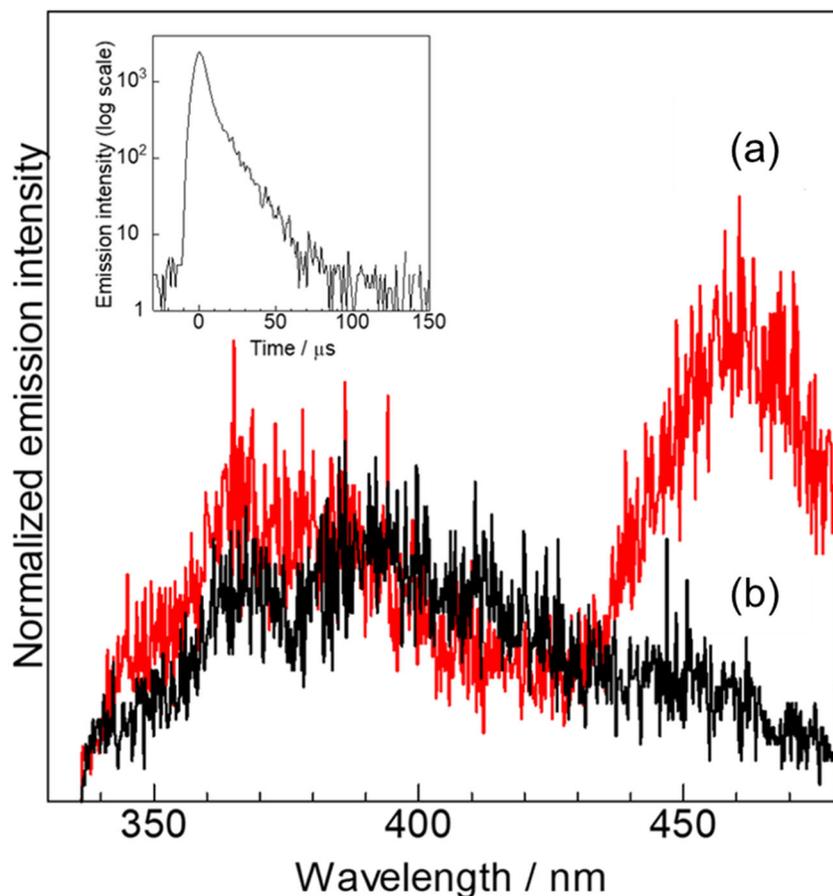
Figure 22. Time-resolved emission spectra of **Pt-Et** in EtOH-MeOH (1:1 v/v) at 77 K (λ_{ex} = 337 nm, c = 1.0×10^{-5} M). The spectrum was exacted (a) in the rage of 0–10 μs, and (b) in the rage of 10–150 μs from the 2D data recorded on a streak camera, respectively. Inset: the emission decay curve of the same data.

Table 9 Photophysical data for **Pt-Me**, **Pt-Et**, **Pt-^{i}Pr**, and **Pt-^{t}Bu** in EtOH-MeOH at 77 K (λ_{ex} = 337 nm).

	λ_{max} / nm	τ / μs
Pt-Me	405, 428, 453	-[a]
Pt-Et	403, 424, 446	14
Pt-^{i}Pr	404, 424, 445	12
Pt-^{t}Bu	413, 432, 454	15

[a] Not detected due to very low solubility.

Table 10. Selected bond length and angles in the optimized structures in S_0 and T_1 states, and the X-ray crystallographic structure.

	Pt-Me			Pt-Et		
	X-ray	S_0	T_1	X-ray	S_0	T_1
Pt1-C1	1.96 (1)	1.96	1.97	1.955(6)	1.96	1.97
Pt1-C2	2.01(1)	2.03	2.04	2.009(6)	2.03	2.04
Pt1-N3	2.08(1)	2.13	2.11	2.089(5)	2.13	2.11
Pt1-C8	2.01(1)	2.04	1.99	2.001(6)	2.04	1.99
N1-C1	1.16(2)	1.16	1.16	1.146(8)	1.16	1.16
N2-C2	1.15(2)	1.16	1.16	1.137(8)	1.16	1.16
C1-Pt1-C2	89.0(6)	88.2	88.1	88.8(2)	87.9	88.1
C1-Pt1-C8	97.6(5)	98.3	98.0	98.9(2)	98.8	98.3
C1-Pt1-N3	176.8(5)	176.0	176.6	177.7(2)	176.4	176.9
C2-Pt1-C8	173.4(5)	173.5	173.8	172.2(2)	173.3	173.6
C2-Pt1-N3	94.2(5)	95.8	95.3	93.3(2)	95.5	95.0
C8-Pt1-N3	79.2(4)	77.7	78.6	79.0(2)	77.8	78.6
	Pt-^{i}Pr			Pt-^{t}Bu		
	X-ray	S_0	T_1	X-ray	S_0	T_1
Pt1-C1	1.961(6)	1.96	1.97	1.945(4)	1.97	1.97
Pt1-C2	2.005(5)	2.03	2.03	2.011(4)	2.01	2.02
Pt1-N3	2.081(5)	2.13	2.11	2.078(3)	2.12	2.11
Pt1-C8	2.015(5)	2.05	1.80	2.057(4)	2.09	2.03
N1-C1	1.139(8)	1.16	1.16	1.152(5)	1.16	1.16
N2-C2	1.144(7)	1.16	1.16	1.130(6)	1.16	1.16
C1-Pt1-C2	88.0(2)	87.8	87.9	86.4(2)	84.8	85.2
C1-Pt1-C8	98.6(2)	99.0	98.4	101.1(2)	103.0	101.9
C1-Pt1-N3	177.4(2)	176.5	177.1	178.5(1)	178.9	178.9
C2-Pt1-C8	173.3(2)	173.2	173.6	172.6(1)	172.2	172.9
C2-Pt1-N3	94.5(2)	95.4	94.9	93.3(2)	94.1	93.8
C8-Pt1-N3	78.9(2)	77.8	78.7	79.4(1)	78.1	79.2

Table 11. Cartesian coordinates of the optimized S_0 structure of **Pt-Me**.

Pt	-0.679022	-0.575197	0.001671
N	3.797584	-0.369021	0.017180
N	-1.449834	-0.587488	-0.003887
N	0.997615	-3.750410	0.004912
N	-1.107028	1.684835	0.006510
N	0.831979	2.605005	-0.007911
C	0.896524	-2.592236	0.002586
C	2.636450	-0.427397	0.008334
C	-1.330284	3.054412	0.010642
C	-0.110051	3.623757	0.002561
C	0.232223	1.412788	-0.003591
C	-2.024798	0.626407	0.004096
C	-2.235178	-1.674188	-0.008962
C	-3.393769	0.805697	0.008169
C	-3.611390	-1.581401	-0.005897
C	2.272062	2.824993	-0.013193
C	-4.195061	-0.323255	0.003187
H	-2.313272	3.496898	0.017140
H	0.182606	4.662088	0.001227
H	-1.728803	-2.633023	-0.015480
H	-3.822741	1.800056	0.014740
H	-4.209233	-2.484715	-0.010325
H	-5.274539	-0.215766	0.006094
H	2.725312	2.291667	-0.849532
H	2.455635	3.893708	-0.123282
H	2.708746	2.476568	0.924545

Table 12. Cartesian coordinates of the optimized S_0 structure of **Pt-Et**.

Pt	-0.068687	-0.940192	-0.004317
N	2.389495	-2.866032	-0.122785
N	2.147360	1.360963	-0.067642
N	-1.677879	0.454086	0.030586
N	0.076947	1.933927	-0.057766
N	-1.936771	-3.524080	0.054463
C	1.487586	-2.134019	-0.072325
C	0.911978	0.852562	-0.040063
C	-1.242132	-2.592155	0.031817
C	2.098014	2.748441	-0.112744
C	-3.955857	1.138627	0.077940
C	-2.216319	2.784983	-0.017988
C	-1.309054	1.743981	-0.014892
C	-3.563088	2.468235	0.029166
C	0.802024	3.113586	-0.102819
C	-2.985084	0.158601	0.076914
C	3.376627	0.549546	-0.083766
C	4.594773	1.326669	0.342864
H	2.985742	3.358735	-0.142442
H	-5.001017	0.856455	0.116716
H	-1.878043	3.813499	-0.056827
H	-4.302870	3.261870	0.028063
H	0.343807	4.089253	-0.119239
H	-3.238617	-0.895133	0.114083
H	3.498028	0.146720	-1.094847
H	3.200964	-0.292935	0.587934
H	5.445466	0.641698	0.387472
H	4.463200	1.766464	1.336727
H	4.850073	2.121977	-0.363520

Table 13. Cartesian coordinates of the optimized S$_0$ structure of **Pt-^{i}Pr**.

Pt	-0.232066	-0.944783	-0.041917
N	-1.817091	0.475561	-0.018024
N	-2.145847	-3.493847	0.010445
N	2.1918	-2.918251	0.009004
N	-0.03795	1.927675	0.024264
N	2.021051	1.325854	-0.075846
C	-1.434653	-2.574431	-0.008939
C	0.779993	0.834278	-0.053016
C	1.301886	-2.170346	-0.02018
C	-1.427199	1.759144	0.030819
C	0.706764	3.095777	0.067455
C	-3.670646	2.516536	0.072744
C	1.996119	2.712241	0.011492
C	-2.318475	2.812956	0.0783
C	4.315423	1.169661	-0.960939
C	3.721803	0.242127	1.303596
C	3.253869	0.506676	-0.111524
C	-3.129572	0.199762	-0.0246
C	-4.084974	1.193609	0.0195
H	0.264571	4.077135	0.128874
H	-4.39783	3.320896	0.109284
H	2.896126	3.306325	0.02236
H	-1.963783	3.835875	0.117381
H	3.933601	1.435375	-1.95145
H	5.145914	0.470152	-1.092625
H	4.717645	2.069636	-0.483161
H	3.991521	1.181779	1.801142
H	4.606443	-0.402338	1.286884
H	2.944343	-0.255204	1.89235
H	2.951824	-0.43128	-0.584747
H	-3.399992	-0.849569	-0.065977
H	-5.134984	0.927385	0.012105

Table 14. Cartesian coordinates of the optimized S_0 structure of **Pt-^{t}Bu**.

Pt	-0.232066	-0.944783	-0.041917
N	-1.817091	0.475561	-0.018024
N	-2.145847	-3.493847	0.010445
N	2.191800	-2.918251	0.009004
N	-0.037950	1.927675	0.024264
N	2.021051	1.325854	-0.075846
C	-1.434653	-2.574431	-0.008939
C	0.779993	0.834278	-0.053016
C	1.301886	-2.170346	-0.020180
C	-1.427199	1.759144	0.030819
C	0.706764	3.095777	0.067455
C	-3.670646	2.516536	0.072744
C	1.996119	2.712241	0.011492
C	-2.318475	2.812956	0.078300
C	4.315423	1.169661	-0.960939
C	3.721803	0.242127	1.303596
C	3.253869	0.506676	-0.111524
C	-3.129572	0.199762	-0.024600
C	-4.084974	1.193609	0.019500
C	0.264571	4.077135	0.128874
H	-4.397830	3.320896	0.109284
H	2.896126	3.306325	0.022360
H	-1.963783	3.835875	0.117381
H	3.933601	1.435375	-1.951450
H	5.145914	0.470152	-1.092625
H	4.717645	2.069636	-0.483161
H	3.991521	1.181779	1.801142
H	4.606443	-0.402338	1.286884
H	2.944343	-0.255204	1.892350
H	2.951824	-0.431280	-0.584747
H	-3.399992	-0.849569	-0.065977
H	-5.134984	0.927385	0.012105
H	-0.232066	-0.944783	-0.041917
H	-1.817091	0.475561	-0.018024
H	-2.145847	-3.493847	0.010445

Table 15. Cartesian coordinates of the optimized T_1 structure of **Pt-Me**.

Pt	0.652643	-0.595257	-0.000629
N	3.785137	-0.533758	0.007529
N	-1.459133	-0.533207	0.002273
N	0.836049	-3.790264	0.009303
N	-1.095072	1.721766	0.002126
N	0.968451	2.623724	-0.006133
C	0.780369	-2.628284	0.004551
C	2.622238	-0.535964	0.004945
C	-1.218422	3.074479	0.029327
C	0.090583	3.602655	0.021401
C	0.315743	1.365220	-0.018177
C	-2.011434	0.721462	-0.001964
C	-2.290790	-1.590555	0.003006
C	-3.400481	0.925528	-0.012648
C	-3.659045	-1.460392	-0.000425
C	2.411430	2.762908	-0.024576
C	-4.220907	-0.170678	-0.010665
H	-2.157736	3.604367	0.061795
H	0.381314	4.644306	0.036033
H	-1.817986	-2.566928	0.007078
H	-3.800830	1.933030	-0.025621
H	-4.280072	-2.348023	0.002308
H	-5.297974	-0.041332	-0.019047
H	2.809707	2.292737	-0.926811
H	2.658920	3.823929	-0.015759
H	2.834777	2.271865	0.854733

Table 16. Cartesian coordinates of the optimized T$_1$ structure of **Pt-Et**.

Pt	-0.079451	-0.933679	-0.000016
N	2.364339	-2.893950	-0.000033
N	2.216618	1.358515	-0.000112
N	-1.670264	0.457258	0.000077
N	0.043615	1.965485	0.000151
N	-1.983771	-3.503669	0.000135
C	1.470973	-2.149388	-0.000076
C	0.910323	0.795998	0.000094
C	-1.280580	-2.576936	0.000065
C	2.153788	2.671359	0.000079
C	-3.957802	1.140535	-0.000147
C	-2.240501	2.816925	-0.000008
C	-1.299311	1.775387	0.000114
C	-3.570853	2.492843	-0.000149
C	0.804905	3.089440	0.000198
C	-2.985291	0.169998	-0.000030
C	3.415550	0.518975	0.000161
C	4.689002	1.317918	-0.000240
H	3.026434	3.309428	0.000099
H	-5.001556	0.850552	-0.000244
H	-1.906458	3.848551	0.000001
H	-4.320081	3.277561	-0.000273
H	0.415297	4.095475	0.000020
H	-3.241142	-0.884237	-0.000026
H	3.344447	-0.128885	-0.880536
H	3.344486	-0.128221	0.881352
H	5.533520	0.624855	0.000152
H	4.773622	1.949544	0.889853
H	4.773652	1.948527	-0.891052

Table 17. Cartesian coordinates of the optimized T$_1$ structure of **Pt-^{i}Pr**.

Pt	-0.222468	-0.934838	-0.045594
N	-1.813581	0.452291	0.014576
N	-2.124424	-3.505381	-0.003992
N	2.219232	-2.895931	-0.152269
N	-0.102841	1.964588	-0.020916
N	2.070346	1.365451	-0.108522
C	-1.422197	-2.578058	-0.018836
C	0.768678	0.797908	-0.048592
C	1.324800	-2.153404	-0.114689
C	-1.444320	1.771753	0.017187
C	0.651974	3.092397	-0.052082
C	-3.715905	2.486315	0.092522
C	2.001057	2.678975	-0.104143
C	-2.386831	2.811988	0.055560
C	4.464582	1.277117	-0.683870
C	3.562280	0.106963	1.350752
C	3.295619	0.538029	-0.078460
C	-3.127500	0.163614	0.052747
C	-4.100801	1.132835	0.091645
H	0.256860	4.096227	-0.047807
H	-4.466050	3.269526	0.123129
H	2.871182	3.320257	-0.136204
H	-2.053902	3.844048	0.054824
H	4.239309	1.642304	-1.690546
H	5.310388	0.587691	-0.752732
H	4.779184	2.120632	-0.059315
H	3.818016	0.979098	1.964250
H	4.405419	-0.590330	1.368461
H	2.695472	-0.392555	1.793023
H	3.052984	-0.335723	-0.692993
H	-3.382412	-0.890867	0.051034
H	-5.143731	0.841345	0.120646

Table 18. Cartesian coordinates of the optimized T_1 structure of **Pt-ᵗBu**.

Pt	-0.387892	-0.927331	-0.000098
N	-1.913314	0.528329	0.000066
N	-0.146726	1.972373	-0.000242
N	-2.439470	-3.365071	0.000532
N	2.039057	1.360607	-0.000093
N	1.778328	-3.189994	0.000287
C	0.713888	0.779797	-0.000863
C	-1.685750	-2.479194	0.000262
C	1.012510	-2.314442	0.000137
C	3.350549	-0.256742	-1.274215
C	-3.238710	0.288392	0.000191
C	-4.175067	1.293171	0.000166
C	3.315951	0.574591	-0.000132
C	0.615399	3.091340	0.000848
C	-1.494128	1.826222	-0.000235
C	3.350564	-0.256667	1.274059
C	-3.737838	2.628744	-0.000214
C	1.957734	2.672217	0.000891
C	4.497488	1.527035	-0.000179
C	-2.396290	2.902559	-0.000457
H	2.478213	-0.902184	-1.381393
H	4.242643	-0.891478	-1.260165
H	3.407552	0.400155	-2.149122
H	-3.534359	-0.754928	0.000342
H	-5.228824	1.042057	0.000351
H	0.232651	4.100078	0.002315
H	3.408656	0.400298	2.148839
H	4.242032	-0.892278	1.259601
H	2.477662	-0.901276	1.381806
H	-4.456294	3.441829	-0.000376
H	2.820660	3.321930	0.001518
H	4.520363	2.159384	-0.894095
H	5.408502	0.921365	-0.000230
H	4.520554	2.159319	0.893770
H	-2.027382	3.921728	-0.000937

Table 19. Computed spin densities of the T_1 minimum of **Pt-Me.**

Pt1	0.177007
N2	0.020876
N3	0.133450
N4	0.047570
C5	-0.038097
N6	0.014567
C7	-0.022396
N8	0.045792
C9	0.406154
H10	-0.014696
C11	0.259571
H12	-0.008929
C13	0.701569
C14	0.104329
C15	-0.012674
H16	0.000723
C17	-0.005345
H18	-0.000532
C19	0.120020
H20	-0.004656
C21	-0.001011
C22	0.058980
H23	-0.002103
H24	0.010226
H25	-0.000575
H26	0.010179

Table 20. Computed spin densities of the T$_1$ minimum of **Pt-Et.**

Pt1	0.804770
N2	-0.439897
C3	-0.463406
N4	0.164755
C5	-0.636415
N6	-0.049251
N7	0.340172
N8	-0.469223
C9	-0.048790
C10	-0.358795
H11	0.269384
C12	-0.515820
H13	0.215192
C14	-0.101036
H15	0.214785
C16	0.043295
C17	-0.398561
H18	0.222605
C19	0.232278
H20	0.266304
C21	0.140001
H22	0.213148
C23	0.084177
H24	0.236950
H25	0.237088
C26	-0.780272
H27	0.212764
H28	0.181847
H29	0.181953
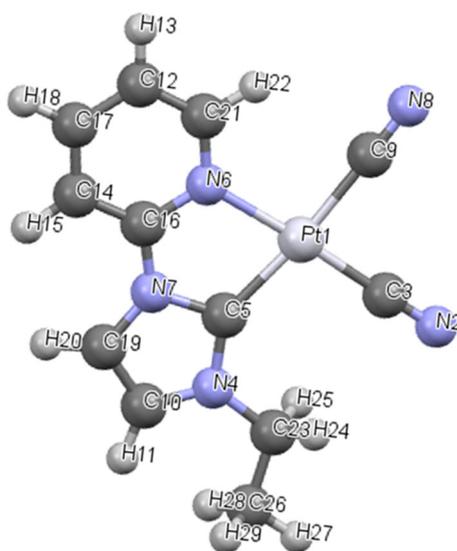
Table 21. Computed spin densities of the T$_1$ minimum of **Pt-^{i}Pr.**

Pt1	0.167170
C2	-0.033731
N3	0.132721
N4	0.046267
N5	0.018062
N6	0.018127
C7	0.685196
C8	-0.015469
N9	0.039786
C10	0.104631
C11	0.398373
H12	-0.014830
C13	0.050027
H14	-0.002140
C15	0.267025
H16	-0.009066
C17	0.013201
H18	-0.000416
C19	0.004518
H20	0.000362
H21	-0.000248
H22	0.000244
C23	-0.003229
H24	-0.000029
H25	0.000780
H26	0.001192
C27	0.025549
H28	0.004766
C29	-0.025035
H30	0.000690
C31	0.130170
H32	-0.004663
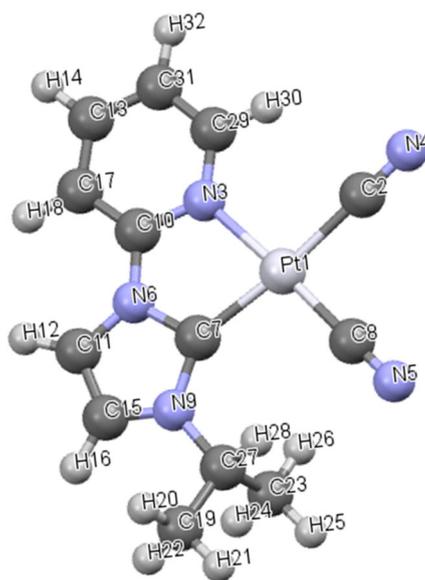
Table 22. Computed spin densities of the T$_1$ minimum of **Pt-^{t}Bu.**

Pt1	0.137722
N2	0.126300
N3	0.019856
N4	0.043022
N5	0.051421
N6	0.016569
C7	0.760295
C8	-0.029675
C9	-0.013477
C10	0.012969
H11	0.002649
H12	0.000932
H13	-0.000243
C14	-0.026890
H15	0.000735
C16	0.121596
H17	-0.004494
C18	-0.007518
C19	0.429736
H20	-0.015329
C21	0.085098
C22	0.012975
H23	-0.000246
H24	0.000929
H25	0.002650
C26	0.047149
H27	-0.001780
C28	0.219516
H29	-0.009243
C30	0.002760
H31	0.000082
H32	-0.000631
H33	0.000081
C34	0.015086
H35	-0.000604
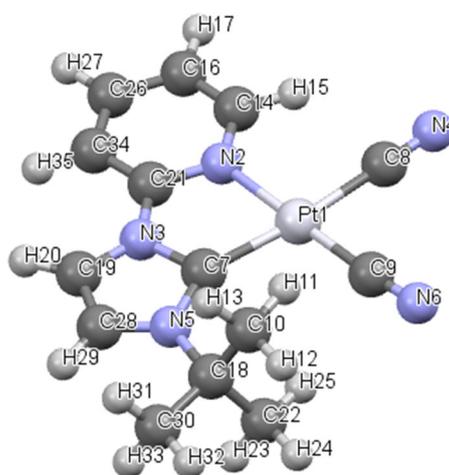
2.3.3 Correlation between ^{3}MMLCT emission energies and Pt···Pt distances

The relationship between the Pt···Pt distance and the absorption/emission energy was reported for some linearly stacked Pt(II) complexes.[4a,46] This correlation has been explained from the viewpoints of the (i) electrostatic coupling of the transition dipole moments (*i.e.* Davydov splitting) and (ii) orbital overlapping and delocalization of the excited electron.[47] For a series of $[Pt(CN)_4]^{2-}$ with different cations, good linear correlations between absorption/emission energies and R^{-3} (R: Pt···Pt distance) were reported and investigated for the intra-metal (dσ*-pσ) transition in detail.[46] Interestingly, such simple correlations were also applicable for the ^{3}MMLCT emission for $[Pt(bpy)Cl_2]$[48] and $[Pt(bpy)(CN)_2]$.[49] However, the rationality of this model has not been sufficiently investigated.

To evaluate the presence or absence of the delocalization of Pt···Pt interactions in the infinite stacks of the Pt(II) complexes having two crystallographically independent Pt···Pt distances, the emission maximum energies were plotted against R^{-3} using the average Pt···Pt distances (R_{ave}) (Figure 23a) and the shortest Pt···Pt distances (Rs) (Figure 23b) at 250 K. As can be seen, a better linear relationship is obtained using the average Pt···Pt distance (coefficient of determination, r^2 = 0.974, Figure 4a) than using the dimer-based model (r^2 = 0.794, Figure 23b). These results suggest that the Pt···Pt electronic interactions are delocalized throughout the one-dimensional chain to some extent including **Pt-^{t}Bu** with the long Pt···Pt distance.
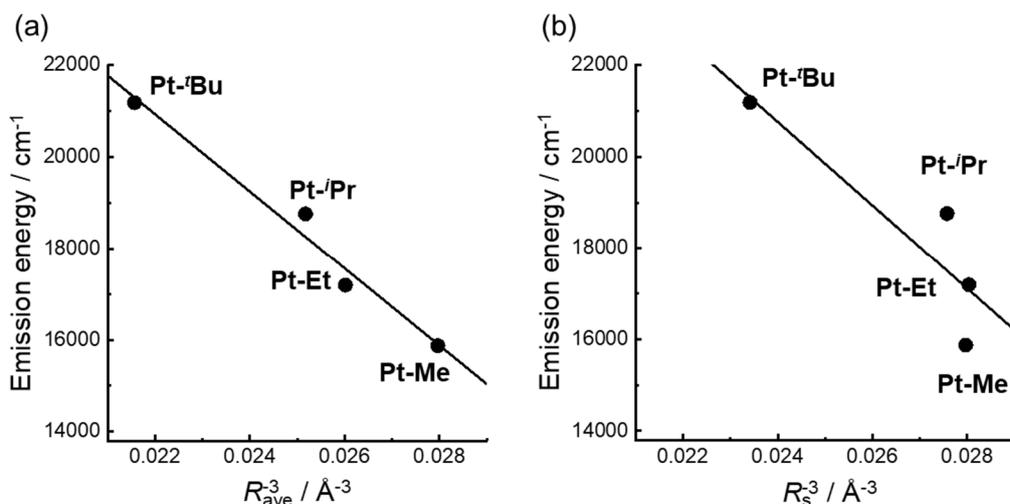

Figure 23. Correlation between emission maximum energies and Pt···Pt distances at 250 K, where the (a) average Pt···Pt distances (R_{av}) and (b) shortest Pt···Pt distances (R_s) were taken as the horizontal axis. The lines show the least-square linear fitting results.

2.3.4 Temperature dependence of Pt···Pt distances and emission spectra

To gain more insight into the Pt···Pt interactions, variable-temperature single-crystal X-ray structural analysis and emission measurements were carried out. The crystallographic parameters at each temperature are summarized in Tables 3–6. No phase transitions were observed for the four complexes in this temperature range; however, a gradual thermal increase in the cell length was observed (Figure 24). Interestingly, an anisotropic shrinkage of the b axis, which is the Pt···Pt chain direction, was observed for **Pt-Me** and **Pt-Et**, while for **Pt-^{i}Pr**, and **Pt-^{t}Bu**, some degree of shrinkage along the c axis was also observed as well as the shrinkage along the b axis, which is probably because of the presence of solvated water molecules between the Pt-complex columns in the **Pt-^{i}Pr**, and **Pt-^{t}Bu** crystals. Nevertheless, the Pt···Pt distances in all the complexes decreased similarly with a decrease in temperature from 250 K to 100 K (Figure 25). The Pt···Pt···Pt angles in all the complexes did not show any remarkable temperature dependence (Figure 26). Such an anisotropic shrinkage of the crystal lattice has been reported for self-assembled Pt(II) complexes.[34-36]
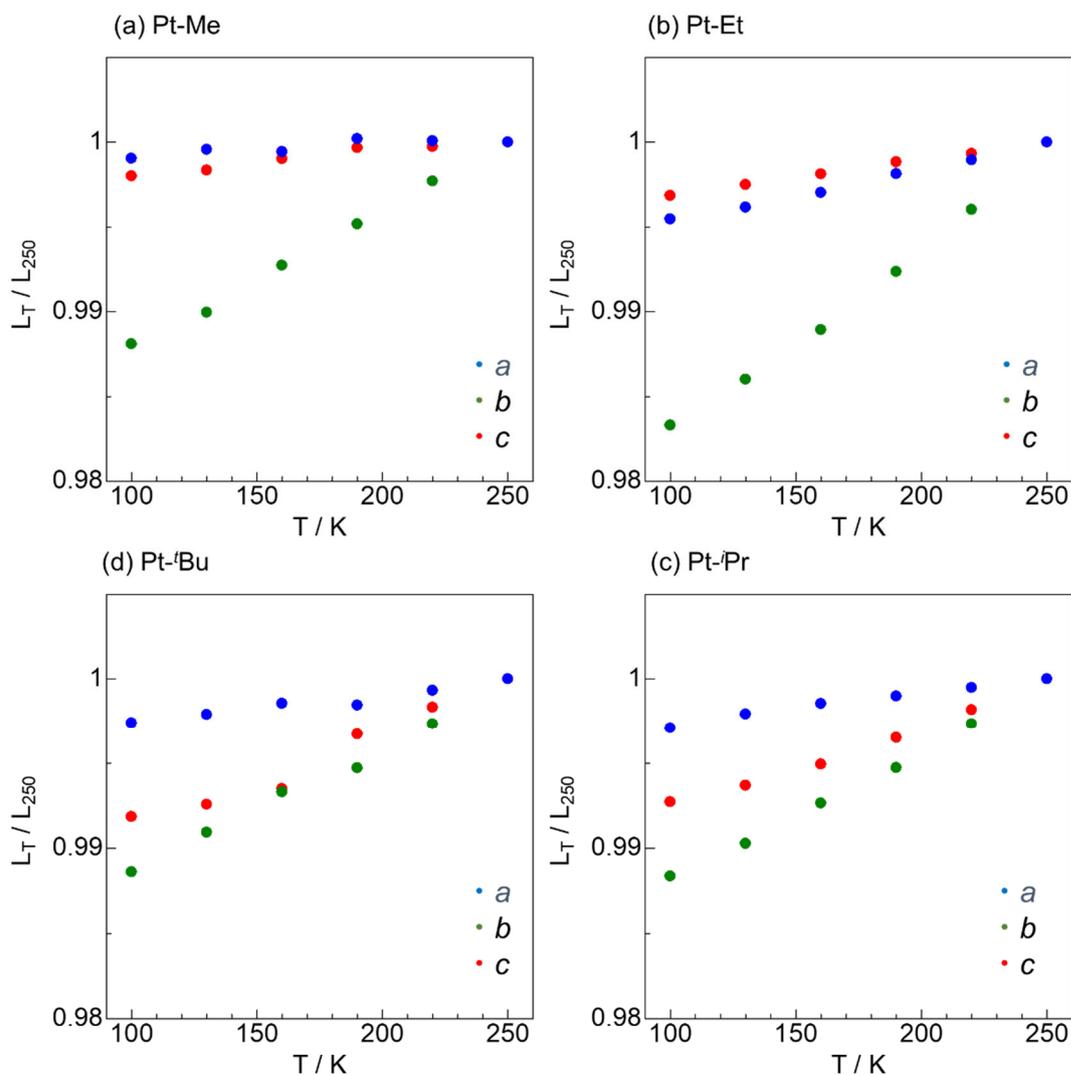

Figure 24. Ratio of cell lengths (*a*, *b*, and *c*) of (a) **Pt-^{t}Bu**, (b) **Pt-^{i}Pr**, (c) **Pt-Et**, and (d) **Pt-Me** relative to that at 250 K.
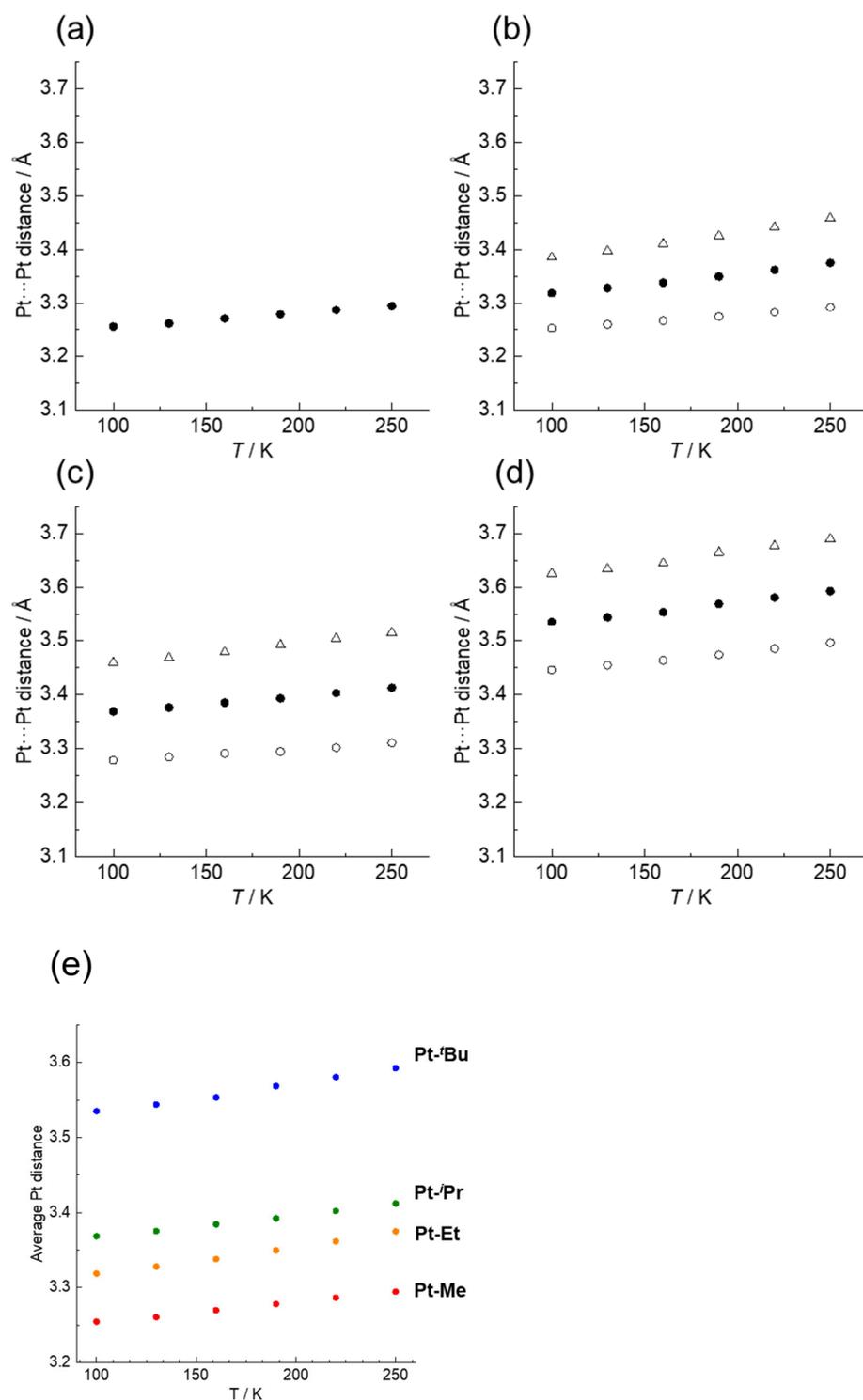
Figure 25. Temperature dependence of the Pt···Pt distance of (a) **Pt-Me**, (b) **Pt-Et**, (c) **Pt-^{i}Pr**, and (d) **Pt-^{t}Bu**. White circles, black dots, and white triangles indicate the shortest, the average, and the longest Pt···Pt distances. (e) The comparison of the average Pt···Pt distance. The numerical data are summarized in Table 10.
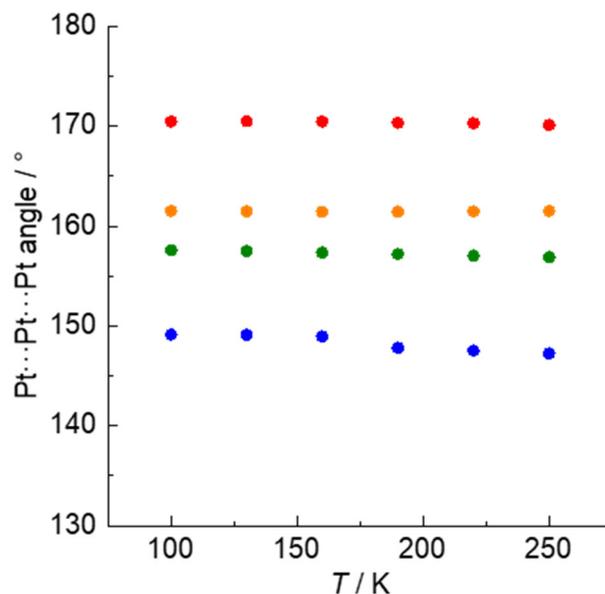
Figure 26. The temperature dependence of the Pt⋯Pt⋯Pt angle of **Pt-Me** (red), **Pt-Et** (orange), **Pt-^{i}Pr** (green), and **Pt-^{t}Bu** (blue).

Table 10. Pt⋯Pt distances and Pt⋯Pt⋯Pt angles at various temperatures during 100–250 K.

	T / K	100	130	160	190	220	250
Pt-Me	Pt1-Pt1'	3.2544(2)	3.2604(2)	3.2697(2)	3.2780(2)	3.2864(2)	3.2945(3)
	Pt1-Pt1''	170.46(5)	170.51(6)	170.46(5)	170.33(5)	170.29(5)	170.11(6)
Pt-Et	Pt1-Pt1'	3.2520(2)	3.2588(2)	3.2656(2)	3.2736(2)	3.2822(2)	3.2919(2)
	Pt1-Pt1''	3.3852(2)	3.3972(2)	3.4104(2)	3.4255(2)	3.4412(2)	3.4579(2)
	Pt1'-Pt1-	161.51(1)	161.45(1)	161.43(1)	161.43(1)	161.46(1)	161.51(1)
Pt-^{i}Pr	Pt1-Pt1'	3.2780(2)	3.2837(2)	3.2906(2)	3.2937(2)	3.3011(2)	3.3101(2)
	Pt1-Pt1''	3.4588(2)	3.4670(2)	3.4780(2)	3.4908(2)	3.5032(2)	3.5142(2)
	Pt1'-Pt1-	157.57(1)	157.49(1)	157.34(1)	157.19(1)	157.03(1)	156.88(1)
Pt-^{t}Bu	Pt1-Pt1'	3.4449(2)	3.4538(2)	3.4628(2)	3.4730(2)	3.4844(2)	3.4955(2)
	Pt1-Pt1''	3.6257(2)	3.6343(2)	3.6446(2)	3.6646(2)	3.6772(2)	3.6900(2)
	Pt1'-Pt1-	149.13(1)	149.08(1)	148.94(1)	147.80(1)	147.51(1)	147.25(1)

Concomitantly, thermochromic changes normally occur in the ^{3}MMLCT emission, and as expected, the emission spectra of **Pt-Me**, **Pt-Et**, and **Pt-^{i}Pr** exhibited remarkable red-shifts with decreasing temperature (Figure 5). However, no spectral shift was observed for **Pt-^{t}Bu** though the spectral bands became shaper and stronger with decreasing temperature. This implies that the electronic effect due to the structural changes is very small even if the Pt⋯Pt distance changes with temperature similar to that observed for the other three complexes. The emission band of **Pt-^{t}Bu** with a maximum of approximately 485 nm is close to the assembled dimer emission at approximately 490 nm in glassy solutions for **Pt-Me**, **Pt-Et**, and **Pt-^{i}Pr** (Figures 18–21). These emission bands appeared at almost the same wavelength for the three complexes, which indicates the ^{3}MMLCT energy of the dimeric species of [Pt(CN)$_2$(R-impy)]. Considering that the crystal structure of **Pt-^{t}Bu** has the stacking mode C (Figure 1), the solid-state emission of **Pt-^{t}Bu** will be mainly based on dimeric interactions. In addition, the weaker "inter-dimer" interactions perturb the ^{3}MMLCT transition energy.[50,51] In fact, Nakagaki *et al*. reported very recently that the red-shift with a decresing temperature of the ^{3}MMLCT emission for the [Pt(bpy)(CN)$_2$] crystal (red form) can be explained by the expansion of the excitation from trimer to tetramer in the triplet excited state.[52] [Pt(bpy)(CN)$_2$] forms a typical parallel stack of the type A (Figure 1), and **Pt-Me**, **Pt-Et**, and **Pt-^{i}Pr** can be categorized in the same group from the emission properties. For **Pt-^{t}Bu** adopting a typical stacking mode of the type C (Figure 1), however, the excitation could be localized mainly in the dimer of the stacking structure, which would enable the emission energy higher than the others.
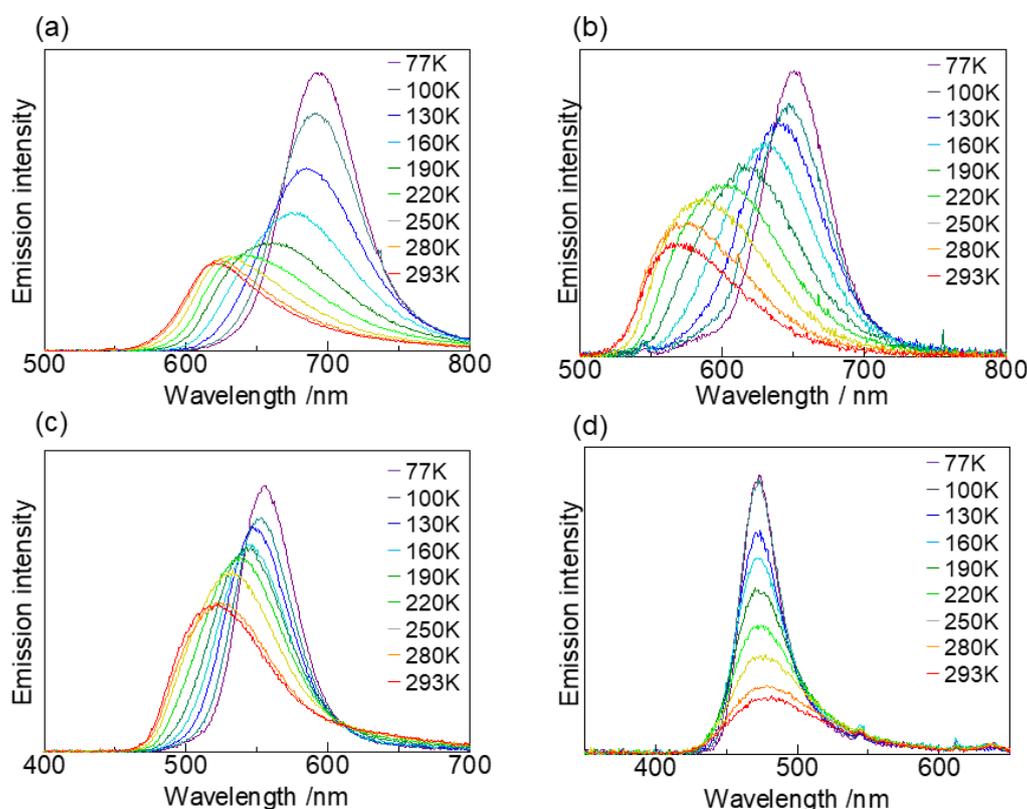

Figure 27. Temperature dependence of the emission spectra of (a) **Pt-Me**, (b) **Pt-Et**, (c) **Pt-^{i}Pr**, and (d) **Pt-^{t}Bu** in the solid states (λ_{ex} = 337 nm).

In Figure 28, the maximum emission energies are plotted against the average Pt⋯Pt distance (R_{ave}). Each set of complexes, **Pt-Me** (red), **Pt-Et** (orange), **Pt-^{i}Pr** (green), and **Pt-^{t}Bu** (blue), exhibits a linear correlation with slopes of (3.7, 3.2, 1.5, and 0.1) $\times 10^4$ cm^{-1} Å^{-1}, respectively. The slope decreases with increasing Pt⋯Pt distance in the order of **Pt-Me**, **Pt-Et**, **Pt-^{i}Pr**, and **Pt-^{t}Bu**. These are roughly fitted using an exponential function.[39] This clearly shows that the limit of the Pt⋯Pt interaction is in the region of 3.5–3.6 Å. Since Bondi suggested the van der Waals radius of Pt can be in the region of 1.72–1.75 Å using limited data with the comment that the estimation was not certain,[45] accumulated structural data of Pt complexes with stacking structures indicated that formally non-bonding but generate electronically interactive Pt⋯Pt distances were found within 3.5–3.6 Å.[4a,5.12,48] Our results provide an accurate experimental confirmation of the limit.
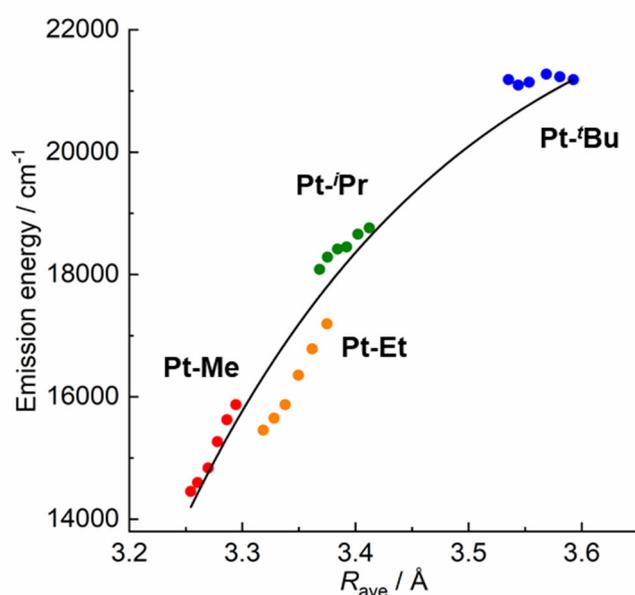

Figure 28. Correlation between maximum emission energies and Pt⋯Pt distances (R_{ave}) for all the **Pt-R** complexes from 100 K to 250 K: **Pt-Me** (red), **Pt-Et** (orange), **Pt-^{i}Pr** (green), and **Pt-^{t}Bu** (blue). The black solid line is a least-square fit based on the equation: E [cm^{-1}] = $-(4.15 \times 10^9)$exp($-R_{ave}$ [Å]/0.250) + (2.36×10^4).

2.3.5 Temperature dependence of emission lifetimes

The most notable feature in the phosphorescent state with a charge-transfer character based on metal orbitals is the large zero-field splitting (ZFS), which causes a remarkable temperature dependence on the emission intensity and lifetime.[53–55] To obtain detailed information on the emission states of **Pt-^{t}Bu**, the temperature dependence of the emission lifetimes was investigated and compared with that of **Pt-Me**. As shown in Figure 29, both the complexes exhibit significant increases in lifetimes with a decrease in temperature to below 77 K. The data were analyzed using eq. 1.

Where kn (n = I, II, and III) is the decay rate constant of the individual sub-levels of the triplet state (T$_1$), andΔE$_{\text{I-II}}$ and ΔE$_{\text{I-III}}$ are the energy separations between the sub-levels. For **Pt-^{t}Bu**, all the data were available because no spectral shifts were observed in the temperature range of 4–298 K (Figure 30). However, the data between 4 and 77 K were applied for the analyses because the emission energies became constant in the temperature region for **Pt-Me**. The energy diagrams of the obtained triplet spin sublevels are shown as insets in Figure 29 (Table 11 for all the parameters). The ΔEI-III values of approximately 50–70 cm^{-1} are not so large compared to the ZFS energies of the ^{3}MLCT states of luminescent Ru(II) and Ir(III) complexes with polypyridine ligands (100–200 cm^{-1}).[52,53] The ZFS energy of the ^{3}MMLCT state of a discrete dinuclear cyclometalated Pt(II) complex connected with a bridging ligand has been estimated as 150 cm^{-1}.[56] The smaller ZFS values of the present systems compared with that of the discrete dinuclear system, which are much larger than those of the $^3\pi\pi^*$ states, could be another characteristic of the ^{3}MMLCT states in self-assembled systems.

$$\tau = \frac{1}{k_{obs}} = \frac{1 + \exp\left(\frac{-E_1}{k_B T}\right) + \exp\left(\frac{-E_2}{k_B T}\right)}{k_0 + k_1 \exp\left(\frac{-E_1}{k_B T}\right) + k_2 \exp\left(\frac{-E_2}{k_B T}\right)} \quad (eq.\,1)$$
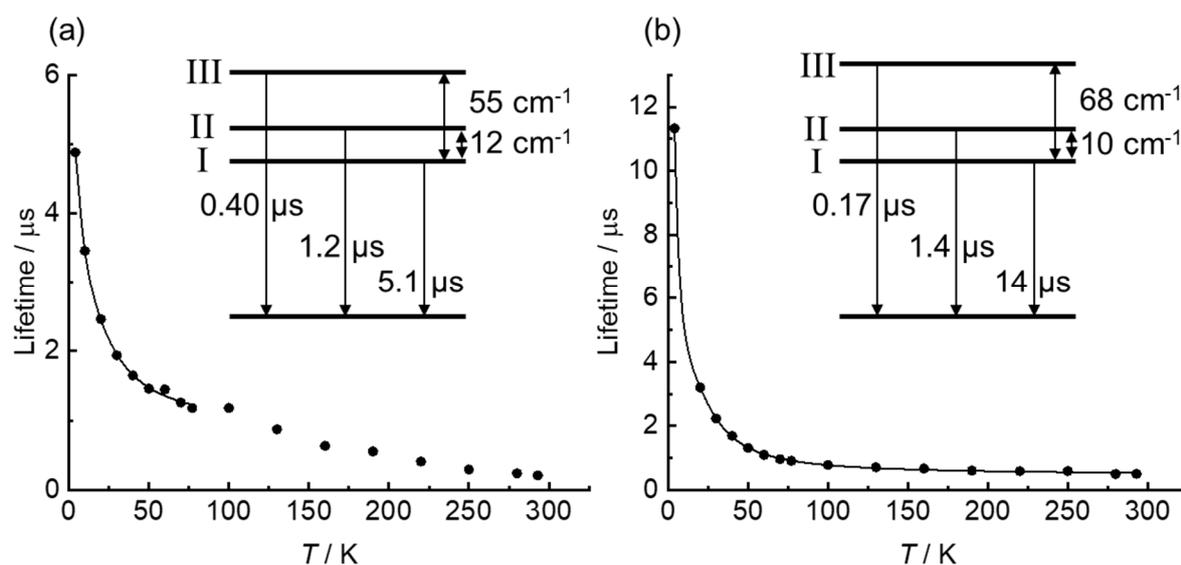

Figure 29. Temperature dependence of the emission lifetimes of the complexes: (a) **Pt-Me** and (b) **Pt-^{t}Bu**. The solid thin lines are the fitting results based on eq. 1, and the parameters are summarized in the insets as the sublevels of the phosphorescence states, respectively. Inset: Energy diagrams of the triplet spin sublevels.

Table 11. Fitting parameters for the spin sublevels of ^{3}MMLCT state based on the temperature-dependent lifetimes.

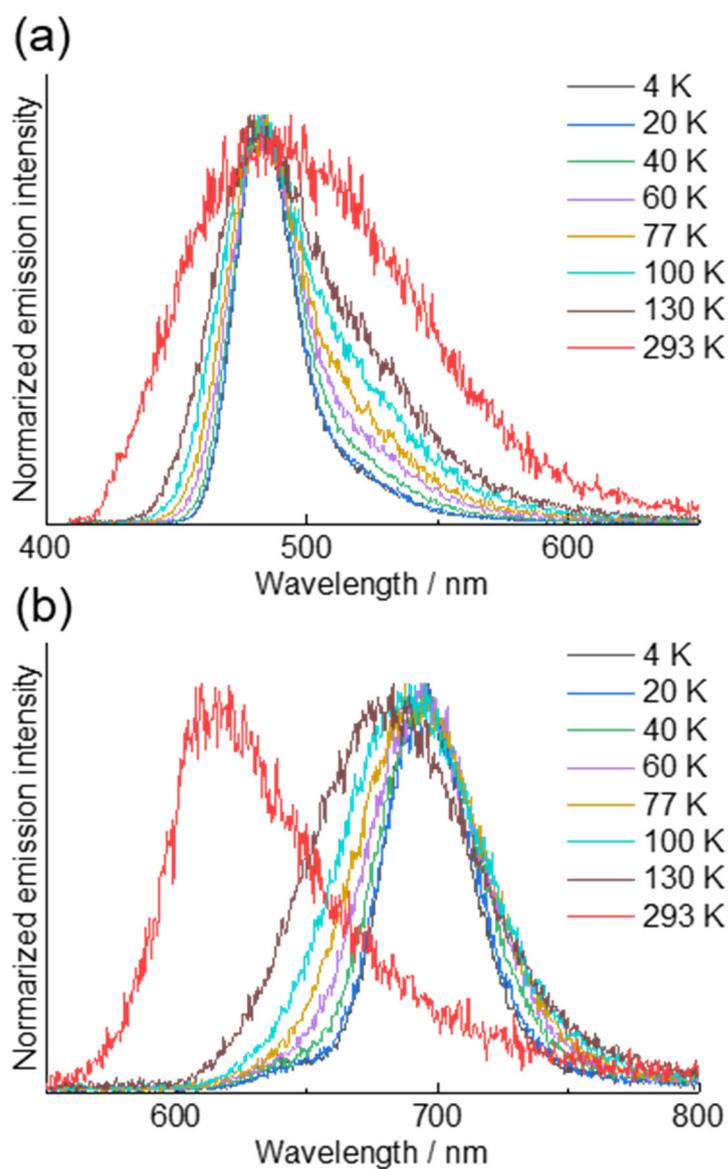|	k_I / s^{-1}	k_{II} / s^{-1}	ΔE_{I-II} / cm^{-1}	k_{III} / s^{-1}	ΔE_{I-III} / cm^{-1}
Pt-Me	$(2.0 \pm 0.1) \times 10^5$	$(8.1 \pm 2) \times 10^5$	12 ± 3	$(2.5 \pm 0.3) \times 10^6$	55 ± 16
Pt-^{t}Bu	$(7.0 \pm 5) \times 10^4$	$(7.3 \pm 2) \times 10^5$	9.9 ± 8	$(5.8 \pm 0.2) \times 10^6$	68 ± 10

Figure 30. The temperature dependence of the emission spectra of (a) **Pt-^{t}Bu** and (b) **Pt-Me** in the solid state (4–293 K, λ_{ex} = 400 nm)

2.4 Conclusion

In conclusion, a new series of assembled Pt(II)-NHC complexes that covers the entire visible region and serves as ^{3}MMLCT emitters were developed. The four neutral Pt(II)-NHC complexes (**Pt-Me**, **Pt-Et**, **Pt-^{i}Pr**, and **Pt-^{t}Bu**) exhibited highly efficient photoluminescence (Φ = 0.51–0.81) with different colors ranging from red (**Pt-Me**), orange (**Pt-Et**), and green (**Pt-^{i}Pr**) to blue (**Pt-^{t}Bu**) in the solid state at room temperature. This is because of the fine control of Pt···Pt distances in the self-assembled stacking structures in the order of 0.01 Å by the introduction of alkyl groups on the imidazolium ring of the NHC ligands. Notably, **Pt-^{t}Bu** is remarkable as the first example of an emitter that exhibits a blue ^{3}MMLCT emission. The nature of the Pt···Pt electronic interactions through detailed investigation by crystal structure analysis and emission spectroscopy including temperature dependence and time-resolved approaches. It is interesting to note that the good correlation between the Pt···Pt distance and emission energy is not a simple linear correlation as reported before but includes distance-dependent interactions. Furthermore, the stacking mode is an important factor for controlling the Pt···Pt electronic interactions effectively, and the dimeric interaction in the inequivalent stacks results in weak Pt···Pt electronic interactions. Nevertheless, the average Pt···Pt distance exhibits a good correlation with the emission energy, which suggests the delocalization of the excited electron throughout the Pt stack. In addition, the correlation clearly indicated the limit distance of the interactions, which is approximately 3.5–3.6 Å. These assembled systems are remarkable in that they show both flexibility and order.[57] As described herein, these crystalline systems enable an in-depth analysis, providing deeper insights into the luminescence properties. The wide-range color tuning of luminescence using the ^{3}MMLCT emission presents a new strategy for constructing efficient luminescent materials that exhibit desirable colors and favorable exciton lifetimes. In addition, these systems can be promising as new photofunctional materials for sensing and optical devices.

References

[1] D. Philp, J. F. Stoddart, *Angew. Chem. Int. Ed.* **1996**, *35*, 1154–1196.

[2] G. M. Whitesides, B. Grzybowski, *Science.* **2002**, *295*, 2418–2421.

[3] K. Harris, D. Fujita, M. Fujita, *Chem. Commun.* **2013**, *49*, 6703–6712.

[4] a) T. W. Thomas, A. E. Underhill, *Chem. Soc. Rev.* **1972**, *1*, 99–120

b) M. Hissler, J. E. McGarrah, W. B. Connick, D. K. Geiger, S. D. Cummings, R. Eisenberg, *Coord. Chem. Rev.* **2000**, *208*, 115–137

c) K. M.-C. Wong, V. W.-W. Yam, *Coord. Chem. Rev.* **2007**, *251*, 2477–2488.

[5] a) O. S. Wenger, *Chem. Rev.* **2013**, *113*, 3686–3733;

b) X. Zhang, B. Li, Z.-H. Chen, Z.-N. Chen, *J. Mater. Chem.* **2012**, *22*, 11427–11441;

c) M. Kato, *Bull. Chem. Soc. Jpn.* **2007**, *80*, 287–294.

[6] A. S. Y. Law, L. C. C. Lee, M. C. L. Yeung, K. K. W. Lo, V. W.-W. Yam, *J. Am. Chem. Soc.* **2019**, *141*, 18570–18577.

[7] A. Aliprandi, M. Mauro, L. De Cola, *Nat. Chem.* **2016**, *8*, 10–15.

[8] a) J. A. Bailey, M. G. Hill, R. E. Marsh, V. M. Miskowski, W. P. Schaefer, H. B. Gray, *Inorg. Chem.* **1995**, *34*, 4591–4599.

b) V. W.-W. Yam, L.-P. Chan, T.-F. Lait, *Organometallics* **1993**, *12*, 2197-2202. c) V. H. Houlding, V. M. Miskowski, *Coord. Chem. Rev.* **1991**, *111*, 145-152.

[9] L. Le Bras, K. Chaitou, S. Aloïse, C. Adamo, A. Perrier, *Phys. Chem. Chem. Phys.* **2019**, *21*, 46–56.

[10] a) J. Luo, Z. Xie, Z. Xie, J. W. Y. Lam, L. Cheng, H. Chen, C. Qiu, H. S. Kwok, X. Zhan, Y. Liu, D. Zhu, B. Z. Tang, *Chem. Commun.* **2001**, *18*, 1740–1741

 b) X. Cai, B. Liu, *Angew. Chem. Int. Ed. Engl.* **2020**, *59*, 9868–9886

c) Z. Zhao, H. Zhang, J. W. Y. Lam, B. Z. Tang, *Angew. Chem. Int. Ed. Engl.* **2020**, *59*, 9888–9907.

11) a) Y. Han, Z. Gao, C. Wang, R. Zhong, F. Wang, *Coord. Chem. Rev.* **2020**, *414*, 213300

b) G. Ghosh, T. Ghosh, G. Fernández, *ChemPlusChem*, **2020**, *85*, 1022–1033.

[12] a) M. L. Saha, X. Yan, P. J. Stang, *Acc. Chem. Res.* **2016**, *49*, 2527–2539;

b) W. B. Connick, R. E. Marsh, W. P. Schaefer, H. B. Gray, *Inorg. Chem.* **1997**, *36*, 913–922.

[13] K. Uemura, *Dalton Trans.* **2017**, *46*, 5474–5492.

[14] D. L. Phillips, C.-M. Che, K. H. Leung, Z. Mao, M.-C. Tse, *Coord. Chem. Rev.* **2005**, *249*, 1476–1490.

[15] C.-M. Che, S.-W. Lai, *Coord. Chem. Rev.* **2005**, *249*, 1296–1309.

[16] V. W.-W. Yam, V. K.-M. Au, S. Y.-L. Leung, *Chem. Rev.* **2015**, *115*, 7589–7728.

[17] L. M. C. Luong, M. A. Malwitz, V. Moshayedi, M. M. Olmstead, A. L. Balch, *J. Am. Chem. Soc.* **2020**, *142*, 5689–5701.

[18] A. G. Williams, In Photochemistry and Photophysics of Coordination Compounds II, Springer, Berlin, **2007**; Vol. 281, pp 205-268.

[19] C. Wakasugi, M. Yoshida, W. M. C. Sameera, Y. Shigeta, A. Kobayashi, M. Kato, *Chem. Eur. J.* **2020**, *26*, 5449–5458.

[20] T. Ogawa, M. Yoshida, H. Ohara, A. Kobayashi, M. Kato, *Chem. Commun.* **2015**, *51*, 13377–13380.

[21] H. Leopold, M. Tenne, A. Tronnier, S. Metz, I. Münster, G. Wagenblast, T. Strassner, *Angew. Chem. Int. Ed.* **2016**, *55*, 15779–15782.

[22] C.-S. S. Lee, S. Sabiah, J.-C. C. Wang, W.-S. S. Hwang, I. J. B. B. Lin, *Organometallics* **2010**, *29*, 286–289.

[23] C.-W. Hsu, K. T. Ly, W.-K. Lee, C.-C. Wu, L.-C. Wu, J.-J. Lee, T.-C. Lin, S.-H. Liu, P.-T. Chou, G.-H. Lee, Y. Chi, *ACS Appl. Mater. Interfaces* **2016**, *8*, 33888–33898.

[24] T. Ogawa, W. M. C. C. Sameera, M. Yoshida, A. Kobayashi, M. Kato, *Dalton Trans.* **2018**, *47*, 5589–5594.

[25] J.-H. Lee, C.-H. Chen, P.-H. Lee, H.-Y. Lin, M. Leung, T.-L. Chiu, C.-F. Lin, *J. Mater. Chem. C* **2019**, *7*, 5874–5888.

[26] Y. Im, S. Y. Byun, J. H. Kim, D. R. Lee, C. S. Oh, K. S. Yook, J. Y. Lee, *Adv. Funct. Mater.* **2017**, *27*, 1603007.

[27] A. Bossi, A. F. Rausch, M. J. Leitl, R. Czerwieniec, M. T. Whited, P. I. Djurovich, H. Yersin, M. E. Thompson, *Inorg. Chem.* **2013**, *52*, 12403–12415.

[28] a) M. A. Baldo, S. Lamansky, P. E. Burrows, M. E. Thompson, S. R. Forrest, *Appl. Phys. Lett.* **1999**, *75*, 4–6;

b) Y. Wu, X. Tan, A. Lv, F. Yu, H. Ma, K. Shen, Z. Sun, F. Chen, Z. K. Chen, X. C. Hang, *J. Phys. Chem. Lett.* **2019**, *10*, 5105–5110.

[29] C. L. Exstrom, J. R. J. Sowa, C. A. Daws, D. Janzen, K. R. Mann, G. A. Moore, F. F. Stewart, *Chem. Mater.* **1995**, *7*, 15–17.

[30] M. Kato, Y. Shishido, Y. Ishida, S. Kishi, *Chem. Lett.* **2008**, *37*, 16–17.

[31] S. Carrara, A. Aliprandi, C. F. Hogan, L. De Cola, *J. Am. Chem. Soc.* **2017**, *139*, 14605–14610.

[32] A. Avshu, A, Parkins, *J. Chem. Res.* **1984**, 2201–2212.

[33] R.-T. Zhuang, W.-J.Lin, R. R. Zhuang,; W.-S. Hwang, *Polyhedron* **2013**, 51, 132–141.

[34] D. Meyer, T. Strassner,. *J. Org. Chem.* **2011**, 76, 305–308.

[35) S. Gründemann, M. Albrecht, A. Kovacevic, J. W. Faller, R. H. Crabtree, *Dalton Trans.* **2002**, 2163–2167.

[36] M. Nirmala, P. Viswanathamurthi, *Chem. Sci.* **2016**, 128, 1725–1735.

[37]a) W. R. Dawson, M. W. Windsor, *J. Phys. Chem.* **1968**, 72, 3251−3260.

b) W. H. Melhuish, *J. Phys. Chem.* **1961**, 65, 229−235

[38] CrysAlisPro, version 1.171.40.67a. Rigaku Corporation, Oxford, UK, 2018

[39] a) G. M. Sheldrick, *Acta Crystallogr. Sect. A* **2015**, 71, 3–8.

b) G. M. Sheldrick, *Acta Crystallogr. Sect. C* **2015**, 71, 3–8.

[40] O. V. Dolomanov, L. J. Bourhis, R. J. Gildea, J. A. K. Howard, *J. Appl. Crystallogr.* **2009**, 42, 339–341

[41] Gaussian 16, Revision C.01, M. J. Frisch, G. W. Trucks, H. B. Schlegel, G. E. Scuseria, M. A. Robb, J. R. Cheeseman, G. Scalmani, V. Barone, G. A. Petersson, H. Nakatsuji, X. Li, M. Caricato, A. V.

Marenich, J. Bloino, B. G. Janesko, R. Gomperts, B. Mennucci, H. P. Hratchian, J. V. Ortiz, A. F. Izmaylov, J. L. Sonnenberg, D. Williams-Young, F. Ding, F. Lipparini, F. Egidi, J. Goings, B. Peng, A. Petrone, T. Henderson, D. Ranasinghe, V. G. Zakrzewski, J. Gao, N. Rega, G. Zheng, W. Liang, M. Hada, M. Ehara, K. Toyota, R. Fukuda, J. Hasegawa, M. Ishida, T. Nakajima, Y. Honda, O. Kitao, H. Nakai, T. Vreven, K. Throssell, J. A. Montgomery, Jr., J. E. Peralta, F. Ogliaro, M. J. Bearpark, J. J. Heyd, E. N. Brothers, K. N. Kudin, V. N. Staroverov, T. A. Keith, R. Kobayashi, J. Normand, K. Raghavachari, A. P. Rendell, J. C. Burant, S. S. Iyengar, J. Tomasi, M. Cossi, J. M. Millam, M. Klene, C. Adamo, R. Cammi, J. W. Ochterski, R. L. Martin, K. Morokuma, O. Farkas, J. B. Foresman, and D. J. Fox, Gaussian, Inc., Wallingford CT, 2016.

[42] Y. Zhao, D. G. Truhlar, *Theor. Chem. Acc.* **2008**, 120, 215–241.

[43] D. Andrae, U. Häussermann, M. Dolg, H. Stoll, H. Preuss, *Theor. Chim. Acta* **1990**, 77, 123–141.

[44] R. Krishnan, J. S. Binkley, R. Seeger, J. A. Pople, *J. Chem. Phys.*, **1980**, 72, 650– 654.

[45] A. Bondi, *J. Phys. Chem.* **1964**, *68*, 441–451.

[46] G. Gliemann, H. Yersin, *Struct. Bond.*, Springer, Berlin, **1985**, 62, 87–153.

[47] P. Day, *J. Am. Chem. Soc.* **1975**, *97*, 1588–1589.

[48] W. B. Connick, L. M. Henling, R. E. Marsh, H. B. Gray, *Inorg. Chem.* **1996**, *35*, 6261–6265.

[49] M. Kato, C. Kosuge, K. Morii, J. S. Ahn, H. Kitagawa, T. Mitani, M. Matsushita, T. Kato, S. Yano, M. Kimura, *Inorg. Chem.* **1999**, *38*, 1638–1641.

[50] M. Kato, A. Omura, A. Toshikawa, S. Kishi, Y. Sugimoto, *Angew. Chemie. Int. Ed.* **2002**, *41*, 3183–3185.

[51] M. Yoshida, M. Kato, *Coord. Chem. Rev.* **2018**, *355*, 101–115.

[52] M. Nakagaki, S. Aono, M. Kato, S. Sakaki, *J. phys. Chem. C* **2020**, *124*, 10453–10461.

[53] T. Sajoto, P. I. Djurovich, A. B. Tamayo, J. Oxgaard, W. A. Goddard, M. E. Thompson, *J. Am. Chem. Soc.* **2009**, *131*, 9813–9822.

[54] H. Yersin, A. F. Rausch, R. Czerwieniec, T. Hofbeck, T. Fischer, *Coord. Chem. Rev.* **2011**, *255*, 2622–2652.

[55] T. Ogawa, W. M. C. Sameera, D. Saito, M. Yoshida, A. Kobayashi, M. Kato, *Inorg. Chem.* **2018**, *57*, 14086–14096.

[56] J. C. Deaton, A. Chakraborty, R. Czerwieniec, H. Yersin, F. N. Castellano, *Phys. Chem. Chem. Phys*. **2018**, 25096–25104

Chapter 3

Vapor-induced single-crystal-to-single-crystal transformation of a highly luminescent Pt(II) complex

3.1 Introduction

In various solid-state reactions of organic and metal complex crystals, a single-crystal-to-single-crystal (SCSC) transformation is an important phenomenon because it provides detailed structural information about the reaction processes that can be useful for specific reactions.[1] Many reviews and feature articles regarding the SCSC transformation have been published from various viewpoints.[2—11] Generally, minimal structural changes during the reactions could easily promote the SCSC transformation.[2, 3] For example, photochromic reactions derived by the cyclization of some diarylethenes proceed through the SCSC transformation.[4] Further, [2+2] cycloadditions of unsaturated organic compounds can occur in the solid state through the SCSC transformation when the two molecules are fixed in a specific configuration in the crystals.[5, 6] In reaction systems that involve the insertion and liberation of molecules, the maintenance of crystallinity is considerably complex.[7] To address this problem, porous materials such as metal–organic frameworks (MOFs),[8-11] and some supramolecular arrangements of molecular crystals with hydrogen-bonded organic frameworks (HOFs)[12] are advantageous because they can maintain the crystal lattice structure during reactions. Other materials including layer and clathrate compounds also undergo the SCSC transformation.[2, 13] However, a reversible SCSC transformation, followed by the absorption and desorption of molecules have been found only in limited systems.[14-17] Meanwhile, annealing processes conducted in a vapor atmosphere are found to improve the ordering in assembled structures of polymer systems and inorganic crystals.[18-20] In this context, elucidating the dynamic process of SCSC transformations in vapor-responsive molecular crystals is a challenging yet significant subject for the emergence of functions in highly ordered systems.[21]

Square-planar Pt(II) complexes are good targets because they sensitively exhibit characteristic assembly-induced luminescence in response to crystal phases.[22, 23] The nonbonded intermolecular interactions between Pt···Pt contacts enable the emergence of intense luminescence even if the complex unit is nonemissive. In addition, highly emissive Pt(II) complexes that have been developed recently mainly for organic light-emitting devices and probes for biosystems [24] would be useful for expanding the diversity of luminescence properties. Notably, the assembly-induced luminescence can change color in response to external stimuli such as temperature, mechanical force, and chemical vapor, reflecting the scope for sensitive changes in the Pt···Pt electronic interactions.[25-27] In-depth investigations regarding temperature and pressure dependency of luminescence have been conducted for several one-dimensional Pt(II) complex systems.[28] However, most of the investigated systems include [Pt$_2$(bpy)$_2$(pyt)$_2$](PF$_6$)$_2$ (bpy=2,2'-bipyridine, pyt=pyridine-2-thiolate).[26, 30] The acetonitrile-solvated form transformed to a red luminescent, unsolvated form under a nitrogen gas stream at 273 K, while retaining its single crystallinity. However, the reverse transformation (i. e., uptake of vapor molecules) induced the deterioration of single crystallinity to the polycrystalline state. It is worth noting that some Au(I) complexes with metal–metal interactions exhibit reversible SCSC transformations, followed by luminescence color changes.[15, 31] The SCSC transformation may occur more easily for systems that show softer metal–metal interactions.

Herein, this chapter the reversible SCSC transformation of a luminescent Pt(II)-*N*-heterocyclic carbene

complex, [Pt(CN)$_2$(^{t}Bu-impy)] (^{t}Bu-impy=1-tert-butyl-3-(2-pyridyl)-1H-imidazol-2-ylidene; **Pt-^{t}Bu**; Figure 1) were detailed investigation . The trihydrate crystal of the complex exhibited highly efficient blue photoluminescence (λ_{max}=484 nm) with an emission quantum yield of 0.70 in the solid state at 298 K.[32] The blue luminescence corresponds to the emission from the triplet metal–metal-to-ligand charge transfer (3MMLCT) state, which originates from the weak Pt· · · Pt electronic interactions in the stacking structure of the crystal. This motivated us to further investigate the structural transformations of the system. In this study, the trihydrate crystal of the complex (**Pt-^{t}Bu** ·3 H$_2$O) transforms to the anhydrous form (**Pt-^{t}Bu** ·dry), while maintaining its single crystallinity and concomitantly exhibiting a distinct luminescence color change from blue to yellowish green. The dynamics of this structural change by the continuous tracking of single-crystal X-ray diffraction in a vapor atmosphere was revealed. Based on this, the SCSC transformation occurred reversibly in two steps was revealed. In addition, a contrasting vapor response in which **Pt-^{t}Bu** ·dry easily responded to MeOH vapor, but did not respond to EtOH vapor at all were observed.
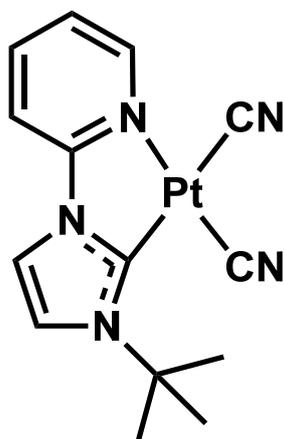

Figure 1. Molecular structure of **Pt-^{t}Bu**

3.2 Experimental

3.2.1 Materials

Pt(II) complex **Pt-^{t}Bu** was prepared as chapter 2.

3.2.2 Photophysical measurements.

Luminescence spectra were recorded using a JASCO FP-8600 spectrofluorometer at room temperature. Slit widths of excitation and emission light were 5 nm. Variable temperature luminescence spectra were measured with a Hamamatsu Photonics multichannel photodetector (PMA-11) and nitrogen laser (Usho KEN-X) for excitation at 337 nm. Absolute luminescent quantum yields were recorded on a Hamamatsu Photonics C9920-02 absolute photoluminescence quantum yield measurement system equipped with an integrating sphere apparatus and a 150 W CW xenon light source. A Hamamatsu Photonics A10095-3 non-luminescent quartz sample holder was used for absolute photoluminescence quantum yield measurements. The accuracy of the instrument was confirmed by measuring the quantum yield of anthracene in ethanol solution (Φ = 0.27).[40,41] Emission lifetime measurements and time-resolved emission spectra were recorded using a Hamamatsu Photonics C4780 system equipped with a streak camera (Hamamatsu Photonics C4334) as a photodetector and a nitrogen laser for excitation at 337 nm. The emission decays were analyzed using two exponentials; I = A$_1$exp($-t/\tau_1$) + A$_2$exp($-t/\tau_2$), where Ai denotes the pre-exponential factors for lifetimes τi.

3.2.3 Single-crystal X-ray diffraction measurements

Single-crystal X-ray diffraction measurements were performed using (1) a Rigaku AFC-8 diffractometer equipped with a mercury CCD area detector and graphite monochromated Mo-Kα radiation (λ = 0.71069 Å) or a Rigaku XtaLAB Synergy-S diffractometer equipped with HyPix6000HE hybrid photon counting detector and multilayer mirror-monochromated Cu Kα radiation (λ = 1.54184 Å) and a micro-focus sealed X-ray tube generator, or (2) Spring-8 synchrotron facility with beamline BL02B1 (λ = 0.24882 Å) and Dectris Pilatus3 X CdTe 1M detector for in-situ continuous measurements. Single crystals measured by (1) were mounted on a glass fiber using an epoxy resin. These single crystals were cooled by using a N$_2$-flow type temperature controller. Diffraction data were collected using CrystalClear [42] or CrysAlisPro [43] software followed by the data processing using CrysAlisPro. Crystals measured by (2) were mounted on gas and vapor adsorption/desorption system in a glass capillary. Diffraction data were collected using RapidAuto and data processing was done with CrysAlisPro. The data collections were performed using a single crystal of **Pt-^{t}Bu**·3H$_2$O in each consecutive step: the initial state, after evacuating water, and after water vapor introduction at 3 kPa and at 100 kPa. The data collection for the adsorption process was repeated at the time after exposure of < 1 min, 2 h, 5 h, 8 h, 11 h, 14 h, 17 h, and 20 h.

All the structures in (1) were solved with the intrinsic phasing method using SHELXT-2014 [44] or SHELXS-2013.[45] Structural refinements were conducted by the full-matrix least-squares method using SHELXL-2017.[46] Non-hydrogen atoms were refined anisotropically and all hydrogen atoms were

refined using the riding model. Calculations were performed using the Olex2 software [47] or Mercury software. [48].

3.2.4 Other measurements.

Vapor-adsorption isotherms were measured using an automatic volumetric adsorption apparatus, MicroBel BELSORP-MAX at 298 K. All samples were dried under vacuum for 12 h to remove the hydrated water molecules prior to each measurement. TG-DTA analysis was performed using a Rigaku Thermo Evo TG-8120 analyzer. The typical sample mass used for the analysis was 1 mg and the heating rate was 1 K min^{-1}. Powder X-ray diffraction (PXRD) measurements were conducted using CuKα radiation (λ =1.5418 Å) on a Bruker D8 Advance diffractometer equipped with a graphite monochromator and a one-dimensional LynxEye detector.

3.2.5 Computational methods.

Density functional theory (DFT) were conducted using the Gaussian 16 (revision C.01) program [49] The M06 functional [50] was used for single point energy calculations. The SDD basis set and associated effective core potentials were used for Pt [51] and the 6-311+G(d, p) basis sets were used for other atoms.[52] Structure of tetrameric unit were taken from the single-crystal X-ray data without optimization.

3.3 Results and discussion

3.3.1 Vapochromic luminescence

Colorless needles of the blue luminescent trihydrate complex (**Pt-^{t}Bu**$\cdot$3 H$_2$O) were obtained by the crystallization from an aqueous DMF solution, which were stable under a water vapor atmosphere, or in a sealed vessel. [32] However, when the crystalline sample of **Pt-^{t}Bu**$\cdot$3 H$_2$O was dried in vacuo, it turned pale yellow, and the emission color changed from blue to yellowish-green (Figure 2a). The dried sample was characterized by thermogravimetric and differential thermal analysis (TG-DTA; Figure 2) and X-ray diffraction measurements (see below) and found to exist in its anhydrous form with the decomposition temperature of 260 °C (**Pt-^{t}Bu** $\cdot$ dry). Emission and excitation spectra are shown in Figures 3 and 4, respectively. The photophysical data of different forms of 1 are summarized in Table 1. **Pt-^{t}Bu**$\cdot$3 H$_2$O is the first example of a Pt(II) complex that exhibits blue ^{3}MMLCT emission on the basis of the detailed investigation of its characteristic absorption and emission properties in the crystal state as well as through crystal structural analyses.[32] The similarity in the emission lifetime and quantum yield for the desorbed form, **Pt-^{t}Bu**$\cdot$dry, suggests that this emission also originated from the ^{3}MMLCT state, and the red-shift of the emission spectrum of the sample after drying (Figure 2b) implies stronger Pt$\cdot\cdot$ $\cdot$ Pt interactions in **Pt-^{t}Bu** $\cdot$ dry. Density functional theory (DFT) calculations support sensitive changes in the HOMO and LUMO energy levels (Figure 5). Upon exposure of **Pt-^{t}Bu**$\cdot$ dry to water vapor, the blue emission recovered successfully. However, the spectral profile suggested that there is a stepwise vapor-uptake process (Figure 2b, yellow line) and the recovery to the initial trihydrate form was incomplete under the measurement conditions in air (Figure 2b, green line).

Interestingly, when **Pt-^{t}Bu**$\cdot$dry was exposed to MeOH vapor, the blue luminescence color recovered and the luminescence spectrum was nearly equivalent to that of the original trihydrate form, thus suggesting that a similar structure was formed with MeOH vapor (Figure 2c, red line). However, upon exposure to EtOH vapor, the yellowish-green luminescence color of the anhydrous form did not change even after 24 h under saturated vapor pressure (Figure 2c, black line).
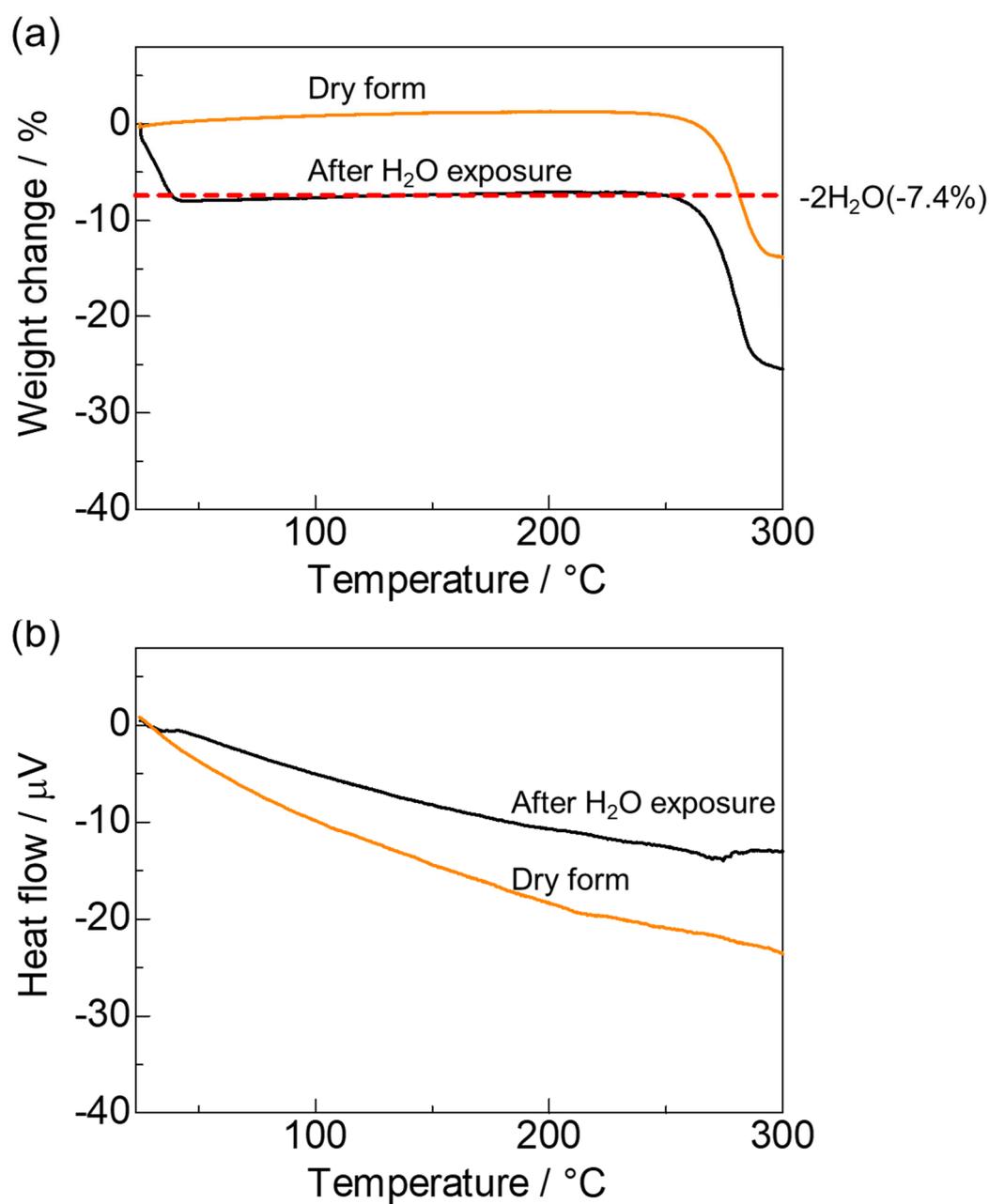
Figure 2. (a) Thermogravimetric and (b) differential thermal analysis (TG-DTA) of **Pt-^{t}Bu**. The sample was found to be the dry (anhydrous) form in the measurement conditions under Ar flow (0.3 L/min) (orange lines). Then the measurement was also carried out in the conditions without Ar flow for the sample after water vapor exposure for 20 min (black lines).
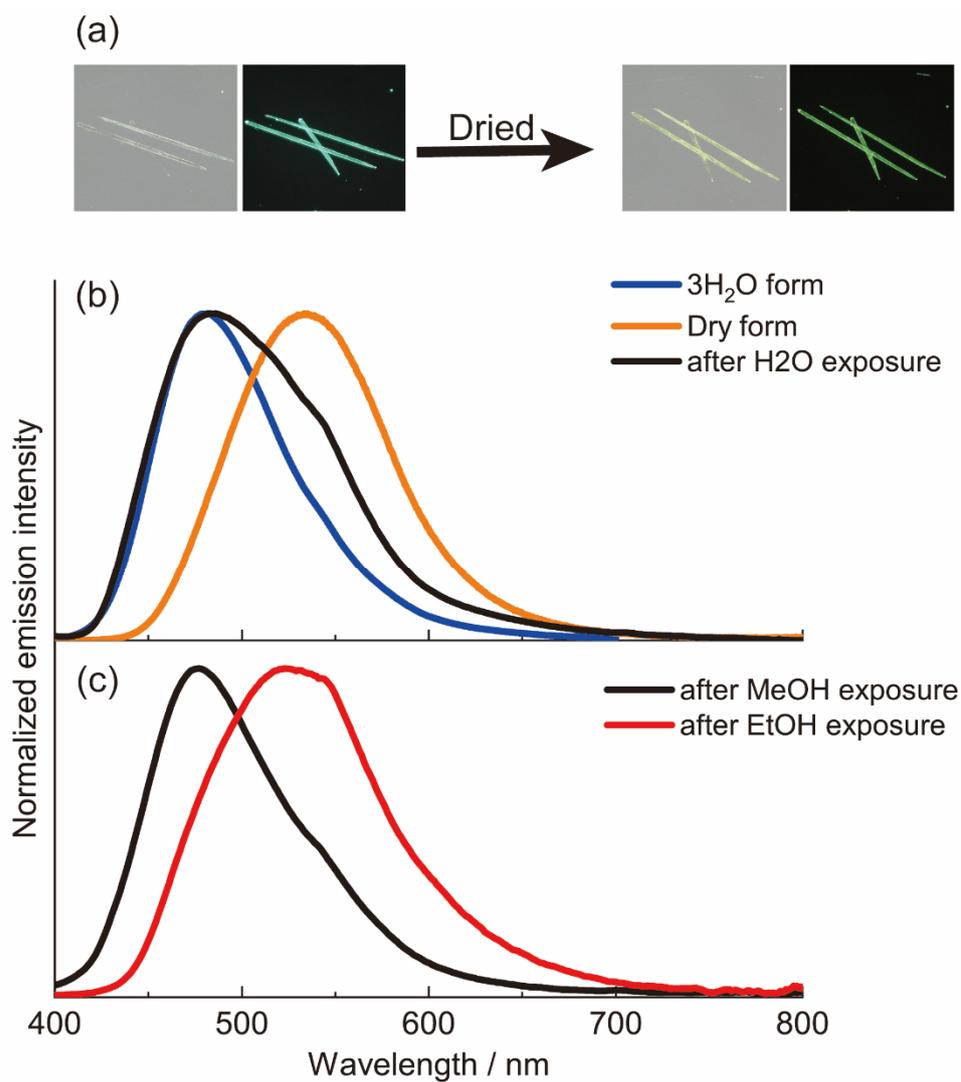
Figure 3. (a) Photos of the crystals of the initial trihydrate **Pt-^{t}Bu**·3H$_2$O complex before and after drying, bright field (left) and under UV light (right), (b) Changes in the emission spectra of **Pt-^{t}Bu**·3H$_2$O at 293 K (λ_{ex} = 350 nm): blue, initial trihydrate; orange, after drying; black, after water vapor exposure of the dried form, (c) black and red, after MeOH and EtOH vapor exposure of the dried form, respectively.
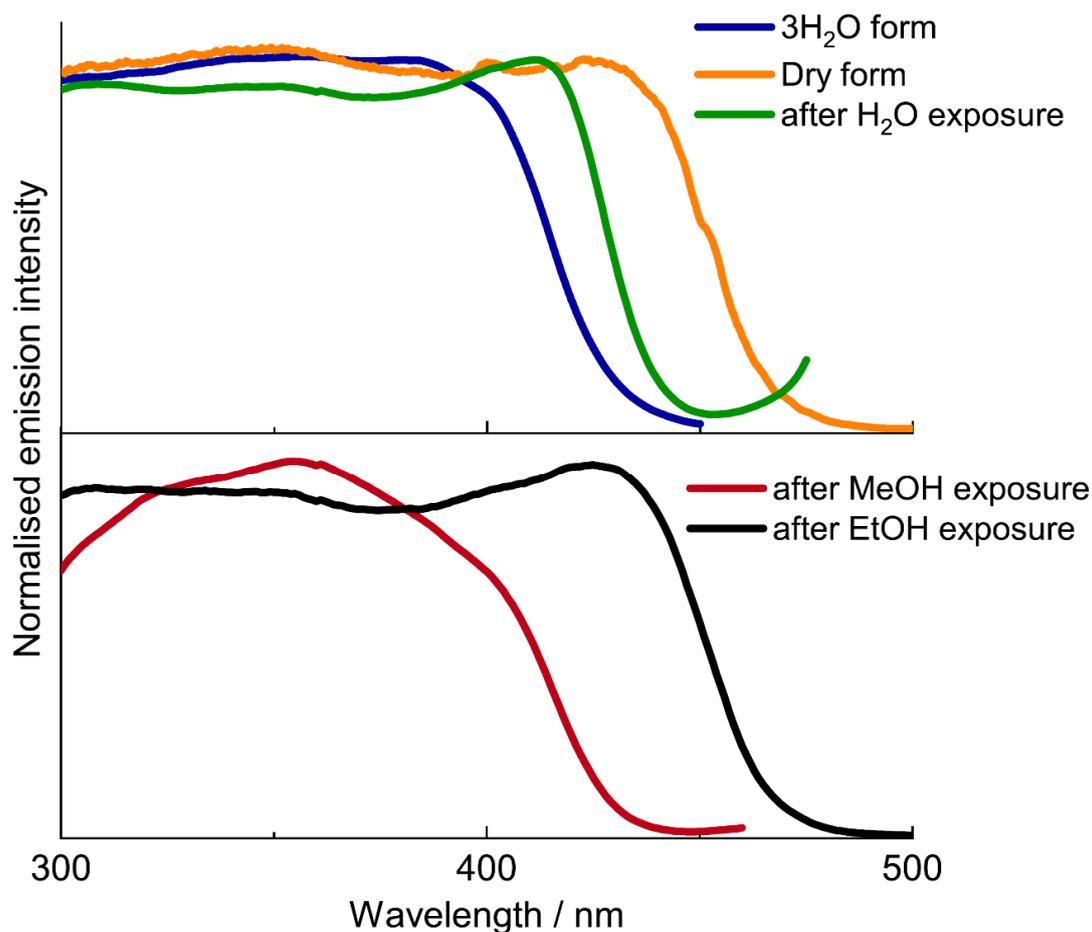
Figure 4. Changes in excitation spectra of **Pt-^{t}Bu**·3H$_2$O at 293 K: blue, non-treated trihydrate; orange, after drying; green, after water vapor exposure of the dried form, red and black, after MeOH and EtOH vapor exposure of the dried form, respectively.

Table 1. Photophysical data of the three forms of [Pt(CN)$_2$(^{t}Bu-impy)] (**Pt-^{t}Bu**) in the solid state at 298 K.

	$\lambda_{max}{}^a$ /nm	Φ^b	τ^c / μs (A^d)	$\tau_{av}{}^e$ / μs	$k_r{}^f$ / s^{-1}	$k_{nr}{}^g$ / s^{-1}
Pt-^{t}Bu·3H$_2$O	484	0.70	0.55 (0.72), 1.25 (0.28)	0.88	8.0×10^5	3.4×10^5
Pt-^{t}Bu·dry	533	0.61	0.31(0.77), 0.82(0.23)	0.53	11.5×10^5	7.4×10^5
Pt-^{t}Bu·MeOH	477	0.57	0.50	-	11.4×10^5	8.6×10^5

^{a} Emission maximum. ^{b} Photoluminescence quantum yields. ^{c} Emission lifetime. ^{d} Pre-exponential factors. ^{e} Average emission lifetimes were determined from the equation $\tau_{av} = \Sigma A_i\tau_i^2 / \Sigma A_i\tau_i$ ($i = 1, 2$). ^{f} Radiative rate constants (k_r) were estimated from the equation $k_r = \Phi/\tau_{av}$. ^{g} Non-radiative rate constants (k_{nr}) were estimated from the equation $k_{nr} = k_r(1 - \Phi)/\Phi$.

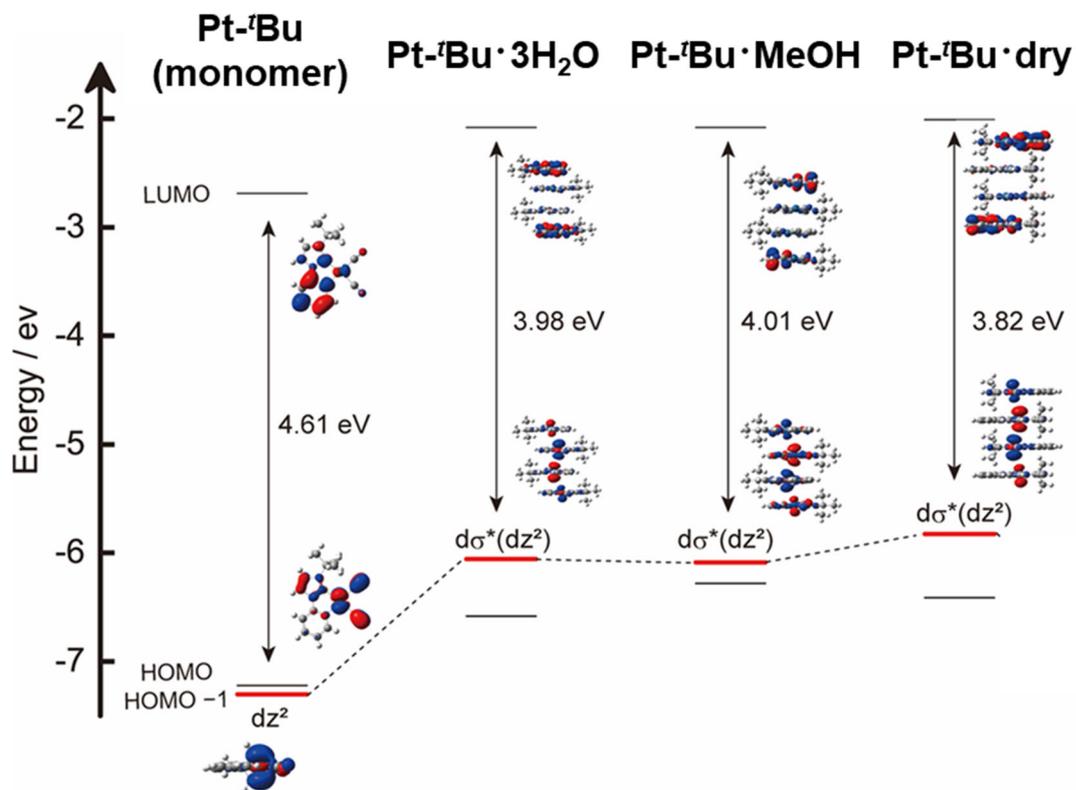**Figure 5.** Energy level diagram of the Pt(II) complex (**Pt-^{t}Bu**) and the tetramers in the three crystal forms, **Pt-^{t}Bu**·3H$_2$O, **Pt-^{t}Bu**·CH$_3$OH, and anhydrous form **Pt-^{t}Bu**·dry. The atomic coordinates were used those obtained from the X-ray analyses for the single point energy calculations based on the density functional theory (DFT) (M06/SDD for Pt, 6-311+G(d,p) for other atoms).

Further, the vapor adsorption behavior for **Pt-ᵗBu** · dry was investigated by vapor adsorption isotherm measurements (Figure 6), which clearly exhibited a selective uptake of water and MeOH to EtOH. MeOH vapor adsorption occurred at a relative pressure of around 0.6, indicating that 1 mol of MeOH was adsorbed per mol of the complex, showing a typical gate-open type adsorption behavior.[33] On the other hand, no adsorption occurred even at the saturated vapor pressure for EtOH. Such discriminative vapor adsorption behavior of MeOH over EtOH has been previously observed for a Ni(II)–quinonoid complex that forms a hydrogen-bonded one-dimensional structure.[34] Considering the differences in the saturated vapor pressure (H_2O: 3.2 kPa, MeOH: 16.9 kPa, EtOH: 7.8 kPa at 298 K),[35] molecular size ($H2O$: ~40 Å^3, MeOH: ~60 Å^3, EtOH: ~90 Å^3),36 and hydrogen-bonding ability ($H2O$ > MeOH > EtOH), the advantageous uptake of MeOH vapor by **Pt-ᵗBu** ·dry can be explained. As for water vapor, very slow adsorption occurred,d although the vapor pressure at 298 K was lower than that of the others. Moreover, the water vapor adsorption isotherm at 298 K (Figure 6) indicates that less than two water molecules per Pt(II) complex were taken up, even at the saturated vapor pressure. This suggests the existence of a dihydrate form (**Pt-ᵗBu** ·$2H_2O$) and that a higher vapor pressure is necessary to revert completely to the trihydrate form (**Pt-ᵗBu** ·$3 H_2O$). It is consistent with the results of the TG-DTA analysis that indicated the weight decrease of two water molecules per complex and heat absorption for the sample after water vapor exposure in the range of 25–43 °C (Figure 2). In fact, through in-situ single-crystal X-ray diffraction analysis, vapor-induced reversible and stepwise SCSC transformations were observed(see below).
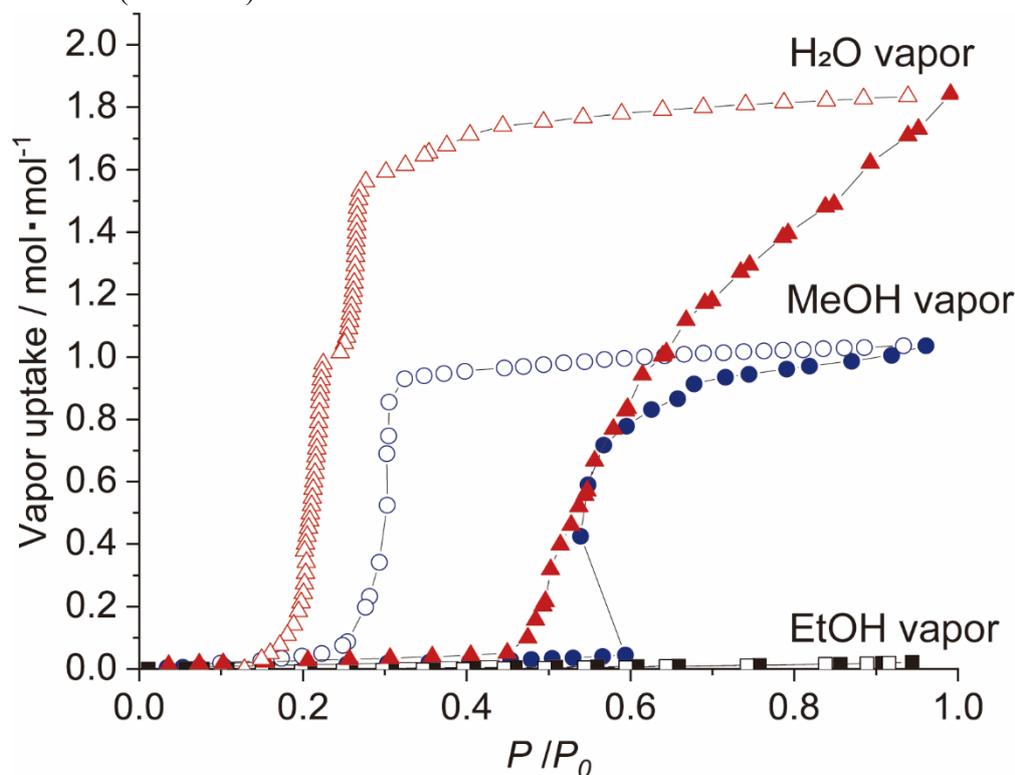

Figure 6. Water (–▲–△–), methanol (–●–○–) and ethanol (–■–□–) vapor adsorption isotherms of the desorbed form **Pt-ᵗBu**·dry at 298 K. Closed and open symbols show the adsorption and desorption processes, respectively.

3.3.2 Temperature-dependent SCSC vapor desorption

To gain insight into the vapochromic behavior, variable-temperature single-crystal X-ray diffraction analysis using **Pt-^{t}Bu**·3 H_2O under a dry nitrogen gas flow was conducted. Diffraction data at each point in the cycle of 100 K→325 K→100 K (Table 2) were successfully obtained. Figure 7a shows photographs of the crystals that changed color during the cycle. At 250 K, the colorless crystal became yellowish. Indeed, phase transitions from space group $P2_1/c$ to $C2/m$ before and after the temperature reached 250 K were observed. It is worth noting that the cell volume changed drastically owing to the phase transition (~360 Å^3 at 100 K), as shown in Figure 7b. It was estimated that 12 water molecules were lost from the unit cell, or three water molecules were lost per complex molecule. In addition, there was no void space accessible to the water molecules in the $C2/m$ crystal.[37] These results clearly indicate that the SCSC structural transformation was driven by the release of solvated water molecules. Further, the **Pt-^{t}Bu** · dry form (space group $C2/m$) was maintained at low temperatures as depicted in Figure 4b, indicating that the transformation is not temperature-induced, but rather triggered by the loss of water molecules. The changes in cell parameters due to the phase transition (Figures 7c) provide useful information about the characteristics of this assembled Pt(II) complex system.
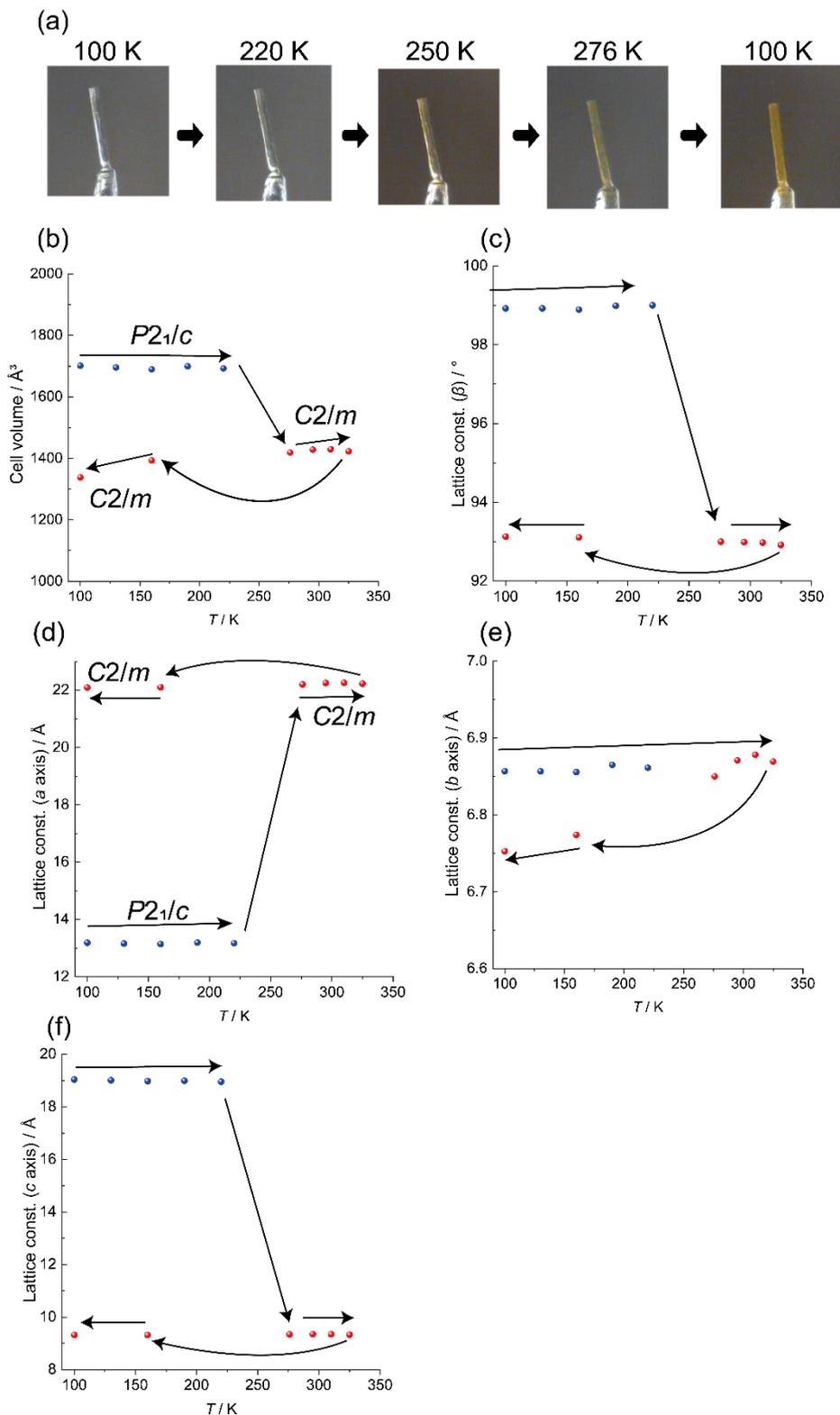
Figure7. Changes in the (a) crystal color, . Changes in the lattice parameters of Pt-tBu·3H2O in the temperature cycle of 100 K → 325 K → 100 K: (b) the cell volume, (c) the angle *β*, (d) the length of the *a* axis, (e) the length of the *b* axis, and (f) the length of the *c* axis

Table 2. Crystal data for **Pt-^{t}Bu·3H$_2$O** in the temperature cycle of 100 K → 325 K → 100 K.

T / K	100	130	160	190	220	276
Formula	C$_{14}$H$_{15}$N$_5$Pt·3H$_2$O	C$_{14}$H$_{15}$N$_5$Pt·3H$_2$O	C$_{14}$H$_{15}$N$_5$Pt·3H$_2$O	C$_{14}$H$_{15}$N$_5$Pt·3H$_2$O	C$_{14}$H$_{15}$N$_5$Pt·3H$_2$O	C$_{14}$H$_{15}$N$_5$Pt
Formula weight	502.45	502.45	502.45	502.45	502.45	448.40
Crystal system	monoclinic	monoclinic	monoclinic	monoclinic	monoclinic	monoclinic
Space group	$P2_1/c$	$P2_1/c$	$P2_1/c$	$P2_1/c$	$P2_1/c$	$C2/m$
a / Å	13.1909(6)	13.1663(4)	13.1449(4)	13.1958(3)	13.1763(5)	22.2046(2)
b / Å	6.8571(2)	6.8569(1)	6.8558(2)	6.8652(1)	6.8615(2)	6.8502(5)
c / Å	19.0476(7)	19.0191(5)	18.9833(6)	18.9960(5)	18.9603(6)	9.3430(6)
α / °	90	90	90	90	90	90
β / °	98.923(4)	98.925(2)	98.892(3)	98.986(2)	99.001(3)	93.005(6)
γ / °	90	90	90	90	90	90
V / Å^3	1702.0(1)	1696.26(7)	1690.19(8)	1699.76(6)	1693.5(1)	1419.2(2)
Z	4	4	4	4	4	4
D_{calc} /g cm^{-3}	1.961	1.967	1.975	1.963	1.971	2.099
$F(000)$	968.0	968.0	968.0	968.0	968.0	848.0
Reflections collected	26989	27211	26925	27630	26981	10453
Unique reflections	4782	4787	4805	4821	4859	2149
GOF on F^2	1.087	1.057	1.096	1.075	1.110	1.091
R_{int}	0.0275	0.0250	0.0249	0.0227	0.0329	0.0664
R_1[a]	0.0192	0.0178	0.0181	0.0173	0.0270	0.0529
wR_2[b] (all data)	0.0488	0.0432	0.0443	0.0403	0.0702	0.1123

(continued)

T / K	295	310	325	160	100
Formula	$C_{14}H_{15}N_5Pt$	$C_{14}H_{15}N_5Pt$	$C_{14}H_{15}N_5Pt$	$C_{14}H_{15}N_5Pt$	$C_{14}H_{15}N_5Pt$
Formula weight	448.40	448.40	448.40	448.40	448.40
Crystal system	monoclinic	monoclinic	monoclinic	monoclinic	monoclinic
Space group	$C2/m$	$C2/m$	$C2/m$	$C2/m$	$C2/m$
a / Å	22.256(2)	22.261(2)	22.231(2)	22.1038(1)	22.094(1)
b / Å	6.8711(4)	6.8785(4)	6.8697(4)	6.7743(4)	6.7527(3)
c / Å	9.3540(5)	9.3507(4)	9.3311(5)	9.3188(5)	9.3230(5)
α / °	90	90	90	90	90
β / °	92.992(5)	92.981(6)	92.922(6)	93.113(5)	93.131(5)
γ / °	90	90	90	90	90
V / Å^3	1428.5(2)	1429.9(2)	1423.2(2)	1393.3(1)	1388.9(1)
Z	4	4	4	4	4
D_{calc} /g cm^{-3}	2.085	2.083	2.093	2.138	2.144
$F(000)$	848.0	848.0	848.0	848.0	848.0
Reflections collected	10914	10984	10987	10189	10289
Unique reflections	2156	2161	2178	2122	2104
GOF on F^2	1.069	1.094	1.057	1.037	1.136
R_{int}	0.0423	0.0446	0.0446	0.0430	0.0444
R_1 [a]	0.0470	0.0474	0.0508	0.0455	0.0428
wR_2 [b] (all data)	0.0951	0.0977	0.1042	0.1283	0.0977

[a] $R_1 = \Sigma||F_o|-|F_c|| /\Sigma|F_o|$. [b] $wR_2 = [\Sigma w(F_o^2 - F_c^2)/ \Sigma w(F_o)^2]^{1/2}$, $w = [\sigma_c^2(F_o^2) + (xP)^2 + yP]^{-1}$, $P = (F_o^2 - 2F_c^2)/3$.

Table 3. Crystal data for the anhydrous form **Pt-^{t}Bu**·dry after drying, the dihydrate and trihydrate forms after H_2O vapor exposure, and the MeOH solvated form after MeOH vapor exposure.

	Pt-^{t}Bu·dry	**Pt-^{t}Bu**·2H$_2$O (H$_2$O vapor)	**Pt-^{t}Bu**·3H$_2$O (H$_2$O vapor)	**Pt-^{t}Bu**·MeOH (MeOH vapor)
Formula	C$_{14}$H$_{15}$N$_5$Pt	C$_{14}$H$_{15}$N$_5$Pt·2H$_2$O	C$_{14}$H$_{15}$N$_5$Pt·3H$_2$O	C$_{14}$H$_{15}$N$_5$Pt·CH$_3$OH
Formula weight	448.40	484.43	502.45	480.44
Crystal system	monoclinic	monoclinic	monoclinic	monoclinic
Space group	$C2/m$	$P2_1/c$	$P2_1/c$	$P2_1/m$
a / Å	22.094(1)	24.6837(8)	13.1454(9)	9.291(1)
b / Å	6.7527(3)	6.8237(2)	6.8184(3)	6.7597(9)
c / Å	9.3230(5)	18.6968(5)	18.948(1)	12.851(2)
α / °	90	90	90	90
β / °	93.131(5)	91.330(3)	99.023(6)	95.67(2)
γ / °	90	90	90	90
V / Å^3	1388.9(1)	3148.3(2)	1677.3(2)	803.1(2)
T / K	100	150	100	100
Z	4	8	4	2
D_{calc} / g cm^{-3}	2.144	2.044	1.990	1.987
$F(000)$	848.0	1856.0	968.0	460.0
Reflections collected	10289	19822	25842	7122
Unique reflections	2104	6444	4748	1792
GOF on F^2	1.136	1.068	1.340	2.306
R_{int}	0.0444	0.0396	0.1140	0.1224
R_1[a]	0.0428	0.0768	0.1121	0.1606
wR_2[b] (all data)	0.0977	0.1841	0.2124	0.4562

[a] $R_1 = \Sigma||F_o| - |F_c||/\Sigma|F_o|$. [b] $wR_2 = [\Sigma w(F_o^2 - F_c^2)/\Sigma w(F_o^2)^2]^{1/2}$, $w = [\sigma_c^2(F_o^2) + (xP)^2 + yP]^{-1}$, $P = (F_o^2 - 2F_c^2)/3$.

Table4. Selected interatomic distances (Å) and angles (°) for **Pt-^{t}Bu**·3H$_2$O (initial), **Pt-^{t}Bu** (dry), **Pt-^{t}Bu**·3H$_2$O (H$_2$O vapor exposure), and **Pt-^{t}Bu**·MeOH (MeOH vapor exposure) at 100 K.

	Pt-^{t}Bu·3H$_2$O (initial)	**Pt-^{t}Bu** ·dry	**Pt-^{t}Bu**·3H$_2$O (H$_2$O vapor)	**Pt-^{t}Bu**·MeOH (MeOH vapor)
Pt1−C1	1.956(2)	1.96(1)	1.97(2)	1.83(5)
Pt1−C2	2.013(3)	1.976(8)	1.99(2)	1.93(6)
Pt1−N3	2.085(2)	2.077(8)	2.09(1)	2.09(3)
Pt1−C8	2.062(3)	2.055(9)	2.04(2)	2.09(3)
N1−C1	1.164(3)	1.16(1)	1.10(2)	1.30(6)
N2−C2	1.158(4)	1.16(1)	1.18(2)	1.11(8)
Pt1⋯Pt1'	3.4760(2)	3.5079(3)	3.442(2)	3.525(1)
Pt1⋯Pt1"	3.6504(2)	–	3.645(2)	–
C1−Pt1−C2	86.4(1)	85.6(4)	86.8(7)	94(2)
C1−Pt1−C8	101.0(1)	102.8(4)	100.4(7)	102(2)
C1−Pt1−N3	178.5(1)	177.7(3)	178.8(6)	178(2)
C2−Pt1−C8	172.6(1)	171.6(4)	172.6(7)	164(2)
C2−Pt1−N3	93.22(9)	92.1(3)	93.2(6)	88(2)
C8−Pt1−N3	79.45(9)	79.5(3)	79.7(6)	76(1)
Pt1'⋯Pt1⋯Pt1"	148.90(1)	148.52(3)	148.32(4)	147.1(1)

3.3.3 Vapor-induced reversible SCSC transformations: In-situ tracking
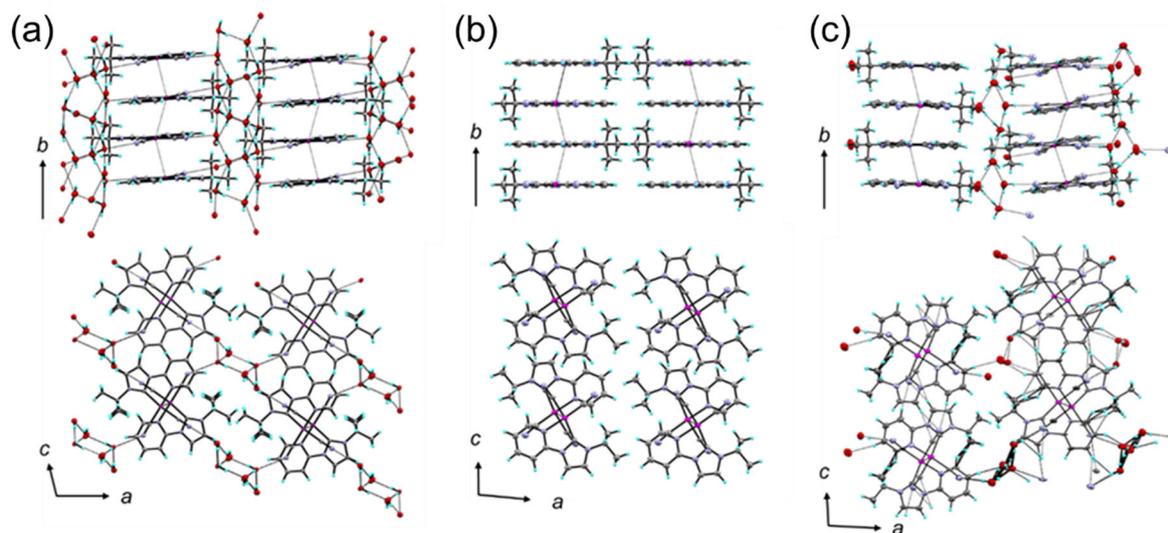
Figure 8. (a) Packing structures of **Pt-^{t}Bu**·3H$_2$O and (b) **Pt-^{t}Bu**·dry derived from **Pt-^{t}Bu**·3H$_2$O by SCSC transformation. The structures were drawn using the data at 100 K. (c) Packing structures of **Pt-^{t}Bu**·2H$_2$O obtained from **Pt-^{t}Bu**·dry by the reverse SCSC transformation at 150 K. Upper: drawings viewed along c axis, lower: drawings viewed along b axis. Color codes for atoms: magenta Pt; red O; violet N; gray C, cyan H. The hydrogen bonds and Pt···Pt contacts are indicated by black dotted lines.

As shown in Figure 8a, the crystal structure of **Pt-^{t}Bu** · 3 H$_2$O consists of Pt(II) complex columns with loose Pt· · · Pt contacts and water molecule chains formed by hydrogen bonding along the b-axis. The loss of water molecules resulted in the closure of the channels by the movement of Pt-complex columns along the a-axis. The intercolumn distances are roughly estimated based on the Pt· · · Pt distances between the nearest columns along the a-axis: 13.2 Å for **Pt-^{t}Bu** · 3 H$_2$O and 11.1 Å for **Pt-^{t}Bu** · dry at 100 K. The water molecules in **Pt-^{t}Bu** · 3 H$_2$O crystal are found to bind with the Pt(II) complex either by direct hydrogen bonding (O1 and O3; Figure 11), or without any direct hydrogen bonding (O2; Figure 11). Considering the larger thermal factor of O2 compared with the other water molecules (O1, O2, O3…), O2 could be a flexible molecule that is easily released in the open space at room temperature. Each Pt(II) complex unit adopts a typical square planar coordination geometry. For the desorbed form (**Pt-^{t}Bu**· dry), all non-hydrogen atoms, except for two of the four tert-butyl carbon atoms, are located on the crystallographic mirror plane. In contrast, for **Pt-^{t}Bu** · 3 H$_2$O, all atoms occupy independent positions, forming a slightly inclined stacking structure.[32] An equivalent Pt· · · Pt distance (3.5079(3) Å at 100 K) for **Pt-^{t}Bu** · dry is slightly shorter than the average value for **Pt-^{t}Bu** · 3 H$_2$O (3.5586(3) Å[32] at 100 K), which is reasonably consistent with the red-shift of the emission spectrum upon the release of water molecules. Such a difference between the two packing structures suggests that the molecular movement may be induced by the water release; water release creates a void volume, which enables molecular movement, and the consequent rearrangement of the columns closes the channel. Interestingly, the reverse transformation by vapor molecules also proceeded through the SCSC transformation, wherein

after the exposure of the single crystal of **Pt-^{t}Bu** · dry to water vapor for ~8 h, diffraction data indicated the recovery of the original trihydrate form, although the crystallinity was slightly lowered (Table 3). To explore the dynamic structural changes, single-crystal studies of **Pt-^{t}Bu** · 3 H_2O with an in-situ gas and vapor system[38] at room temperature (298 K) was conducted, and found that all the processes (dehydration and water reabsorption) proceeded while maintaining the single crystallinity (Figure 9). As in the case of variable temperature measurements under nitrogen flow described in the previous section, the SCSC process in the desorption cycle proceeded smoothly (**Pt-^{t}Bu** · 3 H_2O → **Pt-^{t}Bu** · dry) in vacuo at room temperature. The water molecules were not completely reabsorbed in the reverse process at the saturated vapor pressure (3 kPa), instead requiring higher pressures of 100 kPa by addition of air. At 100 kPa, the crystal structure with space group $P2_1/c$ was found immediately (at <1 min in Figure 9), and then gradual changes in the unit cell were observed by the continuous tracking, with the crystal transformation to the trihydrate form completed after 20 h (Figure 9). As a result, stepwise SCSC transformations (**Pt-^{t}Bu** · dry→ **Pt-^{t}Bu** · 2H_2O→ **Pt-^{t}Bu** · 3 H_2O) during the vapor uptake process were found. Such vapor adsorption/desorption processes were also confirmed with the bulk sample by the powder X-ray diffraction measurements (Figure 10). To investigate the intermediate dihydrate form, **Pt-^{t}Bu** · 2 H_2O, the crystal structure was determined at 150 K (Figure 5c), which revealed two forms of the Pt(II) columns, oblique and parallel stacks; just like an intermediate structure between **Pt-^{t}Bu**· dry and **Pt-^{t}Bu** · 3 H_2O. In addition, anisotropic changes were observed during the expansion process of the unit cells by water uptake. Overall, the reversible and vapochromic SCSC transformation of **Pt-^{t}Bu** is depicted in Figure 12 schematically.
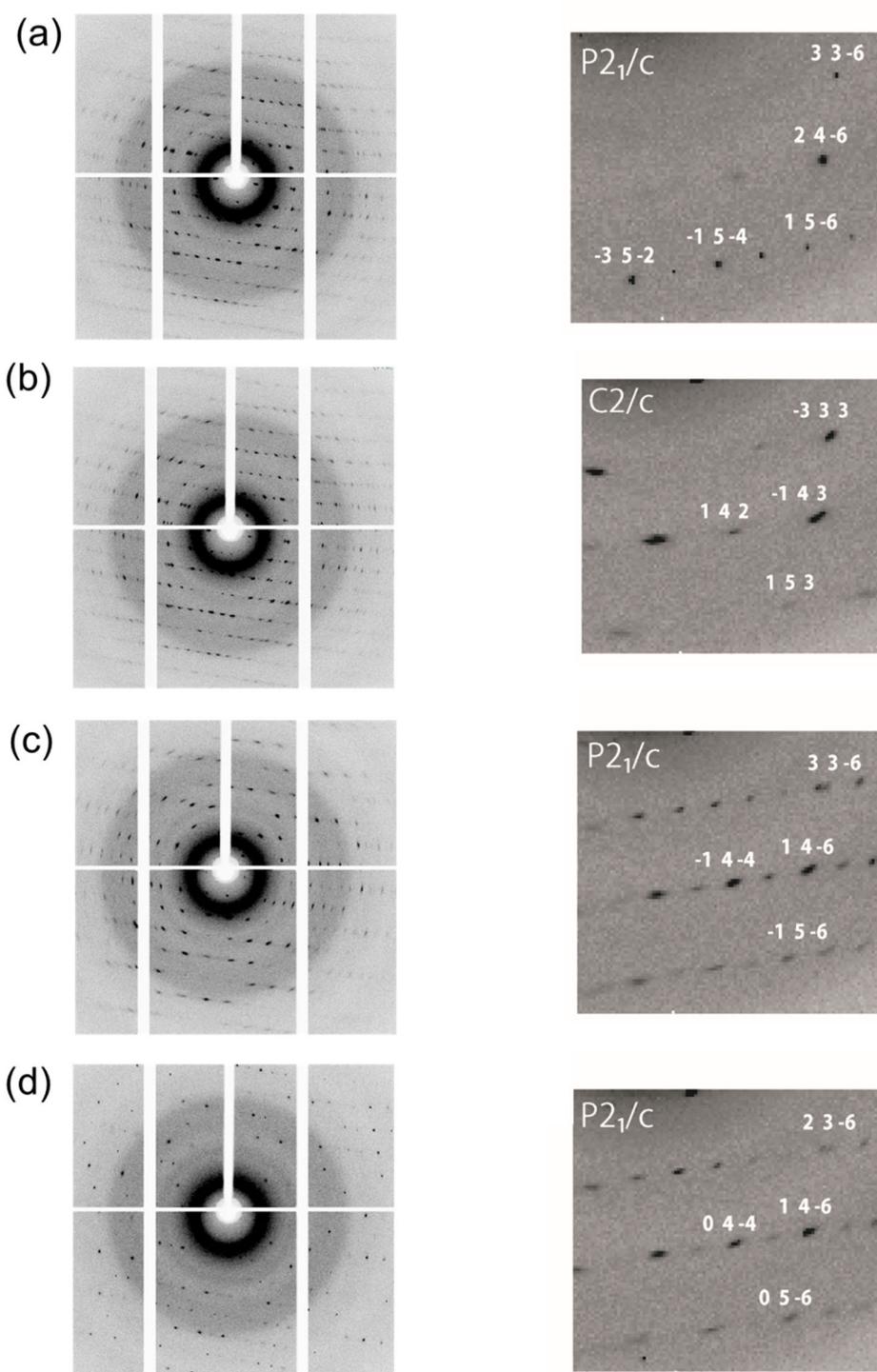
Figure 9. Diffraction images of crystal sealed in a glass capillary on the in-situ gas and vapor system at 298 K. Left, (a) the initial form **Pt-ᵗBu**·3H₂O, (b) Evacuated form **Pt-ᵗBu**·dry, (c) <1 min. under 100 kPa (d) 20 h under the recovered trihydrate form on exposure to water vapor for 8h at room temperature. Right images are the fragments of diffraction pattern for the same diffraction frame, with indexes of reflections.
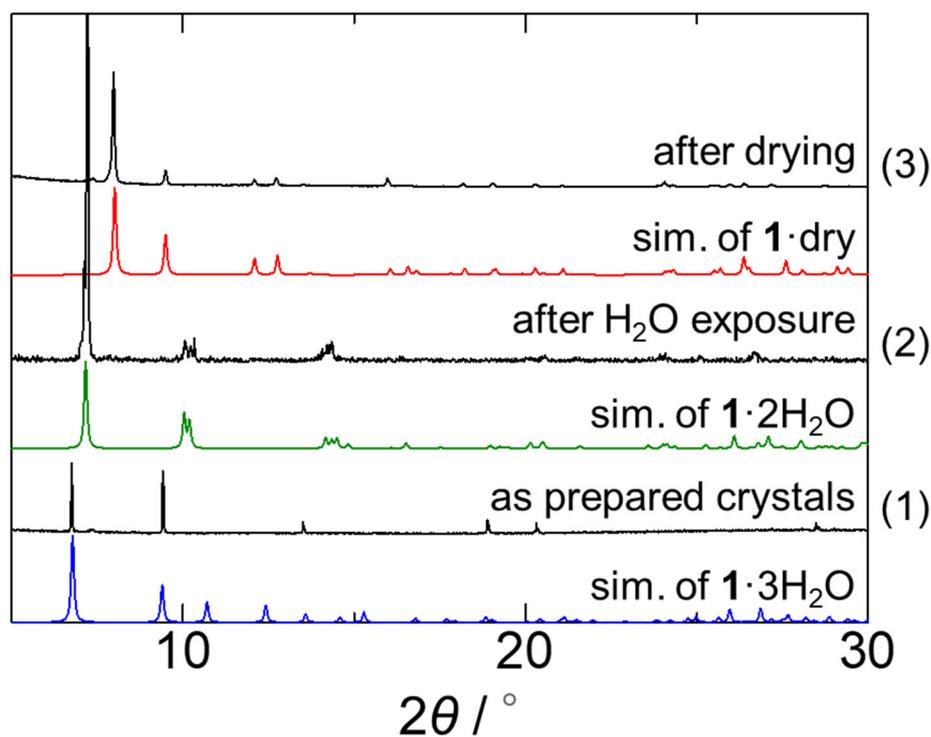
Figure 10. Powder X-ray diffraction measurements that pursued the water vapor desorption/adsorption processes of **Pt-^{t}Bu**·3H$_2$O with the simulation patterns calculated from the single crystal X-ray structures of the three states: (1) as prepared crystals→ (2) after drying →(3) after H$_2$O vapor exposure (20 min.).
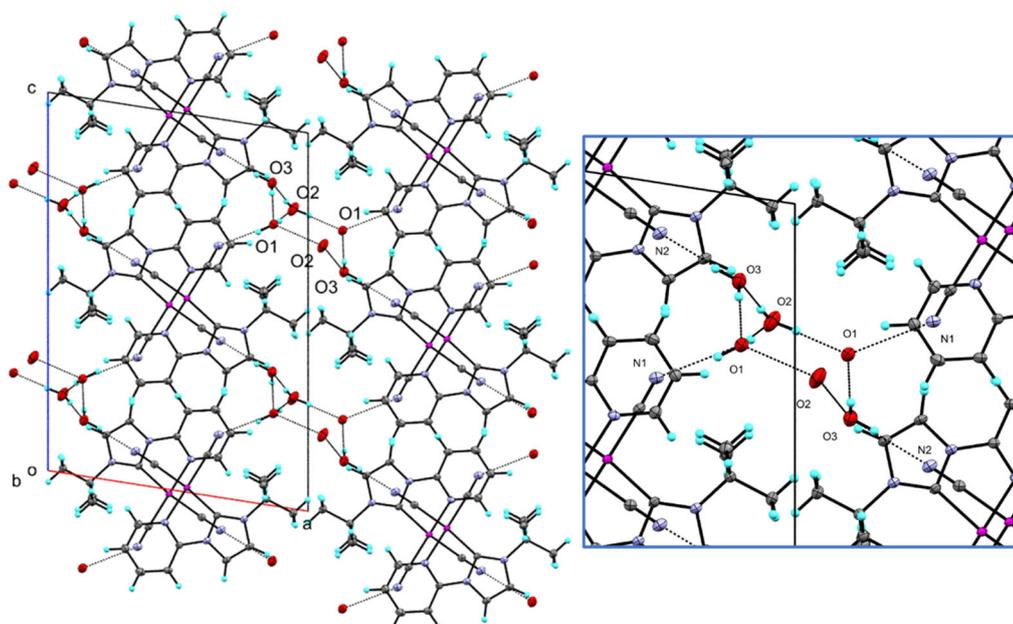
Figure 11. Packing structures with the unit cell viewed along *b* axis for **Pt-^{t}Bu**·3H$_2$O at 100 K with an expanded diagram around the water channel
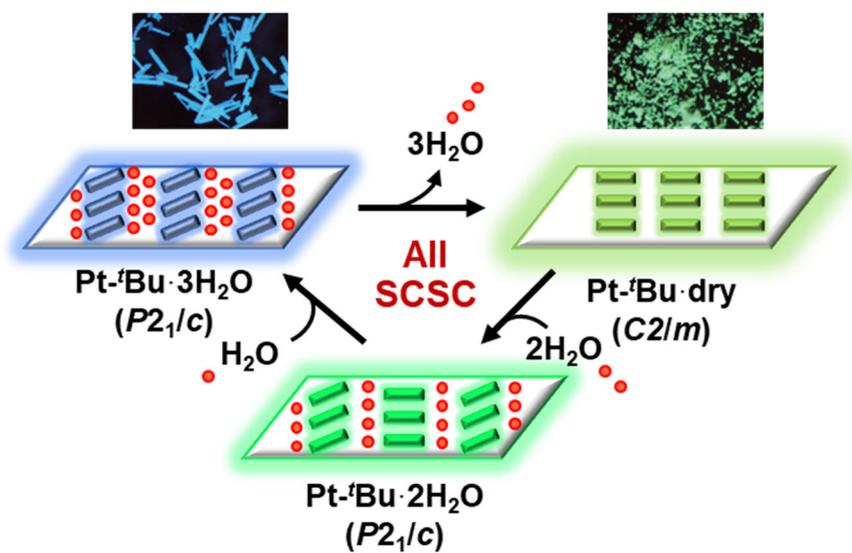
Figure 12. Schematic diagram of structural changes in vapor-induced reversible and stepwise SCSC transition of **Pt-^{t}Bu**

3.3.4 SCSC transformation by MeOH vapors

In addition to water vapor, the vapor-induced SCSC transformation of **Pt-^{t}Bu** · dry was achieved by MeOH vapor. Upon exposure to MeOH vapor at 278 K, the crystals of **Pt-^{t}Bu** · dry were transformed to a MeOH-solvated form, **Pt-^{t}Bu** · MeOH, with space group $P2_1/m$. The coordination plane of **Pt-^{t}Bu** · MeOH is located on the crystallographic mirror plane, similar to that of **Pt-^{t}Bu** · dry with space group $C2/m$. Although the MeOH molecule was disordered, it was linked by a hydrogen bond to the CN ligand (CN· · ·O=2.83 Å) trans to the pyridine of the ^{t}Bu-impy ligand. This position of MeOH is reasonable considering the weaker trans influence of pyridine than that of carbene, as indicated by the corresponding coordination-bond distances. Due to the symmetrical restraint, only one crystallographically independent Pt· · ·Pt distance (3.525(1) Å at 100 K) was observed in the stacking structure of **Pt-^{t}Bu** · MeOH (Figure 13a). This contrasts with the oblique stacking structure for **Pt-^{t}Bu** · 3 H$_2$O which has inequivalent Pt· · ·Pt distances (3.4760(2) and 3.6504(2) Å at 100 K, Table 4). Considering that **Pt-^{t}Bu** · MeOH exhibits almost the same emission spectrum as **Pt-^{t}Bu** · 3 H$_2$O (Figure 13b), the Pt· · ·Pt interactions in the two solvate crystals would be very similar in the ^{3}MMLCT excited states regardless of the difference in the ground state structures. It is interesting to note that the average distance of 3.57 Å in **Pt-^{t}Bu** · 3 H$_2$O is similar to the Pt· · ·Pt distance in **Pt-^{t}Bu** · MeOH (3.525(1) Å). These results are consistent with a good correlation between the average Pt· · ·Pt distance in the ground state structure and the ^{3}MMLCT emission energy, suggesting an expansion of the excited state over the trimer or tetramer.[39]
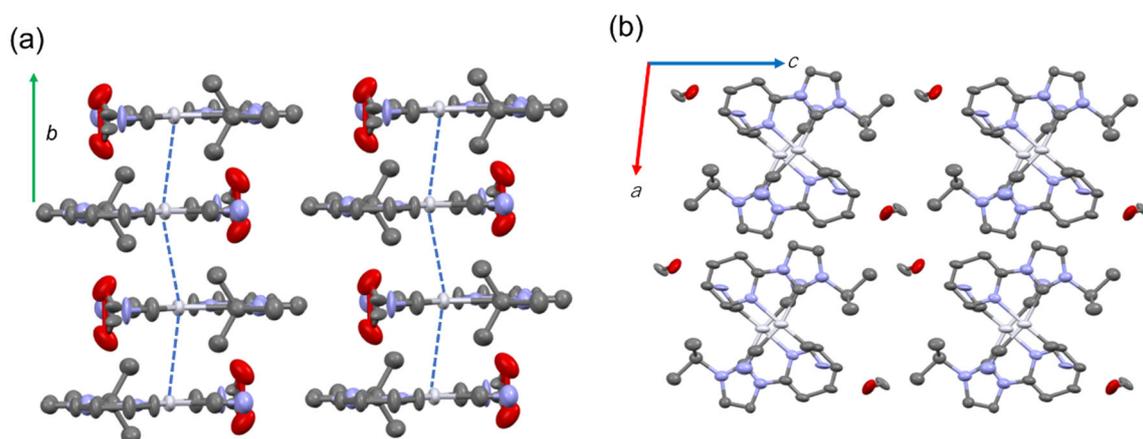

Figure 13. (a) stacking structure of the Pt(II) complex, (b) a packing structure for **Pt-^{t}Bu**·MeOH.

3.4 Conclusion

The vapor-induced reversible and stepwise SCSC transformation of a highly luminescent Pt(II) complex, [Pt(CN)2(^{t}Bu-impy)] (**Pt-^{t}Bu**), was investigated through temperature-dependent and in-situ single-crystal X-ray diffraction measurements. The blue luminescence of the trihydrate form, **Pt-^{t}Bu** · 3 H_2O, originated from the ^{3}MMLCT state derived from the stacking structure with moderately weak Pt···Pt interactions. The emission color changed from blue (λ_{max}=484 nm) to yellowish-green (λ_{max}=533 nm) with the release of water molecules, and a very high quantum yield (0.70→0.61) was maintained. Variable-temperature single-crystal X-ray structure analysis of **Pt-^{t}Bu** · 3 H_2O ($P2_1/c$) revealed the desorption of solvated water through the SCSC transformation to form the unsolvated form, **Pt-^{t}Bu** · dry ($C2/m$). Moreover, in-situ tracking of the SCSC transformations revealed two-step changes upon exposure of **Pt-^{t}Bu** · dry to water vapor; **Pt-^{t}Bu** · 3 H_2O was regenerated via **Pt-^{t}Bu** · 2 H_2O ($P2_1/c$) with an intermediate stacking structure. In addition, when **Pt-^{t}Bu** · dry was exposed to MeOH vapor, a MeOH-solvated crystal (**Pt-^{t}Bu** · MeOH, $P2_1/c$) was obtained that exhibited a blue luminescence, similar to that from the trihydrate form **Pt-^{t}Bu** · 3 H_2O, although the stacking manner (parallel stacking) of **Pt-^{t}Bu** · MeOH was different from that of **Pt-^{t}Bu** · 3 H_2O, which showed oblique stacking. The vapor uptake by **Pt-^{t}Bu** · dry was selective and did not respond to ethanol vapor. Such reversible and stepwise SCSC transformations induced by vapor were realized for the first time in this particular complex bearing a bulky tert-butyl group on the N-heterocyclic carbene ligand, which formed a moderately loose stacking structure. By comparing the stacking structures of compounds that exhibited very similar blue emission that is **Pt-^{t}Bu** · 3 H_2O and **Pt-^{t}Bu** · MeOH, these results confirmed that the average Pt···Pt distance in the ground state can be a rough indicator of the strength of the Pt···Pt interaction in the excited state and, thus, the emission energy. The dynamic SCSC transformations of this system also demonstrated the importance of pressure control of not only water vapor but also air pressure for vapochromic transformation. In conclusion, the vapor-induced reversible SCSC transformations of the Pt(II) complex provide useful information pertaining to assembly-induced luminescence for the development of new materials referred to as soft crystals.

References

[1] I. Halasz, *Cryst. Growth Des.* **2010**, 10, 2817–2823.

[2] S. Reinoso, B. Artetxe, J. M. Gutierrez-Zorrilla, *Acta Crystallogr. Sect. C* **2018**, 74, 1222–1242.

[3] A. Chaudhary, A. Mohammad, S. M. Mobin, *Cryst. Growth Des*. **2017**, 17,2893–2910.

[4] a) S. Kobatake, M. Irie, *Bull. Chem. Soc. Jpn.* **2004**, 77, 195–210; b) S.Kobatake, S. Takami, H. Muto, T. Ishikawa, M. Irie, *Nature* **2007**, 446,778–781.

[5] J.-G. Yu, M.-M. Gan, S. Bai, Y.-F. Han, *CrystEngComm* **2019**, 21, 4673–4683.

[6] F. Hu, X. Bi, X. Chen, Q. Pan, Y. Zhao, *Chem. Lett.* **2021**, 50, 1015–1029.

[7] M. E. van der Boom, *Angew. Chem. Int. Ed.* **2011**, 50, 11846–11848.

[8] J. J. Vittal, *Coord. Chem. Rev.* **2007**, 251, 1781–1795.

[9] C. P. Li, J. Chen, C. S. Liu, M. Du, *Chem. Commun.* **2015**, 51, 2768–2781.

[10] Y. Han, H. V. Huynh, *Dalton Trans.* **2011**, 40, 2141–2147.

[11] E. Fernandez-Bartolome, A. Martinez-Martinez, E. Resines-Urien, L. Piñeiro-Lopez, J. S. Costa, *Coord. Chem. Rev.* **2022**, 452, 214281.

[12] A. J. Sindt, M. D. Smith, S. Berens, S. Vasenkov, C. R. Bowers, L. S.Shimizu, *Chem. Commun.* **2019**, 55, 5619–5622.

[13] S. Lee, S. Y. Hwang, H. Lee, O.-S. Jung, *Cryst. Growth Des.* **2018**, 18, 1278–1282.

[14] M. Kato, M. Yoshida, Y. Sun, A. Kobayashi, *J. Photochem. Photobiol. C* **2022**, 51, 100477.

[15] M. Jin, T. Sumitani, H. Sato, T. Seki, H. Ito, *J. Am. Chem. Soc.* **2018**, 140, 2875–2879.

[16] A. Iturrospe, B. Artetxe, S. Reinoso, L. San Felices, P. Vitoria, L. Lezama, J. M. Gutierrez-Zorrilla, *Inorg. Chem.* **2013**, 52, 3084–3093.

[17] S. Khatua, S. Goswami, S. Biswas, K. Tomar, H. S. Jena, S. Konar, *Chem. Mater.* **2015**, 27, 5349–5360.

[18] Y. S. Jung, C. A. Ross, *Nano Lett.* **2007**, 7, 2046–2050.

[19] A. Kulkarni, T. Singh, A. K. Jena, P. Pinpithak, M. Ikegami, T. Miyasaka, *ACS Appl. Mater. Interfaces* **2018**, 10, 9547–9554.

[20] E. Miliutina, O. Guselnikova, V. Marchuk, R. Elashnikov, V. Burtsev, P. Postnikov, V. Svorcik, O. Lyutakov, *Langmuir* **2018**, 34, 12861–12869.

[21] M. Kato, H. Ito, M. Hasegawa, K. Ishii, *Chem. Eur. J.* **2019**, 25, 5105–5112.

[22] K. M.-C. Wong, V. W.-W. Yam, *Coord. Chem. Rev.* **2007**, 251, 2477–2488.

[23] V. W. Yam, V. K. Au, S. Y. Leung, *Chem. Rev.* **2015**, 115, 7589–7728.

[24] K. Li, G. S. Ming Tong, Q. Wan, G. Cheng, W. Y. Tong, W. H. Ang, W. L. Kwong, C. M. Che, *Chem. Sci.* **2016**, 7, 1653–1673.

[25] O. S. Wenger, *Chem. Rev.* **2013**, 113, 3686–3733.

[26] M. Kato, *Bull. Chem. Soc. Jpn.* **2007**, 80, 287–294.

[27] A. Kobayashi, M. Kato, *Eur. J. Inorg. Chem.* **2014**, 4469–4483.

[28] G. Gliemann, H. Yersin, *Struct. Bonding* **1985**, 62, 87–153.

[29] T. J. Wadas, Q.-M. Wang, Y. Kim, C. Flaschenreim, T. N. Blanton, R. Eisenberg, *J. Am. Chem. Soc.* **2004**, 126, 16841–16849.

[30] M. Kato, A. Omura, A. Toshikawa, S. Kishi, Y. Sugimoto, *Angew. Chem. Int. Ed.* **2002**, 41, 3183–3185

[31] K. R. England, S. H. Lim, L. M. C. Luong, M. M. Olmstead, A. L. Balch, *Chem. Eur. J.* **2019**, 25, 874–878.

[32] D. Saito, T. Ogawa, M. Yoshida, J. Takayama, S. Hiura, A. Murayama, A.Kobayashi, M. Kato, *Angew. Chem. Int. Ed.* **2020**, 25, 874–878.

[33] J. J. Zheng, S. Kusaka, R. Matsuda, S. Kitagawa, S. Sakaki, *J. Am. Chem. Soc.* **2018**, 140, 13958–13969.

[34] P. Kar, M. Yoshida, Y. Shigeta, A. Usui, A. Kobayashi, T. Minamidate, N.Matsunaga, M. Kato, *Angew. Chem. Int. Ed.* **2017**, 56, 2345–2349

[35] D. R. Lide, CRC Handbook of Chemistry and Physics on CD-ROM, CRC Press, **2003.**

[36] I. A. Baburin, V. A. Blatov, *Acta Crystallogr. Sect. B* **2004**, 60, 447–452.

[37] A. L. Spek, *Acta Crystallogr. Sect. C* **2015**, 71, 9–18.

[38] S. Kawaguchi, M. Takemoto, H. Tanaka, S. Hiraide, K. Sugimoto, Y. Kubota, *J. Synchrotron Radiat.* **2020**, 27, 616–624.

[39] M. Nakagaki, S. Aono, M. Kato, S. Sakaki, *J. Phys. Chem. C* **2020**, 124, 10453–10461.

[40] W. R. Dawson, M. W. Windsor, *J. Phys. Chem.* **1968**, 72, 3251–3260.

[41] W. H. Melhuish, *J. Phys. Chem. C* **1961**, 65, 229–235.

[42] CrystalClear, Molecular Structure Corporation, Orem, UT, 2001.

[43] CrysAlisPro, version 1.171.40.67a. Rigaku Corporation, Oxford, UK, 2018.

[44] G. M. Sheldrick, *Acta Crystallogr. Sect..* **2015**, 71, 3–8.

[45] G. M. Sheldrick, *Acta Crystallogr. Sect. A.* **2008**, 64,112–122.

[46] G. M. Sheldrick, *Acta Crystallogr. Sect. C* **2015**, 71, 3–8.

[47] O. V. Dolomanov, L. J. Bourhis, R. J. Gildea, J. A. K. Howard, H. Puschmann, *J. Appl. Crystallogr.* **2009**, 42, 339–341.

[48] C. F. Macrae, I. J. Bruno, J. A. Chisholm, P. R. Edgington, P. McCabe, E. Pidcock, L. Rodriguez-Monge, R. Taylor, J. van de Streek, P. A. Wood, *J.Appl. Crystallogr.* **2008**, 41, 466–470.

[49] Gaussian 16, Revision C.01, M. J. Frisch, G. W. Trucks, H. B. Schlegel, G. E. Scuseria, M. A. Robb, J. R. Cheeseman, G. Scalmani, V. Barone, G. A. Petersson, H. Nakatsuji, X. Li, M. Caricato, A. V. Marenich, J. Bloino, B. G. Janesko, R. Gomperts, B. Mennucci, H. P. Hratchian, J. V. Ortiz, A. F. Izmaylov, J. L. Sonnenberg, D. Williams-Young, F. Ding, F. Lipparini, F. Egidi, J. Goings, B. Peng, A. Petrone, T. Henderson, D. Ranasinghe, V. G. Zakrzewski, J. Gao, N. Rega, G. Zheng, W. Liang, M. Hada, M. Ehara, K. Toyota, R. Fukuda, J. Hasegawa, M. Ishida, T. Nakajima, Y. Honda, O. Kitao, H. Nakai, T. Vreven, K. Throssell, J. A. Montgomery, Jr., J. E. Peralta, F. Ogliaro, M. J. Bearpark, J. J. Heyd, E. N. Brothers, K. N. Kudin, V. N. Staroverov, T. A. Keith, R. Kobayashi, J. Normand, K. Raghavachari, A. P. Rendell, J. C. Burant, S. S. Iyengar, J. Tomasi, M. Cossi, J. M. Millam, M. Klene,

C. Adamo, R. Cammi, J. W. Ochterski, R. L. Martin, K. Morokuma, O. Farkas, J. B. Foresman, D. J. Fox, Gaussian, Inc., Wallingford CT, 2016.

[50] Y. Zhao, D. G. Truhlar, *Theor. Chem. Acc.* **2008**, 120, 215–241.

[51] D. Andrae, U. Häussermann, M. Dolg, H. Stoll, H. Preuss, *Theor. Chim. Acta* **1990**, 77, 123–141.

[52] R. Krishnan, J. S. Binkley, R. Seeger, J. A. Pople, *J. Chem. Phys.* **1980**, 72,650–654.

Chapter 4

Assembly-Induced Luminescent M(II) Complexes (M=Pt, Pd) with a C^N^C Tridentate *N*-Heterocyclic Carbene

4.1 Introduction

Among many phosphorescent metal complexes, platinum(II) complexes with a square-planer geometry have fascinating properties because of not only their strong intrinsic emission but also their characteristic "assembly-induced" luminescent behavior based on the Pt···Pt electronic interactions. [1]Typically, the square-planer platinum(II) complexes form the bonding dσ and the antibonding dσ* orbitals by the overlapping of occupied d_z^2 orbitals in their stacked forms with short Pt···Pt contacts. When appropriate aromatic ligands are introduced into such systems, they often exhibit characteristic absorption/luminescence assignable to a charge transfer transition between the dσ* orbital and the π* orbital of the ligand, so-called the metal-metal-to-ligand charge transfer (MMLCT) transition. Since the MMLCT absorption/emission energies sharply reflect the intermolecular Pt···Pt interactions, research of the assembly-induced luminescence has been conducted to develop sensor materials for heat, volatile organic compounds (VOCs), and other stimuli. [2]The metal-metal interactions have been investigated in other metal complex systems, such as Au(I) and Ag(I) complexes with the d^{10} configuration and Rh(I) complexes with the same d^8 configuration as Pt(II) complexes.[3]However, there are a few examples of assembly-induced luminescence of Pd(II) complexes [4–6] which are homologous atoms to platinum. There are two reasons why there are few examples of assembly-induced luminescence in Pd(II) complexes: 1) The $4d_z^2$ orbital of Pd(II) complexes is less extended compared with the $5d_z^2$ orbital of Pt(II) complexes, so that the metal-metal interactions between Pd(II) complexes are weak in the isostructural systems of the Pt(II) analogues. 2) Weaker ligand fields of Pd(II) complexes than Pt(II) complexes give rise to non-radiative deactivation via an easily accessible ^{3}dd excited state. To overcome the difficulties of Pd(II) complexes, the molecular design to realize much shorter Pd(II)···Pd(II) distances and much stronger ligand fields have been explored. In 2017, Che and co-workers reported MMLCT emissive Pd(II) complexes with C^N^N type tridentate ligands. In 2018, Lu and co-workers also reported self-assembled Pd(II) complexes by Pd···Pd interactions with 3MMLCT emission. In 2019, Lu and co-workers reported highly emissive dinuclear Pd(II) complexes in solution, not only the solid state. However, reported assembly-induced luminescent Pd(II) complexes are still very few, and molecular design remains challenging.

Herein, this chapter focus on C^N^C type tridentate imidazole-type NHC ligands, which are expected to have strong luminescence properties due to their strong sigma donor ability and more rigid structure than C^N type bidentate ligands. And, Synthesis and photophysical properties of a series of cationic Pt(II) and Pd(II) complexes bearing with a tridentate NHC ligand, [M(bisimpy)CN]PF$_6$(M=Pt(**Pt-CN**), Pd(**Pd-CN**); bisimpy= 2,6-bis(3-methyl-1*H*-imidazol-2-ylidene)pyridine (Figure 1) were investigated.
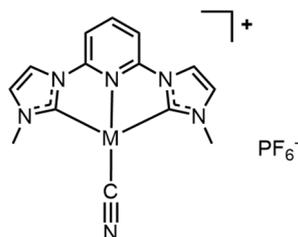

Figure 1. Molecular structure of [M(bisimpy)CN]PF$_6$(M=Pt(**Pt-CN**), Pd(**Pd-CN**)

4.2 Experimental

4.2.1 Materials

Potassium tetrachloridoplatinate(II) ($K_2[PtCl_4]$) was purchased from Tanaka Holdings Co., Inc. All other reagents were purchased from Wako Pure Chemical Industries, Ltd. All solvents were purchased from Kanto Chemical Co., Inc. $[Pt_2(\mu\text{-}Cl)_2(\eta^3\text{-}Me\text{-}C_3H_4)_2]$[7],$[Pd(bisimpy)Br]PF_6$[8] were synthesized according to literature methods.

Synthesis of $[Pt(bisimpy)CN]PF_6$ (**Pt-CN**)

$[Pt_2(\mu\text{-}Cl)_2(\eta^3\text{-}Me\text{-}C_3H_4)_2]$ (149.3 mg, 0.263 mmol), NH4Cl (60 mg, 1.12 mmol), (bisimpyH$_2$)PF$_6$ (278mg, 0.523 mmol) were suspended in acetonitrile (100 mL), and added triethylamine (0.14 mL), then refluxed overnight. The reaction mixture was evaporated and washed with $CHCl_3$, MeOH, H_2O, obtained yellow solid, and AgCN (12.4 mg, 0.093 mmol) suspended in acetonitrile (10 mL) and stirred overnight under excluded light conditions. Then, the reaction mixture was filtered through celite. The filtrate was evaporated to dryness. After recrystallization from acetonitrile/Et$_2$O, the orange crystal was obtained. Yield, 14.5 mg (0.024 mmol, 4.6%).

^{1}H-NMR (500 MHz, DMSO-D6) δ 8.57 (t, J = 8.3 Hz, 1H), 8.45 (d, J = 1.7 Hz, 2H), 8.00 (d, J = 8.6 Hz, 2H), 7.75 (d, J = 1.7 Hz, 2H), 4.04 (s, 6H)

Synthesis of $[Pd(bisimpy)CN]PF_6$ (**Pd-CN**)

$[Pd(bisimpy)Br]PF_6$ (118 mg, 0.207 mmol) and AgCN (31.5 mg, 0.235 mml) were suspended in acetonitrile (10 mL), and stirred overnight under excluded light conditions. Then, the reaction mixture was filtered through celite. The filtrate was evaporated to dryness. After recrystallization from acetonitrile/Et$_2$O, the colorless crystal was obtained. Yield, 80.3 mg (0.155 mmol, 75%).

^{1}H NMR (500 MHz, DMSO-D6) δ 8.57 (t, J = 8.3 Hz, 1H), 8.45 (d, J = 1.7 Hz, 2H), 8.00 (d, J = 8.6 Hz, 2H), 7.75 (d, J = 1.7 Hz, 2H), 4.04 (s, 6H).   Anal. calcd for $C_{14}H_{13}F_6N_6PPd$: C, 32.54; H, 2.54; N, 16.27%. Found: C, 32.64; H, 2.43; N, 16.25%. MS (ESI) m/z: $[M]^+$ calcd for $C_{11}H_9N_5Pd^+$, 371.02; found, 371.02

4.2.2 Photophysical measurements

Luminescence spectra were recorded using a JASCO FP-8600 spectrofluorometer at room temperature, and 77 K. Slit widths of excitation and emission light were 5 nm. Variable temperature luminescence spectra were measured with a Hamamatsu Photonics multichannel photodetector (PMA-11) and nitrogen laser (Usho KEN-X) for 337 nm excitation. A liquid nitrogen cryostat (Optistat-DN optical Dewer and ITC-503 temperature controller, Oxford instruments) was used for temperature control. Absolute luminescent quantum yields were recorded on a Hamamatsu Photonics C9920-02 absolute photoluminescence quantum yield measurement system equipped with an integrating sphere apparatus and a 150 W CW xenon light source. A Hamamatsu Photonics A10095-3 non-luminescent quartz sample holder was used for absolute photoluminescence quantum yield measurements. The accuracy of the

instrument was confirmed by the measurement of the quantum yield of anthracene in ethanol solution ($\Phi = 0.27$).[9,10] Emission lifetime measurements and time-resolved emission spectra were recorded using a Hamamatsu Photonics C4780 system equipped with a streak camera (Hamamatsu Photonics C4334) as a photodetector and a nitrogen laser for the 337 nm excitation. The emission decays were analyzed using two exponentials; $I = A_1\exp(-t/\tau_1) + A_2\exp(-t/\tau_2)$, where A_i denotes the pre-exponential factors for lifetimes τ_i. The average emission lifetimes (τ_{av}) were calculated using following equation (1):

$$\tau_{av} = \frac{\sum A_i \tau_i^2}{\sum A_i \tau_i} \qquad (1)$$

4.2.3 Single-crystal X-ray diffraction measurements

All single-crystal X-ray diffraction measurements were performed using a Rigaku XtaLAB Synergy-S diffractometer equipped with HyPix6000HE hybrid photon counting detector and multilayer mirror-monochromated Cu Kα radiation ($\lambda = 1.54184$ Å) and a micro-focus sealed X-ray tube generator. Each single crystal was mounted on a MicroMount using paraffin oil. These single crystals were cooled by using N_2-flow type temperature controller. Diffraction data were collected and processed using the CrysAlisPro software. [11] The structures were solved with the intrinsic phasing method by using the SHELXT-2014.[12] Structural refinements were conducted by the full-matrix least-squares method using the SHELXL-2017.[13] None-hydrogen atoms were refined anisotropically, and all hydrogen atoms were refined using the riding model. All calculations were performed using Olex2 software.[14]

4.2.4 Other measurements

^{1}H NMR spectroscopy was performed using a JEOL ECZ-500R NMR spectrometer. Elemental analyses and ESI mass spectrometry were carried out at the analysis center in Hokkaido University. TG-DTA analysis was performed using a Rigaku Thermo plus Evo2 TG-DTA8122 analyzer. The typical sample mass used for the analysis was 5 mg, and the heating rate was 1 K min^{-1}. UV-vis absorption spectra were measured using a Shimadzu UV-2500PC spectrophotometer. Diffuse reflectance spectra were converted to absorption spectra using the Kubelka-Munk function $F(R^\infty)$. Spectroscopic grades of solvents and a quartz cuvette were used for UV-vis absorption spectra.

4.2.5 Computational methods

Density functional theory (DFT) and time-dependent density functional theory (TD-DFT) were conducted using the Gaussian 16 program.[15] The M06 functional[16] was used for ground-state structure optimizations, vertical excitation energy calculations, and optimizations of the lowest singlet and triplet states for the monomer complexes. The SDD basis set and associated effective core potentials were used for Pt [17], and the 6-311+G(d,p) basis sets were used for other atoms.[18] Unless otherwise stated, structure optimizations were performed without any constraints. Vibrational frequency calculations were performed to confirm the nature of the optimized ground-state (DFT) and excited-

state (TD-DFT) minima (*i.e.*, no imaginary frequencies).

4.3 Results and discussion

4.3.1 Crystal Structures

The structures of **Pt-CN**·PF$_6$, and **Pd-CN**·PF$_6$ were determined by single crystal X-ray diffraction analysis at 150 K. Single crystals of **Pt-Cl**·PF$_6$, **Pt-Br**·PF$_6$, and **Pt-CN**·PF$_6$ were obtained by vapor diffusion of diethyl ether into an acetonitrile solution. The crystal structures are drawn in Figure 2, and the crystallographic data are summarized in Table 1. The complex molecules had a one-dimensional stacked structure with a head-to-tail stacking manner, and their 1D chains were similar in all complexes (Figure 3). The metal···metal distances are 3.6604(3) Å for **Pt-CN** and 3.8303(5) Å for **Pd-CN**, which are larger than twice the van der Waal radius of the central metal (Pt:3.5 Å, Pd: 3.26 Å) in all complex crystals. Moreover, there is no strong typical ππ interaction between the tridentate NHC Ligands, as seen from the head-to-tail stacking structure. On the other hand, the distance between coordination planes is 3.332 Å for **Pt-CN** and 3.378 Å for **Pd-CN**, which indicates relatively close.
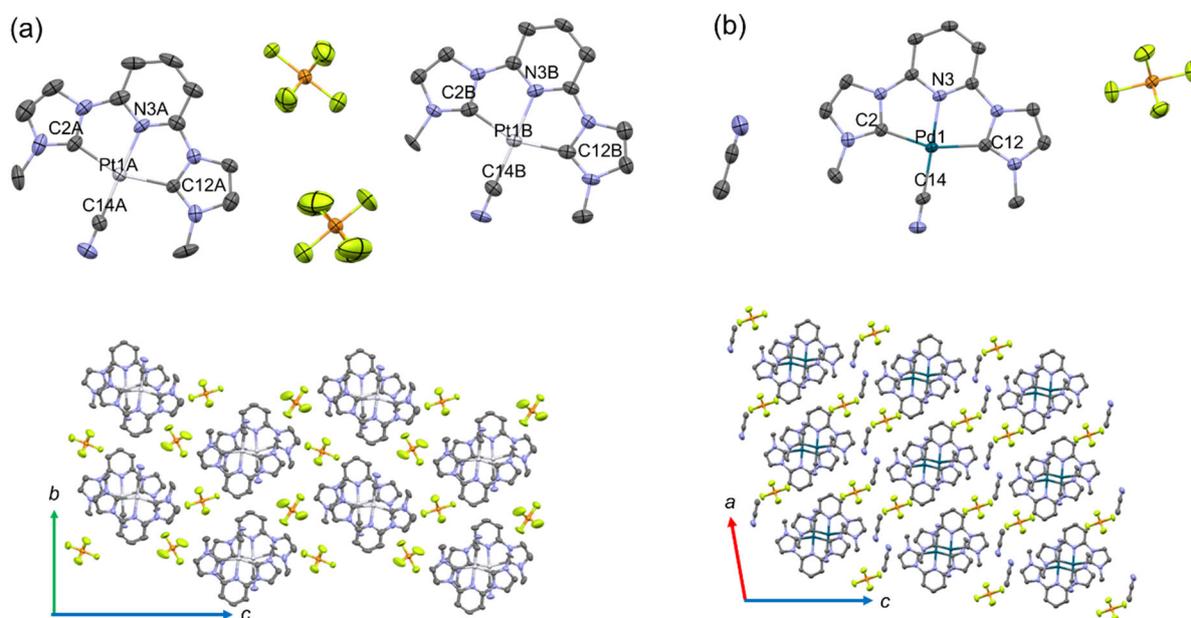
Figure 2. Molecular structures and packing structures of the (a)**Pt-CN** and (b)**Pd-CN** complexes cations. The thermal ellipsoids are displayed at the 50% probability level. Hydrogen atoms are omitted for clarity.
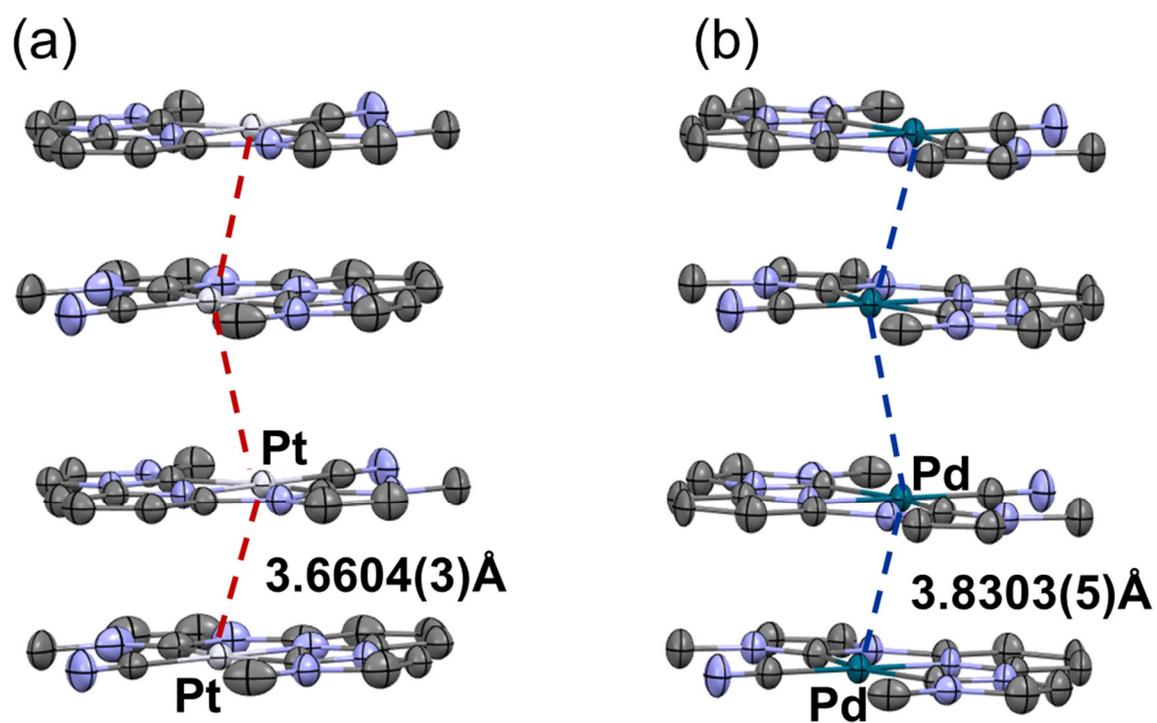
Figure 3. Stacking structures of (a)**Pt-CN**, (b)**Pd-CN**

Table 1. Crystal data for complexes at 150 K.

	Pt-CN	Pd-CN
Formula	$C_{14}H_{13}F_6N_6PPt$	$C_{16}H_{16}F_6N_7PPd$
Formula weight	605.36	557.73
Crystal system	orthorhombic	monoclinic
Space group	$Pmn2_1$	$P2_1/m$
a / Å	6.6647(1)	10.4088(3)
b / Å	11.0143(1)	6.7489(2)
c / Å	24.0832(3)	14.5742(4)
α / °	90	90
β / °	90	104.432(3)
γ / °	90	90
V / Å^3	1767.88(4)	991.50(5)
T / K	150	150
Z	4	2
D_{calc} / g cm^{-3}	2.274	1.868
$F(000)$	1144.0	552.0
Reflections collected	41745	6266
Unique reflections	3873	2170
GOF on F^2	1.113	1.073
R_{int}	0.0693	0.0462
R_1[a]	0.0317	0.0340
wR_2[b] (all data)	0.0916	0.0858

[a]$R_1 = \Sigma||F_o| - |F_c||/\Sigma|F_o|$. [b] $wR_2 = [\Sigma w(F_o^2 - F_c^2)/ \Sigma w(F_o)^2]^{1/2}$, $w = [\sigma_c^2(F_o^2) + (xP)^2 + yP]^{-1}$, $P = (F_o^2 - 2F_c^2)/3$.

Table 2. Selected interatomic distances (Å) and angles (°) for **Pt-CN·PF₆**, and **Pd-CN·PF₆** at 150 K.

	Pt-CN	
	A	B
Pt1–C2	2.04(1)	2.04(1)
Pt1−C12	2.05(2)	2.03(2)
Pt1−N3	2.01(2)	2.03(1)
Pt1-C14	1.97(2)	1.95(2)
Pt1⋯Pt1'	3.6604(3)	
N3−Pt1−C14	178(1)	180(2)
N3−Pt1−C12	77.6(7)	77.6(7)
N3−Pt1−C2	79.9(8)	79.9(8)
C12−Pt1−C14	101(1)	101(1)
C2−Pt1−C14	102(1)	102(1)
C2−Pt1−C12	157.4(5)	157.1(5)
Pt1'⋯Pt1⋯Pt1"	131.12(2)	
	Pd-CN	
Pd1–C2	2.031(5)	
Pd1−C12	2.045(5)	
Pd1−N3	2.002(4)	
Pd1-C14	1.979(5)	
Pd1⋯Pd1"	3.8226(3)	
N3−Pd1−C14	179.22(18)	
N3−Pd1−C12	78.7(2)	
N3−Pd1−C2	79.4(2)	
C12−Pd1−C14	102.1(2)	
C2−Pd1−C14	99.8(2)	
C2−Pd1−C12	158.1(2)	
Pd1'⋯Pd1⋯Pd1"	123.96(2)	

4.3.2 Photophysical properties

Both of **Pt-CN** and **Pd-CN** complexes exhibit photoluminescence in the solid state. The emission spectra are shown in Figure 4, and the photophysical properties are summarized in Table 3. The emission maxima wavelength of two complexes in the solid state were 666 nm for **Pt-CN**(Φ = 0.44), 517 nm for **Pd-CN**(Φ = 0.02), respectively. To investigate the details of emission origin, the emission spectra at 77 K in the solid state were measured (Figure 4a). The spectrum profile of **Pt-CN** was similar to that at room temperature, without the redshift that is usually observed in one-dimensional stacked platinum complexes with MMLCT emission. On the other hand, the emission spectrum of **Pd-CN** at 77K was different from that of RT, and a vibrational structure was observed. All these complexes are non-emissive in solution at room temperature but exhibit emission at 77 K in glassy solution. Next, emission measurements in a glass matrix were conducted to investigate the luminescence in a dispersed state. The emission spectra of **Pt-CN** and P**d-CN** have a very different vibrational structure from that of the solid state at RT, which can be assigned to the phosphorescence from triplet $\pi\pi^*$. The significant difference between **Pt-CN** and **Pd-CN** in spectral profiles between the solid and dilute solutions suggests that the luminescence in the solid originated from an aggregated state.
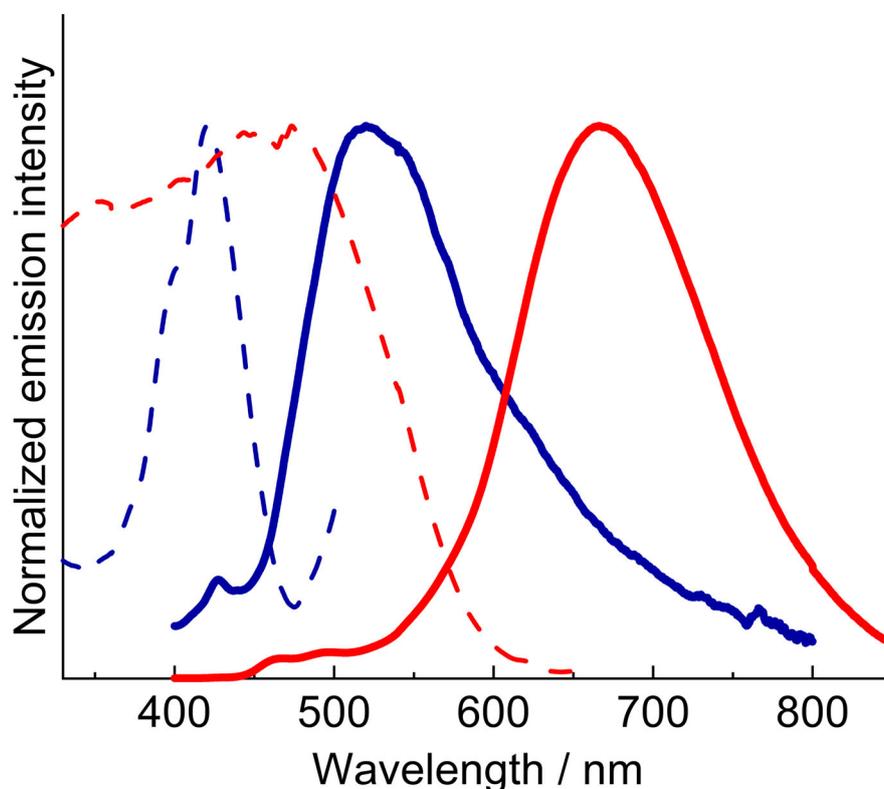
Figure 4. Emission(solid line) and excitation(dashed line) spectra of **Pt-CN**(red) and **Pd-CN**(blue) at room temperature in the solid state.(λ_{ex} = 350 nm)

Table 3. Photophysical properties in the solid state

Complexes	Temperature	$\lambda_{max}{}^a$/ nm	$\varPhi^b$	τ^c [μs (A^d)]	τ_{av} ^{e}(μs)	$k_r{}^f$(s^{-1})	$k_{nr}{}^g$(s^{-1})
PtCN	solid (RT)	666	0.44	0.61(0.37),1.66(0.63)	1.5	2.93×10^5	3.73×10^5
PdCN	solid (RT)	517	0.02	0.22(0.80), 1.4(0.20)	0.95	1.05×10^4	1.04×10^6

^{a} Emission maximum. ^{b} Photoluminescence quantum yields. ^{c} Emission lifetime. ^{d} Pre-exponential factors. ^{e} Average emission lifetimes were determined from the equation $\tau_{av} = \Sigma\, A_i\tau_i{}^2\, /\, \Sigma\, A_i\tau_i$ ($i = 1, 2$). ^{f} Radiative rate constants (k_r) were estimated from the equation $k_r = \varPhi/\tau_{av}$. ^{g} Non-radiative rate constants (k_{nr}) were estimated from the equation $k_{nr} = k_r(1 - \varPhi)/\varPhi$.
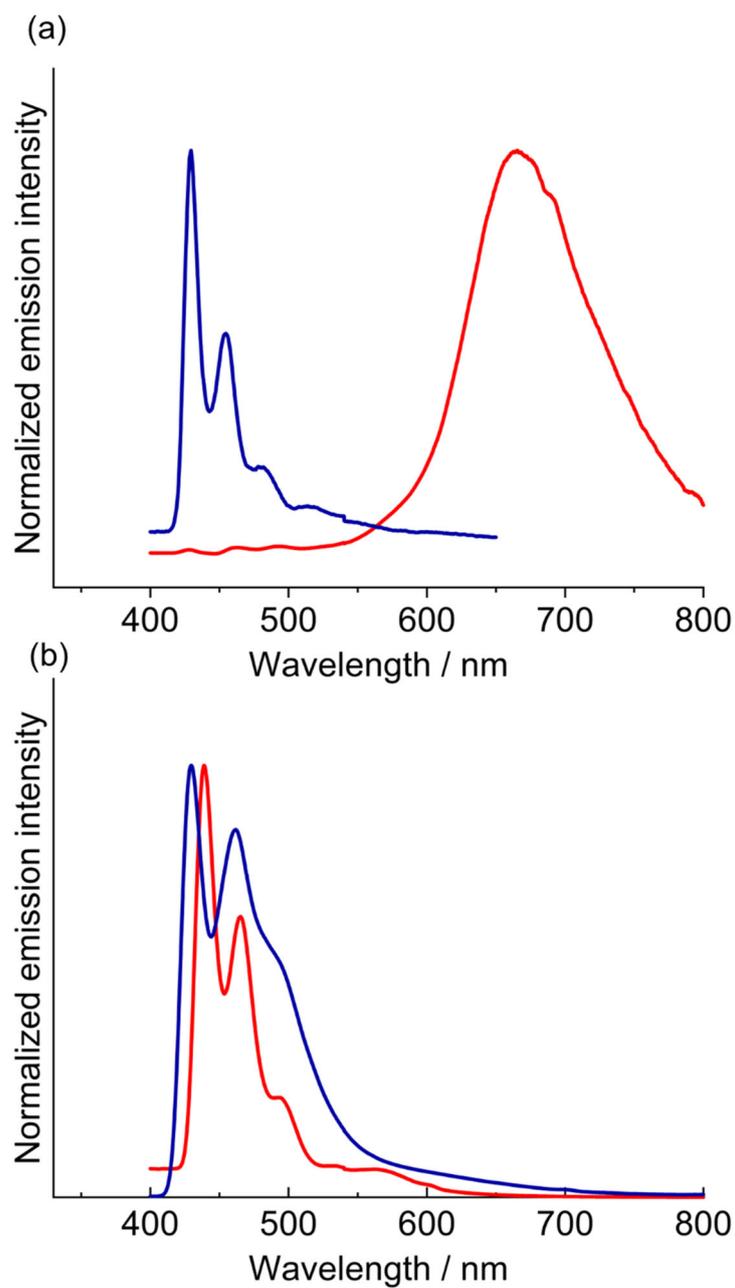
Figure 5. Emission spectra of **Pt-CN**(red) and **Pd-CN**(blue) (a) at 77K in the solid state, (b) in glass matrix(MeOH/EtOH= 1/1 v/v) at 77K.

Figure 6 shows the UV-vis absorption spectra of **Pt-CN** and **Pd-CN** in acetonitrile at room temperature. These complexes exhibited absorption bands in the region of 280-300 nm, which are absent in the absorption spectra of the free ligands. Thus the bands can be assigned to the ^{1}MLCT transition bands, although the TD-DFT calculation results suggest that the metal-perturbed $^1\pi\pi^*$(or ^{1}LC) transitions were mixed. On the other hand, new absorption not observed in the dilute solution was observed in the solid state, as shown in Figure 7. These results suggest that both the excited state and the ground state are affected by intermolecular interactions.
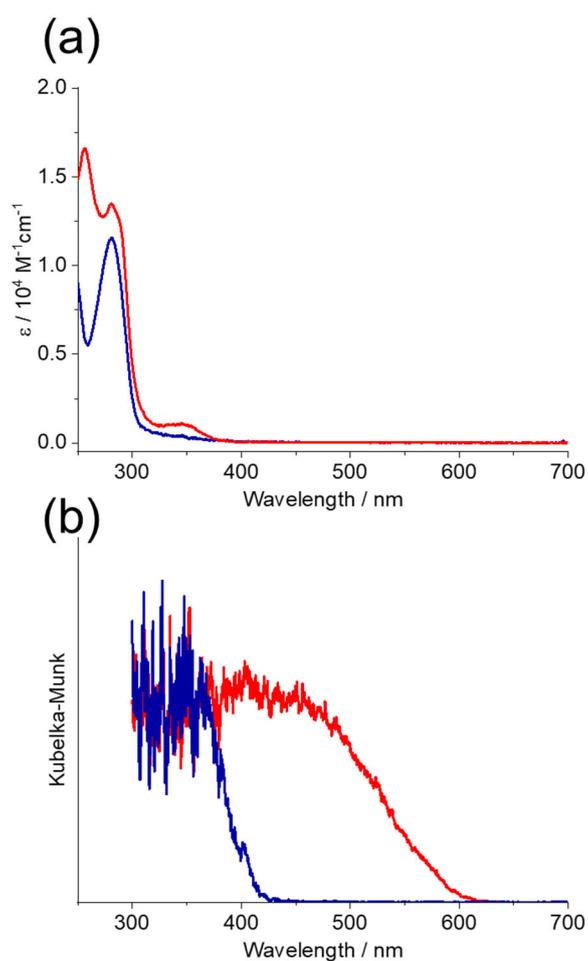
Figure 6. (a) UV-vis absorption spectra in acetonitrile solution, (b)diffuse reflectance spectra in the solid state.
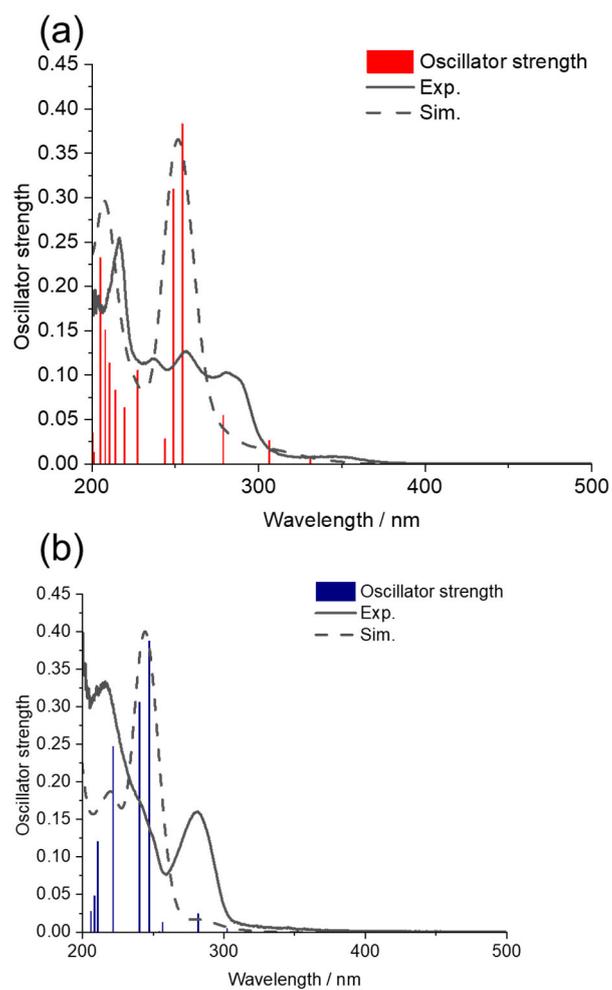
Figure 7. Simulated absorption spectra by TDDFT calculations (a) **Pt-CN**, (b)**Pd-CN** in acetonitrile solution

4.3.3 Thermochromic behavior of **Pd-CN**

To discuss the thermochromic behavior of **Pd-CN**, variable-temperature single-crystal X-ray structural analysis and emission measurements were carried out. Crystallographic parameters at each temperature are summarized in Table 4. TG-DTA results showed that the acetonitrile-solvated crystals were relatively stable under 300 K(Figure 8), but just to be sure, paraffin oil was used to coat the crystals to prevent acetonitrile desorption. **Pd-CN** has $P2_1/m$ space group symmetry from 290 K to 130 K. At even lower temperatures (110 K and 90 K), the unit lattice changed to $P2_1/n$, which corresponded to twice the *c*-axis. Interestingly, an anisotropic shrinkage of the *b*-axis, which is the stacking direction, was observed (Figure 9). Figure 10 shows the crystal structures before(130 K) and after(90 K) space group change. At high temperatures (290 K to 130), the coordination plane and acetonitrile molecules are positioned on a crystallographic mirror plane, and the stacking structure is parallel stacking mode. On the other hand, at low temperatures (110 K and 90 K), the coordination plane gradually moves away from the mirror plane, crystallographic symmetry is reduced, and the space group becomes $P2_1/n$. In addition, the stacking mode changed to oblique stacking mode, which is weak molecular interaction.

Figure 11 shows the temperature dependence of emission spectra. The luminescence intensity decreased with increasing temperature, and the emission band observed at room temperature appeared on the long wavelength. This emission change corresponds to the results of the crystal structure analysis. At low temperatures, the luminescence intensity is high and intermolecular interactions are weak because molecular motion is suppressed, while at high temperatures, molecular motion increases, and the excited states are easily deactivated, while the degree of intermolecular freedom increases and assembly-induced emission is observed. Overall, the thermochromic luminescence behavior of **Pd-CN** is depicted in Figure 12, schematically.
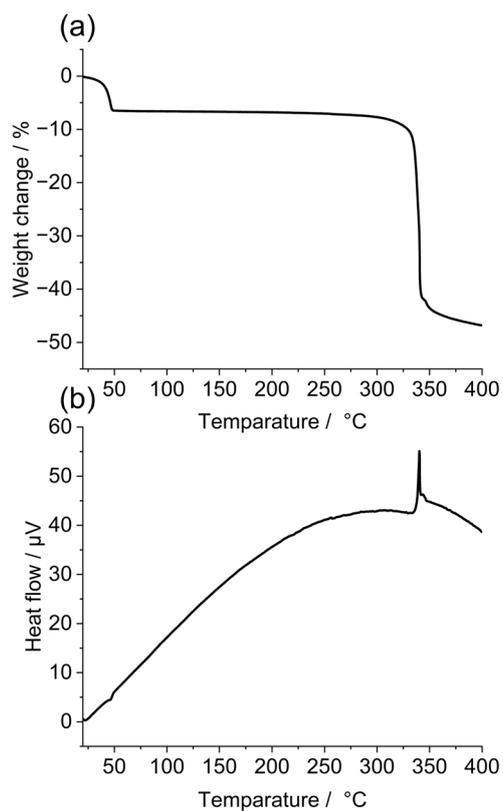
Figure 8. (a) Thermogravimetric and (b) differential thermal analysis (TG-DTA) of **Pd-CN** in the measurement conditions under Ar flow (0.3 L/min) (orange lines)
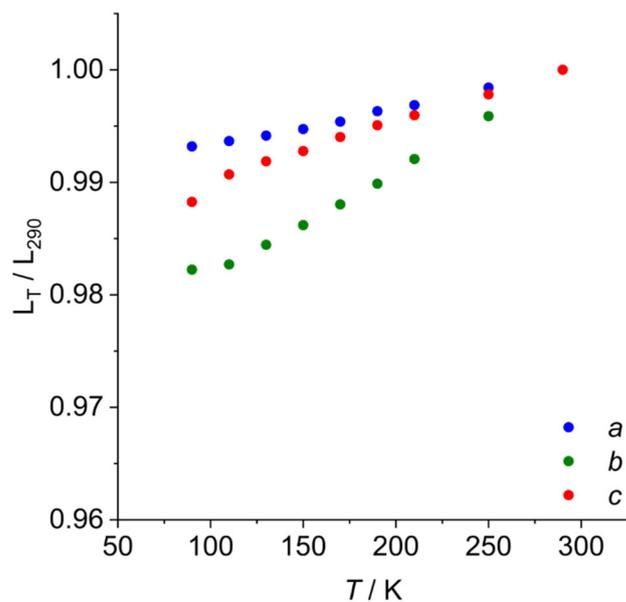

Figure 9. The ratio of cell lengths (*a*, *b*, and *c*) of **Pd-CN** relative to that at 290 K. For comparison, the *c* axis of 290 K to 130 K was doubled.
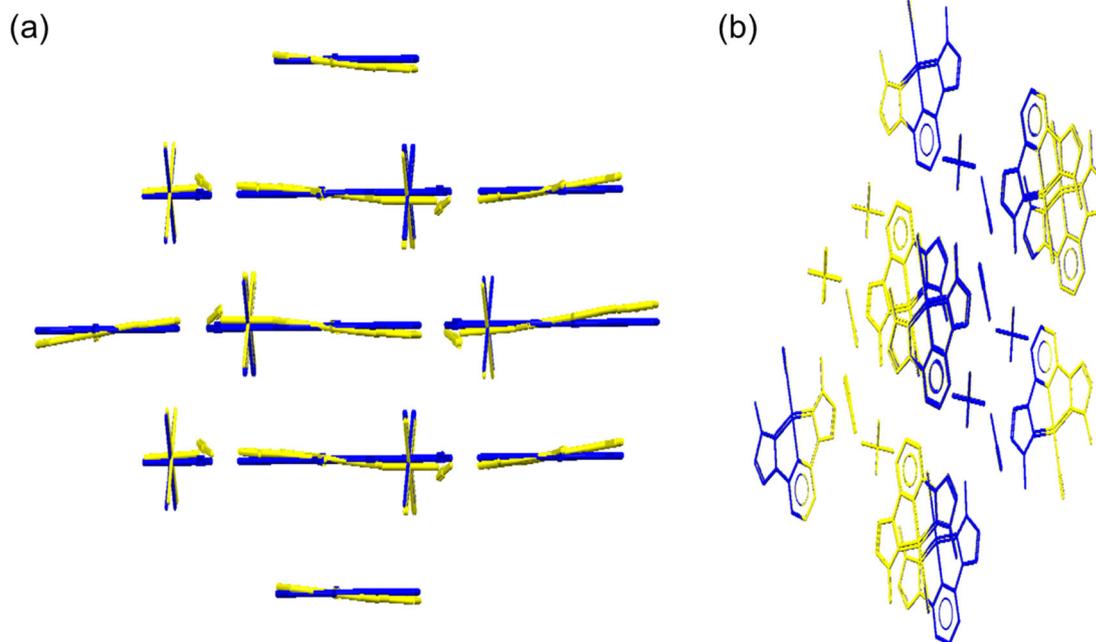
Figure 10. Comparison of packing structure of **Pd-CN** at 90 K(yellow) and 130 K(blue). (a)side view, and (b) top view
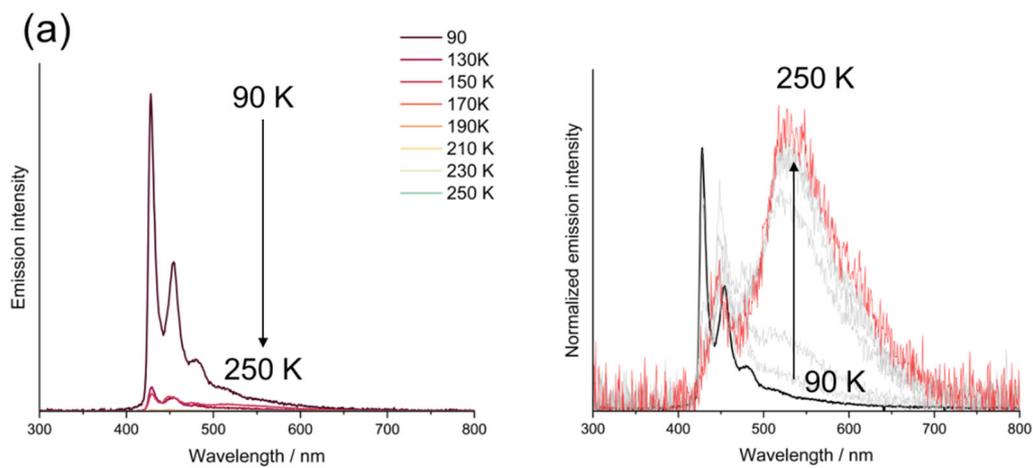

Figure 11. (a)Temperature dependence of emission spectra, (b)normalized intensity to discuss thermochromic behavior.
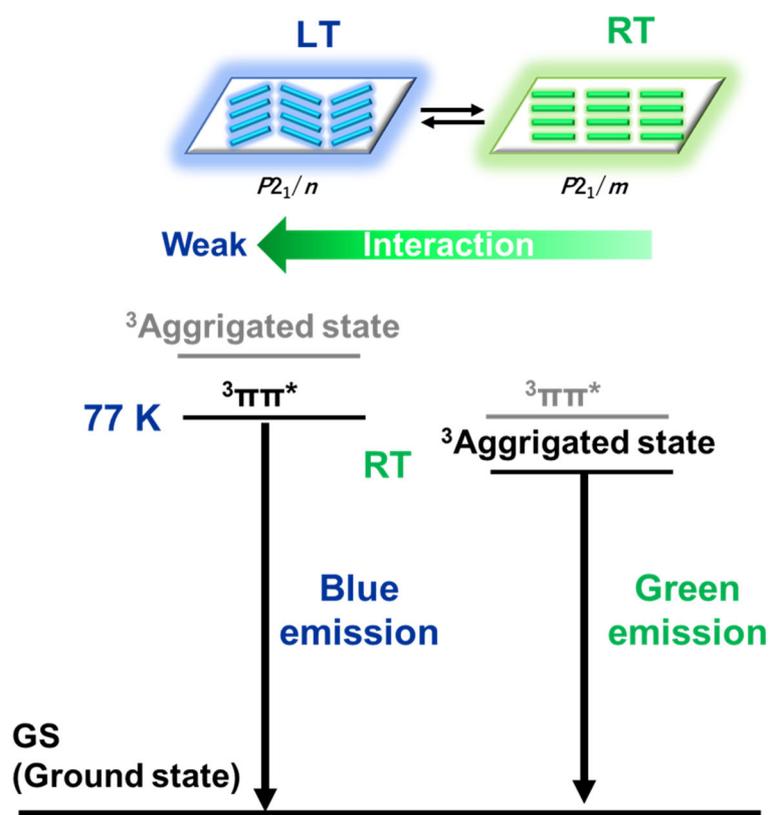
Figure 12. Schematic energy diagram of **Pd-CN**

Table 4. Crystal data for **Pd-CN** at various temperatures during 90–290 K.

T / K	90	110	130	150	170	190
Formula	$C_{16}H_{16}F_6N_7PPd$	$C_{16}H_{16}F_6N_7PPd$	$C_{16}H_{16}F_6N_7PPd$	$C_{16}H_{16}F_6N_7PPd$	$C_{16}H_{16}F_6N_7PPd$	$C_{16}H_{16}F_6N_7PPd$
Formula weight	557.73	557.73	557.73	557.73	557.73	557.73
Crystal system	monoclinic	monoclinic	monoclinic	monoclinic	monoclinic	monoclinic
Space group	$P2_1/n$	$P2_1/n$	$P2_1/m$	$P2_1/m$	$P2_1/m$	$P2_1/m$
a / Å	10.39500(10)	10.40000(10)	10.4048(3)	10.4096(3)	10.4163(2)	10.4253(2)
b / Å	6.72420(10)	6.72740(10)	6.74043(19)	6.75183(19)	6.76468(16)	6.77846(15)
c / Å	28.2831(4)	28.3533(4)	14.5650(4)	14.5725(4)	14.5931(4)	14.6024(3)
α / °	90	90	90	90	90	90
β / °	96.3020(10)	96.3370(10)	104.433(3)	104.397(3)	104.350(2)	104.316(2)
γ / °	90	90	90	90	90	90
V / Å^3	1964.99(4)	1971.62(4)	989.25(5)	992.05(5)	996.19(4)	999.87(4)
Z	4	4	2	2	2	2
D_{calc} / g cm^{-3}	1.885	1.879	1.872	1.867	1.859	1.853
$F(000)$	1104.0	1104.0	552.0	552.0	552.0	552.0
Reflections collected	11925	12583	6374	6457	6362	6431
Unique reflections	3917	3970	2165	2173	2165	2181
GOF on F^2	0.0340	0.0292	0.0264	0.0280	0.0263	0.0270
R_{int}	1.069	1.062	1.079	1.065	1.061	1.056
R_1[a]	0.0340	0.0292	0.0264	0.0280	0.0263	0.0270
wR_2[b] (all data)	0.0297	0.0298	0.0248	0.0238	0.0241	0.0237

(continued)

T / K	210	250	290
Formula	$C_{16}H_{16}F_6N_7PPd$	$C_{16}H_{16}F_6N_7PPd$	$C_{16}H_{16}F_6N_7PPd$
Formula weight	557.73	557.73	557.73
Crystal system	monoclinic	monoclinic	monoclinic
Space group	$P2_1/m$	$P2_1/m$	$P2_1/m$
a / Å	10.4335(3)	10.4508(3)	10.4667(3)
b / Å	6.7932(2)	6.8216(2)	6.8454(2)
c / Å	14.6141(4)	14.6420(4)	14.6556(4)
α / °	90	90	90
β / °	104.261(3)	104.176(3)	104.120(3)
γ / °	90	90	90
V / Å^3	1003.88(5)	1012.06(5)	1018.33(5)
Z	2	2	2
D_{calc} / g cm^{-3}	1.845	1.83	1.819
$F(000)$	552.0	552.0	552.0
Reflections collected	6680	6730	6758
Unique reflections	2191	2211	2221
GOF on F^2	0.0278	0.0290	0.0346
R_{int}	1.075	1.141	1.074
R_1[a]	0.0278	0.0290	0.0346
wR_2[b] (all data)	0.0253	0.0280	0.0335

[a] $R_1 = \Sigma||F_o| - |F_c||/\Sigma|F_o|$. [b] $wR_2 = [\Sigma w(F_o^2 - F_c^2)/ \Sigma w(F_o)^2]^{1/2}$, $w = [\sigma_c^2(F_o^2) + (xP)^2 + yP]^{-1}$, $P = (F_o^2 - 2F_c^2)/3$.

4.3.4 Proposed mechanism of assembly-induced luminescence

The molecular orbitals of the monomer state and the trimer of the **Pt-CN** are shown in Figure X . It can be seen that the LUMOs of both the monomer and the trimer are similar. On the other hand, the HOMO of the monomer is localized to the center metal ion and the ligand, whereas the HOMO of the trimer is quite different. The HOMO of the trimer was localized to the dz^2 orbital of the center metal and the sigma bond of the metal carbene. These results suggest that there is an interaction between the molecular orbitals spread from the dz^2 orbital of the platinum to the carbene ligand. As in the **Pt-CN** the LUMO is located mainly in the π^* of the ligand, while the HOMO is distributed in the dz^2 orbital of the center metal and in the carbene metal bond.

The close distance between the central metal ion and the carbene carbon in the crystal and the DFT results suggested that the absorption and luminescence properties are greatly affected by the interaction of orbitals spread from the dz^2 orbital to the carbene ligand. In other words, A new type of assembly-induced emission originated from NHC σ orbital mixed metal-metal to ligand charge transfer. Thus, assembly-induced luminescence involving d orbitals cannot be discussed only by simple van der Waal radius. In fact, Ma et al. reported in 2022 that Pt-Pt interactions could exist even at intermetallic distances of 3.7 Å for **[Pt(C^N)(N^N)]BPh$_4$** (C^N = 2-(2,4-difluorophenyl)pyridine (bfppy); N^N = 2,2-bipyridine (bpy))**,** as revealed by crystal structure and spectroscopic analysis. [19] Thus, assembly-induced luminescence involving d orbitals is strongly influenced by using ligands since the orbital spreading should be considered.

On the other hand, **Pd-CN** does not exist directly interaction, considering the van der Waal radius of Pd and Pd⋯Pd distance, and it is difficult to assign a luminescence origin of Pd-CN in the solid state at room temperature. However, the luminescence origin switches from ^{3}LC with vibrational structure emission band to broad emission due to the change in the stacking structure with increased temperature, and a new absorption band, which is not observed in solution, is observed in the excitation spectrum at RT. These results suggest that the luminescence origin is from the assembly reflecting the structure of the ground state. In addition, the relatively large value of the radiative rate constant ($k_r \sim 10^4$) suggests the contribution of the orbital of the central metal ion.
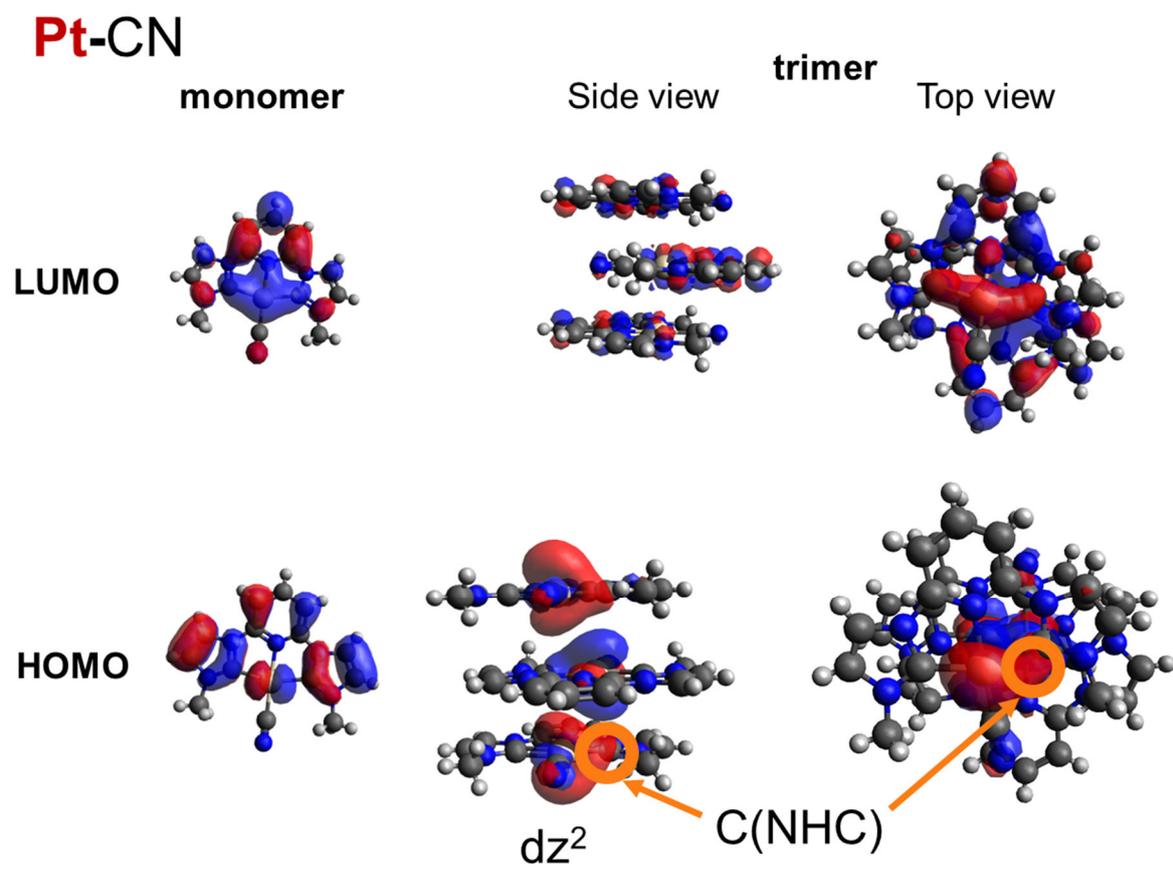
Figure 12. Kohn–Sham orbitals in the frontier region of the singlet ground state, obtained by single-point calculations using the geometry of crystal structure.

4.4 Conclusion

In summary, cationic platinum(II) and palladium(II) complexes with tridentate NHC ligand and cyanide ligand were developed and studied. The effect of the C^N^C tridentate ligand, including two NHCs, on photophysical properties, was investigated. Both Pt(II) and Pd(II) complexes self-assembled infinite 1D chains by intermolecular interaction. Interestingly, **Pd-CN** shows thermochromic behavior corresponding to a slight change in stacking structure. This study shows that a new type of assembly-induced luminescence from NHC orbitals involves MMLCT excited states and provides a new approach to developing assembly-induced luminescence in d^8 metal complexes.
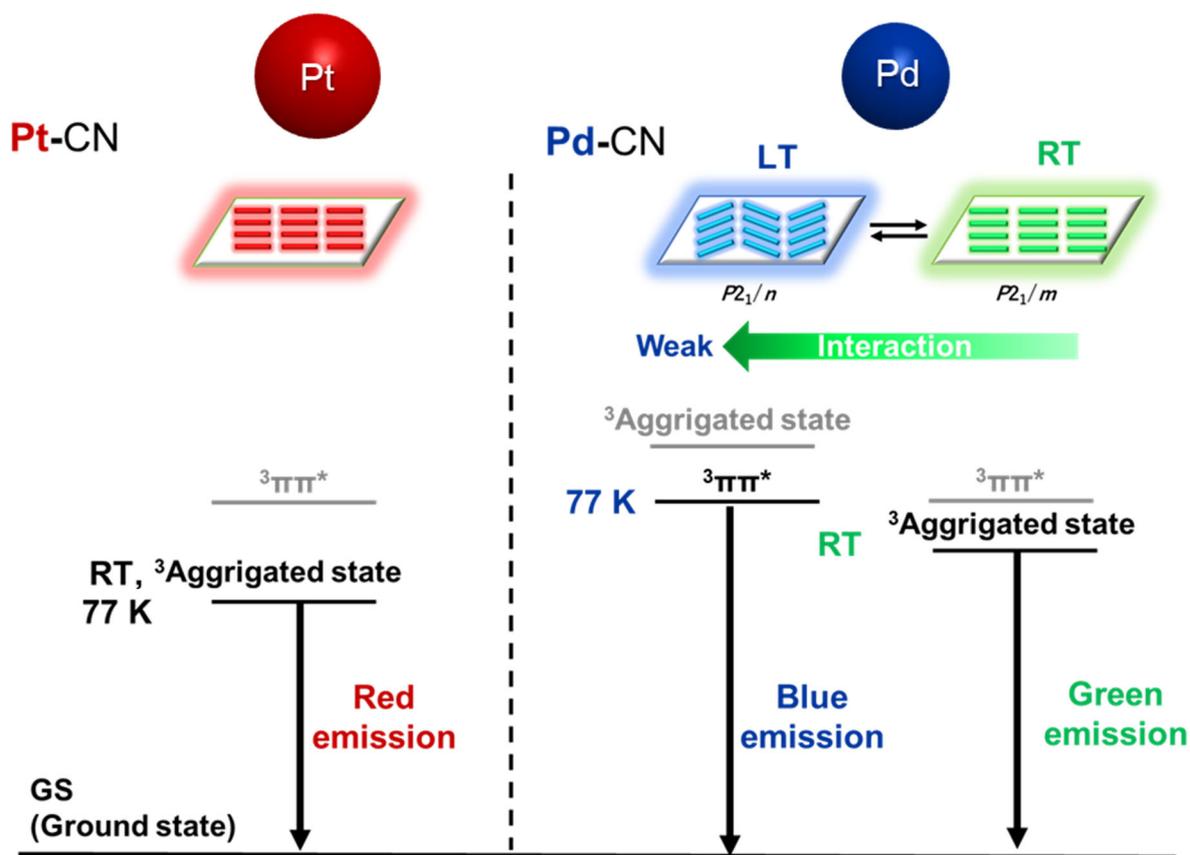
References

[1] O. S. Wenger, *Chem. Rev.* **2013**, *113*, 3686–3733.

[2] M. Kato, *Bull. Chem. Soc. Jpn.* **2007**, *80*, 287–294.

[3] V. W.-W. Yam, V. K.-M. Au, S. Y.-L. Leung, *Chem. Rev.* **2015**, *115*, 7589–7728.

[4] Q. Wan, W. To, C. Yang, C. Che, *Angew. Chem. Int. Ed.* **2018**, *57*, 3089–3093.

[5] C. Zou, J. Lin, S. Suo, M. Xie, X. Chang, W. Lu, *Chem. Commun.* **2018**, *54*, 5319–5322.

[6] J. Lin, C. Zou, X. Zhang, Q. Gao, S. Suo, Q. Zhuo, X. Chang, M. Xie, W. Lu, *Dalton. Teans.* **2019**, *48*, 10417–10421.

[7] D. J. Mabbott, B. E. Mann, P. M. Maitlis, *J. Chem. Soc. Dalton Trans.* **1977**, *0*, 294–299.

[8] E. Peris, J. A. Loch, J. Mata, R. H. Crabtree, *Chem. Commun.* **2001**, *0*, 201–202.

[9] W. H. Melhuish, *J. Phys. Chem.* **1961**, *65*, 229–235.

[10] W. R. Dawson, M. W. Windsor, *J. Phys. Chem.* **1968**, *72*, 3251–3260.

[11] *CrysAlisPro, Version 1.171.40.67a*, Rigaku Corporation, Oxford, UK, **2018**.

[12] G. M. Sheldrick, *Acta. Crystallogr. Sect. A.* **2015**, *71*, 3–8.

[13] G. M. Sheldrick, *Acta. Crystallogr. Sect. C.* **2015**, *71*, 3–8.

[14] O. V. Dolomanov, L. J. Bourhis, R. J. Gildea, J. A. K. Howard, H. Puschmann, *J. Appl. Crystallogr.* **2009**, *42*, 339–341.

[15] M. J. Frisch, G. W. Trucks, H. B. Schlegel, G. E. Scuseria, M. A. Robb, J. R. Cheeseman, G. Scalmani, V. Barone, G. A. Petersson, H. Nakatsuji, X. Li, M. Caricato, A. V. Marenich, J. Bloino, B. G. Janesko, R. Gomperts, B. Mennucci, H. P. Hratchian, J. V. Ortiz, A. F. Izmaylov, J. L. Sonnenberg, D. Williams-Young, F. Ding, F. Lipparini, F. Egidi, J. Goings, B. Peng, A. Petrone, T. Henderson, D. Ranasinghe, V. G. Zakrzewski, J. Gao, N. Rega, G. Zheng, W. Liang, M. Hada, M. Ehara, K. Toyota, R. Fukuda, J. Hasegawa, M. Ishida, T. Nakajima, Y. Honda, O. Kitao, H. Nakai, T. Vreven, K. Throssell, J. A. Montgomery, Jr., J. E. Peralta, F. Ogliaro, M. J. Bearpark, J. J. Heyd, E. N. Brothers, K. N. Kudin, V. N. Staroverov, T. A. Keith, R. Kobayashi, J. Normand, K. Raghavachari, A. P. Rendell, J. C. Burant, S. S. Iyengar, J. Tomasi, M. Cossi, J. M. Millam, M. Klene, C. Adamo, R. Cammi, J. W. Ochterski, R. L. Martin, K. Morokuma, O. Farkas, J. B. Foresman, and D. J. Fox, *Gaussian 16, Revision C.01*, Gaussian, Inc., Wallingford CT, **2016**.

[16] Y. Zhao, D. G. Truhlar, *Theor. Chem. Acc.* **2008**, *120*, 215–241.

[17] D. Andrae, U. Häußermann, M. Dolg, H. Stoll, H. Preuß, *Theoret. Chim. Acta.* **1990**, *77*, 123–141.

[18] R. Krishnan, J. S. Binkley, R. Seeger, J. A. Pople, *J. Chem. Phys.* **1980**, *72*, 650–654.

[19] M. Chaaban, S. Lee, J. S. R. V. Winfred, X. Lin, B. Ma, *Small Struct.* **2022**, 3, 2200043.

Chapter 5

General Conclusion

This thesis focused on controlling emission properties in the solid states by intermolecular interactions on self-assembled Pt(II) and Pd(II) complexes.

In chapter 1, the research background and purpose of this thesis were described. The phosphorescence metal complexes, assembly-induced emission of Pt(II) complexes and other d^8 metal complexes, external stimulus-responsive materials in the crystal states and the outline of this thesis were summarized.

In chapter 2, the synthesis, crystal structure, and photophysical properties of novel neutral Pt (II) complexes, [Pt(CN)$_2$(R-impy)] (R-impy = 1-alkyl-3-(2-pyridyl)-1H-imidazol-2-ylidene, R = Me (**1**), Et (**2**), ^{i}Pr (**3**), and ^{t}Bu (**4**)) were described. For novel neutral platinum(II) complexes with an N-heterocyclic carbene (NHC), the Pt$\cdots$Pt distance in the crystal is precisely controlled by systematically changing the bulkiness of the substituent. This precise control and the selection of a ligand with an appropriate π-system resulted in the first achievement of blue ^{3}MMLCT luminescence in addition to yellow-green luminescence, which is rare for ^{3}MMLCT luminescence, and the luminescence properties were investigated in detail from the crystal structure and temperature dependence of the luminescence properties. This result, which shows that strong luminescence and a wide range of luminescence color control are possible while maintaining the same molecular skeleton, is a result that reconfirms the superiority of ^{3}MMLCT luminescence.

In chapter 3, complex **4** with weak Pt interactions investigated its vapor responsivity in expecting a flexible response to external stimuli based on the weak interactions. in self-assembled systems exhibiting vapochromic luminescence, such a reversible Single-Crystal to Single-Crystal (SCSC) structural transformation by vapor adsorption and desorption has not been reported before and is assumed to be a property exhibited by flexible, organized systems with weak Pt$\cdots$Pt interactions.

In chapter 4, cationic platinum(II) and palladium(II) complexes with tridentate NHC ligand and cyanide ligand, [M(bisimpy)CN]PF$_6$ (M = Pt (**5**), Pd (**6**); 2,6-bis(3-methyl-1H-imidazol--2-ylidene)pyridine) were developed and studied. The effect of the C^N^C tridentate ligand, including two NHCs, on photophysical properties was investigated. Both Pt(II) and Pd(II) complexes self-assembled infinite 1D chains by intermolecular interaction. Interestingly, complex **6** shows thermochromic behavior corresponding to a slight change in stacking structure. This study shows that a new type of assembly-induced luminescence from NHC orbitals involves MMLCT excited states and provides a new approach to developing assembly-induced luminescence in d^8 metal complexes.

These results provide some strategies for the design of assembly-induced luminescent d^8 metal complexes. Appropriate control of such weak intermolecular interactions is expected to develop further a group of "soft crystal" materials as highly ordered and flexible responsive systems with various functions. In addition, in the case of palladium(II) and nickel(II) complexes, which have the same d^8 electron configuration as platinum(II) complexes, the weak ligand field is disadvantageous for luminescence. However, it is expected that the weak intermolecular interactions in the 4d and 3d orbitals will be utilized to develop more flexible response systems and luminescent properties through self-assembly.

Acknowledgment

<div align="right">

Daisuke Saito

Graduate School of Chemical Sciences and Engineering

Hokkaido University

</div>